MCP optics

Adam North Brunton

Thesis submitted to the University of Leicester for the degree of Doctor of Philosophy.

December 1994

X-Ray Astronomy Group

Department of Physics and Astronomy

University of Leicester

University Road

Leicester

U.K.

UMI Number: U070121

UMI

Dissertation Publishing

ProQuest

Abstract

This thesis is an account of research into a novel type of X-ray optic - the microchannel plate (MCP).

Experiments to determine the point to point focusing properties of square pore MCPs manufactured by Galileo Electro-Optics and Philips Photonics are reported. These were performed both in a test chamber at Leicester with an electron-bombardment X-ray source and with a laser-plasma X-ray source at the Rutherford Appleton Laboratory. A resolution of 6 arcmin and an intensity gain of 20 were recorded using a Galileo focusing MCP.

An invesigation into the focusing action of MCPs which have been curved to a spherical figure is detailed. Such curved MCPs may, in a manner reminiscent of a conventional refractive lens, be used to focus a parallel X-ray beam to a point forming the basis of an X-ray telescope, or conversely to convert the diverging beam from a point-like X-ray source to a quasi-parallel one. The curving experiments were performed by Philips Photonics on standard circular pore MCPs. Tests on these plates were performed at Leicester; the results appear favourable. The technique has been applied to MCPs of up to 4mm thickness, curving them to a radius of 1.4m (0.7m focal length).

A comprehensive Monte Carlo ray-tracing model is presented. This was initially developed to facilitate an understanding of the geometry of MCP focusing and to produce idealised images corresponding to a given experimental set up. These perfect images may be compared with, or used to predict experimental results. Comparison with experimental results led to incorporation of MCP distortions into the code. These distortions have been found by a programme of metrology which is also described. The model has led to a clear insight into the causes of poor image quality and their relative importance.

Declaration

I hereby declare that no part of this thesis has been previously submitted to this or any other University as part of the requirements for a higher degree. Work described here was conducted by the undersigned except for the contribution of colleagues indicated in the text.

Adam Brunton

December 1994

Acknowledgements

List of Publications

Some of the experimental results reported in this thesis have been incorporated in the following papers. The chapters to which these papers refer are given in brackets.

1. 'X-ray focusing using square-pore microchannel plates: first observations of cruxiform structure.'

   G. W. Fraser, A. N. Brunton, J. E. Lees, J. F. Pearson and W. B. Feller

   Nuclear Instruments and Methods in Physics Research A 321 (1993) 404   (Chapter 3).

2. 'Production of quasi-parallel X-ray beams using microchannel plate "X-ray lenses"' G. W. Fraser, A. N. Brunton, J. E. Lees and D. L. Emberson

   Nuclear Instruments and Methods in Physics Research A 334 (1993) 579 (Chapter 4).

3. 'Development of microchannel plate (MCP) optics'

   G. W. Fraser, A. N. Brunton, J. E. Lees, J. F. Pearson, R. Willingale, D. L. Emberson, W. B. Feller, M. Stedman and J. Haycocks

   Proc.SPIE 2011 (1993) 215 (Chapters 3,4 and 6).

4. 'Hard X-ray imaging using microchannel plate optics'

   J. E. Lees, G. W. Fraser, A. N. Brunton and R. Willingale

   Presented to International Workshop on High Energy Astronomy, Anacapri 26th Sept 1994 (Chapters 3,4 and 6).

5. 'High intensity focused X-rays from a repetitive laser plasma source'

   I. C. E. Turcu, A. N. Brunton, J. E. Lees, G. W. Fraser and P. Land

   In preparation (Chapter5).

Contents

Chapter 1

Microchannel plate X-ray optics for astronomy

1.1 Intro   duction

Microchannel plates (MCPs) are one example of a novel class of X-ray optic - the capillary array. In these optics, rays are redirected by reflection from the inside surfaces of tubes which may be of square or circular cross-section. In principle these tubes could be made from any material, but in practice are usually manufactured by the drawing and etching of glass, in the manner of fibre optics. Currently the two most important examples of capillary optics are (i) the microchannel plate, with which the reader will become thouroghly acquainted by the end of this thesis and (ii) the so called "Kumakhov Lens" (Kumakhov & Komarov 1990; Gibson & MacDonald 1994). Gorenstein (1991) reviewed the Kumakhov Lens in an astronomical context and his findings were rather favourable. Since that time, a probable high cost and lack of any true imaging capability seem, however, to have caused the Kumakhov Lens to fall from favour with the astronomical community. Kumakhov optics, therefore, will not be discussed in detail here.

The capillaries or channels of an MCP have diameters of the order $10 - 100\mu$m. This means that compared to conventional grazing incidence X-ray optics their reflective surfaces are packed

very closely together. Hence, for a given aperture, the effective area of a microchannel plate is very large compared with that of a conventional optic. Large effective area is, of course, one of the primary goals of any astronomical telescope design. Furthermore, the "large area" of MCP optics is located close to the optical axis. This means that the grazing angles involved in reflection from the channel surfaces are necessarily small. MCPs should therefore be able to operate at shorter wavelengths than conventional X-ray mirrors of a similar focal length. This property leads to one of the proposed applications of MCP optics in astronomy; a hard X-ray telescope working at photon energies of up to 60keV (Fraser *et al.* 1993c; Holland *et al.* 1994; Willingale & Fraser 1995).

Another interesting feature of MCP optics is that their focal surface is a sphere with half the radius of the optic. As long as a detector whose front surface approximates to a section of a sphere can be manufactured, MCPs may be tesselated to form a telescope with an, in principle, unlimited field of view. The almost negligible mass of MCPs is a further advantage for such a large aperture telescope. An X-ray sky survey mission or an all sky monitor (ASM) are further applications to which MCP optics appear very well suited (Fraser *et al.* 1990; Fraser *et al.* 1991b; Kaaret & Geissbühler 1991).

This thesis should be viewed as a proof of concept investigation, at the most basic level, of the technologies required to fabricate MCP optics for one or the other of these missions. It also reports the development of techniques required to characterise channel plate optics and research into the factors which limit their performance. This particular chapter contains a brief description of MCPs, the history and mechanism of their use as optics and how they may be of use to X-ray astronomers.

1.2   Microchannel Plates (MCPs)

Microchannel plates were developed in the late 1960s as compact imaging electron multipliers for "night vision" image intensifiers. Since then they have seen widespread scientific use as detectors for visible light, UV and X-rays and as charged particle detectors (Wiza 1979; Fraser 1989). Although their use as multipliers is not the subject of this thesis, it warrants some attention both from a historical point of view and because most of the focused images presented in later

8

chapters were recorded using an MCP detector (see section 3.1.5). MCPs were initially developed from continuous dynode channel electron multipliers (CEMs) which are glass or ceramic tubes with a metal oxide semiconducting layer deposited on their inside surface (Lecomte & Perez-Mendez 1978). A photon or charged particle with sufficiently high energy can, after entering the channel, cause the emission of electrons when it strikes the channel wall. A high voltage is maintained between the ends of the channel which accelerates the ejected electrons. As the semiconducting surface is treated to render the secondary electron yield greater than unity, an avalanche develops, so that a single photon causes a sizeable charge to be developed at the channel exit. The gain for a CEM is $\sim 10^8$ and around 10^4 for a single MCP which is essentially a large number ($\sim 10^7$) of very small examples ($\sim 10\mu m$ channel diameter) of such multipliers packed together to form a plate. The manufacturing method by which the array of tiny capillaries which constitute an MCP is constructed is described in section 1.3 below. Some of the features of MCPs are desirable both for the established multiplier industry and for the nascent focusing activity. These are uniformity of the channel shape and matrix and parallelism of the channels.

If a focusing MCP is deficient in these attributes its performance will be degraded; the focal spot will be broad and the angular resolution poor. The distortions mentioned above, if present in a multiplier plate, will lead to non-uniform response. Therefore, the MCP industry had already taken steps towards achieving the main requirements of capillary array optics before the optics themselves had been conceived.

Conventionally, MCPs are fabricated with channels of circular cross-section. Unfortunately most optical applications require square channels. Theoretically, a square section channel may give better X-ray detection efficiency (Fraser *et al.* 1991a) and some polarisation sensitivity (Fraser, Lees & Pearson 1989). In order that these potential enhancements might be investigated, within the Leicester programme, some experimental square pore plates were manufactured by Philips Photonics [1] and by Galileo Electro-Optics [2]. It is partly the focusing properties of these prototype plates which are described in this thesis.

---

[1] Philips Photonics, Mitcham, Surrey, UK now transferred to: Avenue Roger Roncier, B.P. 520, F-19106 Brive la Gaillarde Cedex, France

[2] Galileo Electro-Optics Corp. Galileo Park, Sturbridge, MA 01466, USA.

Typically MCPs are circular with diameters of $\sim 25 - 50$mm. Larger area MCPs (100×100mm square) are to be used in the High Resolution Camera (HRC) of NASA's Advanced X-ray Astrophysics Facility (AXAF) (Winkler *et al.* 1993). The HRC is a collaborative development of the Harvard-Smithsonian Centre for Astrophysics, the Universities of Leicester and Hawaii and of the Osservatrio G. S. Vaiana, Palermo. Indeed a detector incorporating examples of these AXAF HRC plates was used to record the majority of the images presented in this thesis (see section 3.1.5). In standard MCPs the channels have an aspect or length to diameter ratio $L{:}D{\sim}40{:}1$. In X-ray detectors they tend to be rather longer; the AXAF plates have $L{:}D{=}120{:}1$. Generally the channel axes are not at right angles to the front and rear surfaces of the plate but are inclined at a "bias angle" of around $13°$ in order to eliminate ion feedback in two-stage "chevron" or three-stage "Z-stack" high gain configurations. A non-zero bias angle is a nuisance to the focusing enthusiast but does not prevent point to point focusing with a flat plate. It does, however, preclude curving or "slumping" the plates to the spherical figure required for astronomical applications.

There are many overviews of MCP technology available in the literature, for example the afore-mentioned Wiza (1979) and Fraser (1989). For reasons which will become clear later in this chapter, standard MCPs are not ideal for X-ray focusing. Some recent technological advances in techniques for slumping MCPs to a spherical figure are reported in chapter 4.

1.3   MCP manufacture

The way in which MCPs are manufactured is important in the context of X-ray focusing since a knowledge of the process stages (figure 1.1) may give an insight into many of the distortions exhibited by these optics, which in turn limit the resolution and the flux concentration which can be achieved by their use.

A hollow tube of lead silicate "cladding glass" has a bar of etchable "core glass" inserted in its centre to support it physically during the fabrication process. The composite bar is heated and pulled, to form a fibre of approximately 1mm diameter. It is then chopped up into short lengths. For a square pore MCP, these lengths are assembled (manually in most cases) to form the square section "second draw stack" of (say) 40x40 units. If a circular channel MCP is being
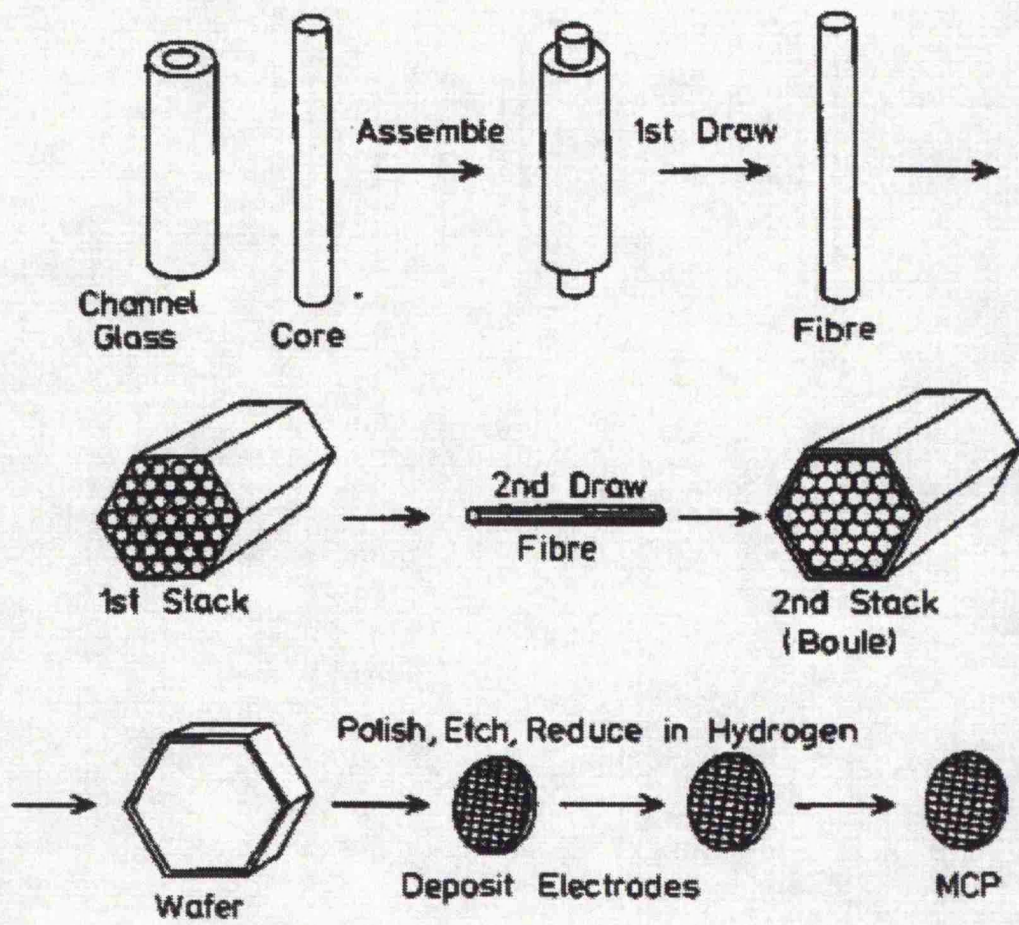
Figure 1.1: MCP manufacturing process

11

manufactured the stack will be hexagonal due to the packing geometry of the circular fibres. The first draw stack is pulled to form a "multifibre". Lengths are then cut from the multifibre and stacked in a "boule", 20-30 cm long. The boule is heated and fused under vacuum. Proto-MCPs are sliced from this boule. They are ground to the correct shape then polished. Finally, they are etched using a strong alkali, to remove the core glass and form MCP blanks. Figure 1.1 is a schematic of this manufacturing process.

For multiplier operation the blank needs to be heated in a hydrogen atmosphere which causes a semiconducting layer with the required secondary electron yield and resistance to be formed at the surface of the channels. Multiplier MCPs must also have metal electrodes deposited on the front and rear surfaces to allow application of the high voltage along the channel length. Neither electroding nor hydrogen firing is necessary for MCP operation as an X-ray optic, though it is thought that the hydrogen reduction process may decrease the surface roughness of the channels (see chapter 3). If the MCP is to become an optical element, it may well need to be "slumped" to a spherical section. This is done at Philips by a proprietary technique which involves bending the MCP blank to the correct shape and then heating to anneal it. Slumping is ideally performed prior to etching while the core glass still supports the channels; the technique may, however, be applied after etching.

From consideration of this manufacturing technique we can see that misalignments between the channels may be introduced at either the first or second stack stages. Any twisting during the draw stages will distort the channels or multifibres. Distorted channels may also arise during the fusion stage when both the channels and the matrix may be crushed near the edges and, particularly, near the corners of the multifibres. All of these problems have been seen in real square pore MCPs; their effects are described in later chapters (3,5 and 6).

1.4 MCPs as Optics

1.4.1 A brief history

The very first idea for focusing X-rays used reflection from orthogonal surfaces (Kirkpatrick & Baez 1948). In the Kirkpatrick-Baez configuration the reflecting surfaces are actually spherical,
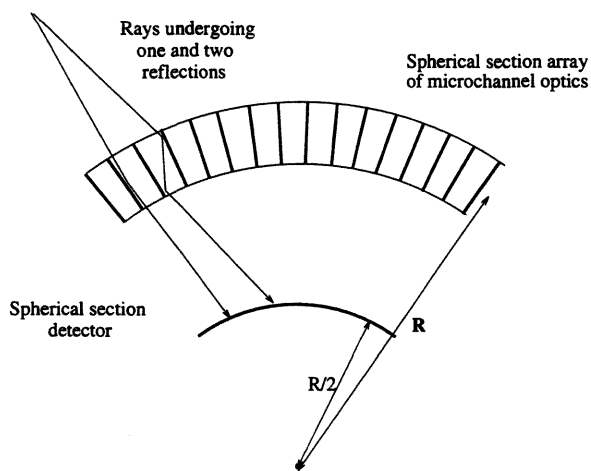
Figure 1.2: An All Sky Monitor telescope which, in principle, has an unlimited field of view, based *exactly* on the geometry of a lobster's eye

though the radii of curvature are large and may be approximated by planes (Joy & Weisskopf 1991). A square pore MCP optic could be considered as such an approximation to this well known geometry. Historically, the next step towards capillary optics was a proposal to make a one dimensionally focusing wide angle telescope using a set of reflecting planes normal to the surface of a cylinder. (Schmidt 1975; Schmidt 1981). This geometry focuses incoming X-rays onto a second cylinder with half the radius of curvature of the optic (figure 1.2) in the same way that an MCP optic will focus onto a sphere (section 1.1). This system still has some proponents, for example Hudec *et al.* (1994).

Square arrays of reflective surfaces were first proposed as a two dimensional focusing / imaging device by Angel (1979). Angel did not think of the idea himself, he plagiarised it, rather appropriately, from *God* who as Land (1978) reported in a fascinating paper, had installed similar devices in the eyes of Lobsters.

In 1979 150μm square channel glass capillary arrays manufactured by Galileo using the MCP technique of section 1.3, were being studied at Leicester for use as collimators in front of EX-OSATs Medium Energy Detector Array (MEDA) proportional counters (Turner & Smith 1981;

Fraser *et al.* 1989). Realising that these collimator blocks were ideal for the realisation of Angel's idea, Martin Turner, from the Leicester X-ray astronomy group contacted him offering to try out the collimators as focusing devices. Unfortunately, no collaboration was forthcoming and the "lobster eye" optic never left the drawing board. Ironically the main difficulty with the EXOSAT collimators was the need to *reduce* the reflectivity of the channel walls as reflected rays led to flat tops on the desired saw-tooth transmission *vs* angle function.

After Angel's brief flirtation with lobster eye optics, interest in the area lapsed. It was rekindled in Australia (Wilkins *et al.* 1989; Chapman, Nugent & Wilkins 1991). The University of Melbourne / CSIRO collaboration realised that MCP technology could provide uniform arrays of small square channels like the ones found in lobster eyes. These authors also made an attempt at slumping a circular pore MCP from Varian so that it would resemble a lobster eye more closely (Chapman *et al.* 1990).

Next, Dr. S. Wilkins from CSIRO approached Galileo Electro-Optics, wondering if they could provide him with some square pore MCPs for his experiments. Galileo had already, in fact, supplied square channel MCPs to Leicester and Columbia Universities who were, at that time, collaborating in a quest for an imaging X-ray polarimeter based on these devices (Kaaret *et al.* 1989). Bruce Feller of Galileo mentioned this novel MCP application to George Fraser of Leicester and Prof. Bob Novick at Columbia. They immediately saw the potential of these optics for a wide angle "All Sky Monitor" (ASM) telescope. At that time there was an ESA small satellite mission opportunity so the MCP lobster eye was (unsuccessfully) proposed (Fraser *et al.* 1990; Fraser *et al.* 1991b; Kaaret & Geissbühler 1991). Laboratory programmes in MCP optics at both Leicester and Columbia began in early 1991. The Columbia group, after some efforts (Kaaret & Geissbühler 1991; Kaaret *et al.* 1992) with MCPs, turned their backs on that technology in favour of a micromachining approach to capillary optics (Chen, Kaaret & Kenny 1993) in which they attempt to etch channels in silicon wafers by using potassium hydroxide which preferentially eats along the 110 crystal plane at a rate 400 times that at which it etches in the perpendicular 111 direction. The idea behind this is that the channels so produced will automatically be aligned with the crystal planes of the silicon, giving near perfect uniformity.

The bulk of the Leicester efforts to date, based entirely on glass capillary microchannel plates and conducted on a limited budget are detailed in the following pages.

14
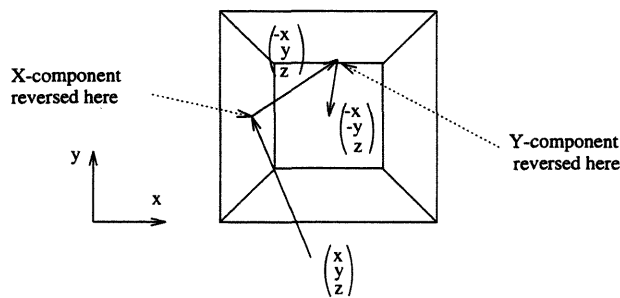
Figure 1.3: A view along the z-direction of a ray being doubly reflected by a square section MCP channel. Rays that end up in the central "true" focus are reflected an odd number of times by each of the orthogonal channel walls. If we think of the walls as being parallel to the yz and xz planes as shown in the diagram, then reflection by them negates the x and y direction cosines respectively, while leaving the other components unchanged. So the ray is focused to a point on the far side of the plate from the source which has the same x and y coordinates as the source point.

1.4.2   Focusing Mechanism

The MCP optic works by grazing incidence specular reflection from the channel surfaces. A straightforward comparison of X-ray wavelengths ($< 100\text{Å}$) with the channel dimensions ($> 10\mu\text{m}$) shows that diffraction plays no part in their operation.

A planar array of square pores will relay an image of an extended source to an equidistant position on the opposite side of the optic. A square channel with its planar walls will reflect light from a given point to another almost unique point with only a small uncertainty due to the physical size of the channel. The mechanism is easy to visualise since the geometry of the channels follows Cartesian coordinates (figure 1.3) When a ray of light is reflected by the "xz wall" the x component of its direction vector is negated, while the y component remains unchanged. Similarly when a ray is reflected from the yz wall its y component is reversed leaving the x component as it was. If a ray is reflected twice, once in each plane it ends up going in the opposite direction to that in which it entered the plate. Thus it will meet a detector plane equidistant with the source from the MCP at the same x and y co-ordinates that it left the source and will form part of an image of the source (figure 1.3). The uncertainty in the image

15
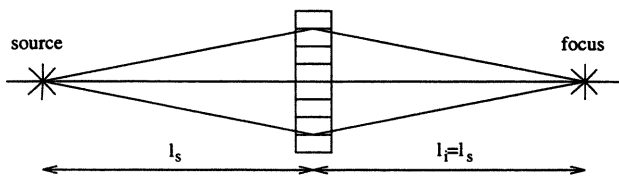
Figure 1.4: A Flat capillary array can be used to focus a point source to another point
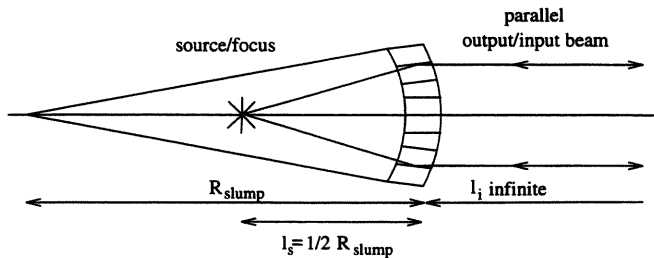
Figure 1.5: A spherically slumped optic will focus a parallel beam to a point or expand a point source to a quasi-parallel beam.

position is due to the finite size of the channel which allows a range of incidence angles on the channel wall and gives a small spread in the output ray directions.

Unfortunately only about a third of the rays undergo this double reflection. Another third are only singly reflected and the final third pass straight through the plate. The singly reflected rays form the cross structure characteristic of these devices (see chapter 3). The rays passing straight through the plate form a diffuse halo around the image.

We have seen that a flat plate will serve to refocus a point light source at another point some distance away (figure 1.4), thus acting as a relay lens. If the plate is slumped to a spherical figure, so that the channels point to a common centre, then a parallel beam can be focused to a point such that the image distance is half the radius of curvature. This is Angel's lobster eye geometry. When the angular extent of the optic is extended (by tesselating the MCPs) then

parallel beams from different directions are focused to points on a sphere with half the radius
of curvature of the sphere on which the optics lie (figure 1.2).

Alternatively a slumped plate may be used to convert the diverging beam from a point X-
ray source to a quasi-parallel one (figure 1.5). This geometry has been extensively used in
the laboratory testing of slumped plates (see chapter 4). This "beam expander" has no use
in astronomy. It may, however, prove to have terrestrial applications, for instance providing
parallel beams for X-ray lithography to produce microelectronic devices. Some early work in
this area will be reported in a forthcoming paper. In short, the slumped MCP displays most
of the properties of a conventional refractive lens. Indeed the focus is described by the lens
equation: (Wilkins *et al.* 1989):

$$\frac{1}{l_s} - \frac{1}{l_i} = \frac{2}{R_{slump}} \qquad (1.1)$$

where l_s and l_i are the source and image distances and R_{slump} the radius of curvature, is positive
when the source is on the concave side of the plate.

Detailed explanations of flat and slumped square pore plate focusing mechanisms are given in
sections 2.4.3 and 2.5.3 respectively. The Melbourne / CSIRO group have published analytical
treatments (Wilkins *et al.* 1989; Chapman, Nugent & Wilkins 1991) of both square and circular
pore MCP focusing.

1.5   MCP optics for imaging in X-ray astronomy

Two X-ray astronomical applications of MCP optics have been considered at Leicester; the All
Sky Monitor (ASM) (Fraser *et al.* 1990; Fraser *et al.* 1991b; Kaaret & Geissbühler 1991) and
the Hard X-ray Telescope (HXT) (Fraser *et al.* 1993c; Holland *et al.* 1994; Willingale & Fraser
1995). These designs will not be detailed here but a short discussion of the more demanding
requirements for the optics of HXT is appropriate. The HXT is a multifocus hard X-ray imager
with a focal length of 5m. It is intended to operate at photon energies of up to 60keV. The
microchannel optics proposed for it are of a novel design. They incorporate pairs of MCPs
with radially packed channels, one in front of the other. The secondary has a focal length one

third that of the primary. This is an approximation to the Wolter type 1 geometry (Wolter 1952a; Wolter 1952b) which has been the mainstay of soft X-ray astronomy to date, and halves the grazing angles encountered by the reflected rays. The HXT could be built with square packed MCPs approximating the Kirkpatrick-Baez geometry, albeit with some compromise in the effective area per optic unit. Characteristics of the telescope have been calculated by ray-tracing (Fraser *et al.* 1993c; Willingale & Fraser 1995).

The two alternative image forming technologies in this energy band are reviewed by Ramsey, Austin & Decher (1994). The first is the well-established coded aperture mask (Caroli *et al.* 1987) which suffers from a poor signal to noise ratio and the need for a large detector when compared with focusing techniques. The second technology is the relatively novel "graded d-space" multilayer or "supermirror" (Christensen *et al.* 1994). This, as the name implies, is a multilayer mirror with varying layer spacings to enable it to reflect X-rays of different wavelengths. The closer spaced layers are at the bottom of the stack, these reflect the short wavelength X-rays which penetrate through the widely spaced upper layers. Telescopes have been proposed in which these coatings are deposited on Kirkpatrick-Baez or Wolter optics in order to extend their operating range to around 100keV.

The modelled performance of HXT was found to be favourable compared with telescopes of both these types. The constructional tolerances incorporated in the HXT ray trace code were an RMS surface roughness of 10Å and an RMS channel misalignment angle of 100arcsec (Willingale & Fraser 1995). These figures could be taken as a first goal for a workable MCP optic system, although there is no reason why they could not be surpassed.

Chapman, Nugent & Wilkins (1991) inform us that for optimum focusing effect at high photon energies (> 8keV) the channels should have an aspect ratio $L{:}D = 1/tan\theta_{crit}$ where L is the channel length, D is the square side length and θ_{crit} is the critical angle (which decreases with increasing photon energy) above which total external reflection is not possible. In this hard X-ray range the critical angles are of the order of arcminutes so the channels have to be of high aspect ratio, around 700:1 would be desirable. This causes twofold difficulties, first these long channels have to be etched and secondly the resulting thick plates ($700 \times 12.5\mu m \simeq 9$mm) have to be slumped.

The requirements for the ASM are, if anything, less stringent. The primary difficulties with this system are the engineering ones: assembling a mosaic of optics to cover hundreds of square degrees and devising a suitable detector.

The HXT specification leads to a set of requirements for MCP optics. These can be listed as follows.

- Drawing and assembly of regular cuboidal channels

- Etching of long channels

- Production of smooth channel surfaces

- Achievement of good parallelism between channels on flat plates

- Slumping of thick plates to an accurate spherical figure, maintaining good channel alignment.

The chapters that follow describe assess the current technology in flat square pore MCPs and detail some steps in the development of a new technology - slumping plates to a spherical figure. All of the requirements on the list above are addressed. A comprehensive ray-trace model is developed in order to determine the relative and absolute importance of the various distortions and misalignments seen in these optics.

Chapter 2

Basic ray-trace models

2.1 Intro duction

Ray tracing is a tool used in all types of optical design work, from X-ray mirrors to camera lenses. It is logical, therefore, to apply this technique to modelling the response of MCP or capillary optics. Considerable effort has been devoted to developing ray-tracing programmes, both to look at the optical properties of "perfect" MCPs and to investigate the effect on image quality of distortions, which are known to exist in "real-life" channel plates.

These Monte Carlo codes were developed in parallel with the experimental campaign, rather than before or afterwards. For the purposes of this thesis it seems logical to divide their description into two parts. The perfect plate codes are described in this chapter and the codes which incorporate distortion of the MCP are explained later on, in chapter 5, as these require experimental input regarding the nature of MCP imperfections.

The purpose of the perfect plate codes is both to verify results obtained in the lab, and predict distributions of rays for a given experimental configuration, without having to actually perform the experiment. These codes deal with idealised arrays of channels; that is, perfect cylinders or cuboids, with perfectly smooth surfaces, aligned parallel to one another, in the case of flat point-to-point focusing optics, or perpendicular to a sphere defining the surface of the MCP, in the case of a spherically slumped plate. There are two generic divisions: square or circular pores

20

and flat or slumped plates.

The simulations were all written in the fortran language, initially the computer used to run them was a DEC[1] Vaxstation 3100. To run a typical simulation, tracing a million rays, would take a few hours on this machine, usually necessitating an overnight run. When the Leicester University Computer Centre acquired an SGI[2] Challenge XL mainframe system all the ray-tracing codes were ported onto this platform, which allows a million rays to be traced in about three minutes. Some of these programmes have been experimentally compiled on a Sun[3] Sparcstation 10: on this machine, which has a floating point performance rating of around 80 specmarks, they run at about half the speed that they do on the SGI computer. One million rays has been adopted as a standard simulation length as it is comparable to the number of events generally accumulated when MCP optics are illuminated with X-rays in the lab at Leicester.

2.2 X-ray reflectivities

All the simulation codes use a routine which calculates, for each individual reflection, the reflectivity of the MCP lead silicate glass, whatever its composition may be, at the incident angle of the X-ray on the channel surface. The reflectivity is calculated the derivation due to Henke (1981) of Fresnel's equations.

The complex dielectric constant required by these equations is obtained from the atomic scattering cross-section database of Cromer & Liberman (1970). This database contains calculated photo-electric cross-sections, at various energies, for many elements. A programme reads these cross-sections and calculates the atomic scattering factors f_1 and f_2 from them:

$$f_1(E) = Z + \frac{1}{\pi r_0 h c} \int_0^\infty \frac{\epsilon^2 \mu(\epsilon)}{E^2 - \epsilon^2} d\epsilon \; + \; \Delta f_r \qquad (2.1)$$

$$f_2(E) = \frac{E \mu(E)}{2\pi r_0 h c} \qquad (2.2)$$

---

[1] Digital Equipment Corporation

[2] Silicon Graphics Incorporated

[3] Sun Microsystems

21

where: Z is the atomic number; r_0 is the first Bohr radius; μ is the photoelectric cross-section; h is the Planck constant; c is the speed of light; E is the photon energy and ϵ is the energy for integration purposes. Δf_r is a relativistic correction factor which is usually insignificant except at very high photon energies.

We can then form the complex dielectric constant k:

$$k = 1 - \alpha - i\gamma \qquad (2.3)$$

where:

$$\alpha = \frac{r_0 \lambda^2}{\pi} N\hat{f}_1 \qquad (2.4)$$

and:

$$\gamma = \frac{r_0 \lambda^2}{\pi} N\hat{f}_2 \qquad (2.5)$$

For a compound, such as MCP glass, Henke *et al.* assure us (with the support of a great body of experimental evidence) we just have to sum the scattering factors for its constituent elements in proportion to their number density, as chemical bonds only affect the outermost electrons. $N\hat{f}_1$ and $N\hat{f}_2$ represent these averages multiplied by the number density of atoms N. Fresnel's equations for the reflected intensity of the two polarisation components σ (electric vector parallel to the reflecting surface) and π (electric vector perpendicular to the reflecting surface) are:

$$R_\sigma(\theta) = \frac{4\eta^2(sin\theta - \eta)^2 + \gamma^2}{4\eta^2(sin\theta + \eta)^2 + \gamma^2} \qquad (2.6)$$

$$R_\pi(\theta) = \frac{4\eta^2(\eta - cos\theta cot\theta)^2 + \gamma^2}{4\eta^2(\eta + cos\theta cot\theta)^2 + \gamma^2} \qquad (2.7)$$

where:

$$\eta^2 = \frac{1}{2}\left(sin^2\theta - \alpha + \sqrt{(sin^2\theta - \alpha)^2 + \gamma^2}\right) \qquad (2.8)$$

and θ is the grazing incidence angle. Finally the Fresnel reflectivity for unpolarised X-rays is:

$$R_F(\theta) = \frac{R_\sigma(\theta)}{2}\left(1 + \frac{R_\pi(\theta)}{R_\sigma(\theta)}\right) \qquad (2.9)$$

The application to the Monte Carlo codes is as follows. Before running any Monte Carlo simulation the complex dielectric constant k must be calculated for the MCP glass, at the X-ray energy we require. This constant is supplied to the ray trace code as an input parameter. Each time an X-ray impinges on a channel wall the reflectivity is calculated, using Fresnel's equations as above, then a random number $0 < n < 1$ is generated. If $n > R_F(\theta)$ the ray is deemed to have been absorbed. If $n < R_F(\theta)$, a direction for the reflected ray is generated and simulation continues.

The reflectivity calculation routine has been used to generate X-ray reflectivity versus angle curves for both Philips unreduced MCP glass ($Si_5O_{12}KNaPb$ density 3.3g/cm^3, Fraser 1982) and silica (SiO_2, density 2.2g/cm^3) which is a close approximation to the surface layer of reduced glass in a hydrogen fired MCP. Reflectivity versus grazing angle curves for all the wavelengths used in this research are shown in figures 2.1 and 2.2.

This calculation of reflectivities represents a difference in approach to that of Chapman, Nugent & Wilkins (1991), who approximate the reflectivity function in their model in one of two ways, depending on the X-ray energy. If the energy is "high" (more than 8keV) they use a step function at the critical angle θ_{crit}:

$$R(\theta) = \begin{cases} 1, & \theta < \theta_{crit} \\ 0, & \theta > \theta_{crit} \end{cases} \tag{2.10}$$

and if it is "low" (less than 200eV) they use the straight line approximation:

$$R(\theta) = \begin{cases} 1 - \theta/\theta_m, & \theta < \theta_m \\ 0, & \theta > \theta_m \end{cases} \tag{2.11}$$

where θ_m is the cut-off angle at which the reflectivity is zero. In a further paper, (Chapman, Nugent & Wilkins 1993a) they use a hybrid of the two approximations for intermediate energies. Fortunately in the Monte Carlo approach these approximations are not necessary.

2.3 Monte Carlo ray-tracing codes - common elements

Several individual programmes are used to simulate the various MCP focusing geometries available. They all have the same basic logical structure, which is as follows.

23
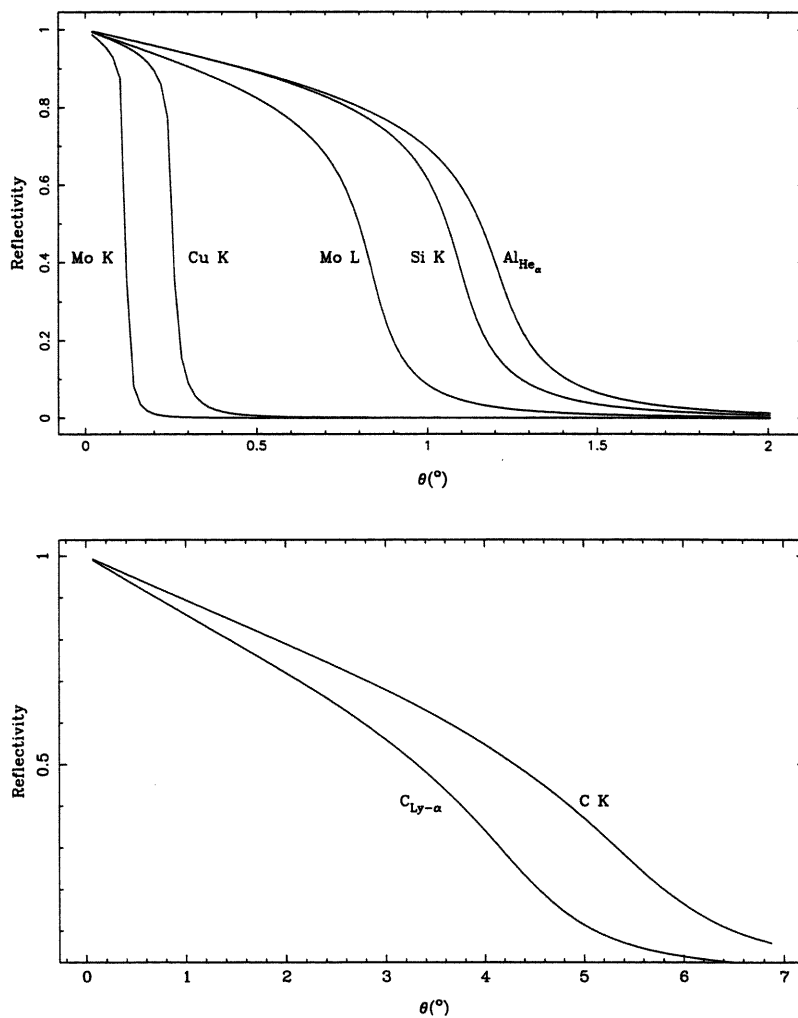
Figure 2.1: X-ray reflectivity curves for Philips unreduced MCP glass ($Si_5O_{12}KNaPb$ density $3.3g/cm^3$) Energies are: Mo K 17.4keV; Cu K 8.05; Mo L 2.29keV; Si K 1.74keV; Al_{He_α} 1.59keV (a line from He like Al XII from a laser induced plasma); $C_{Ly-\alpha}$ 0.37keV (the C VI Lyman α line also from the laser plasma); C K 0.28keV.
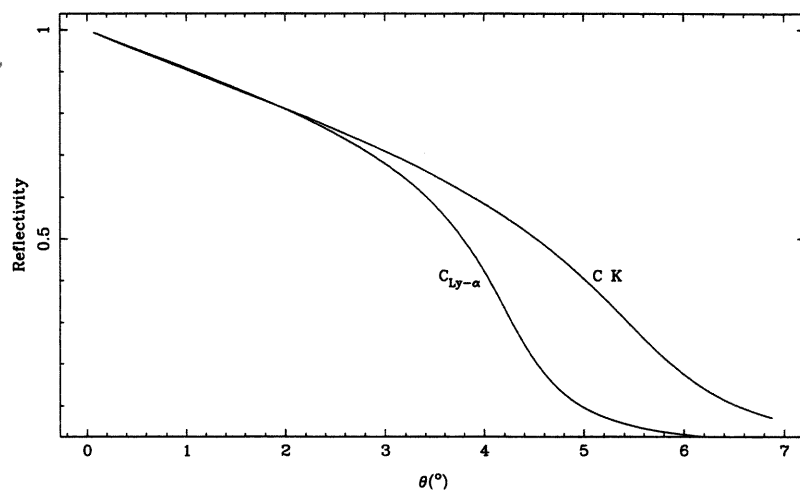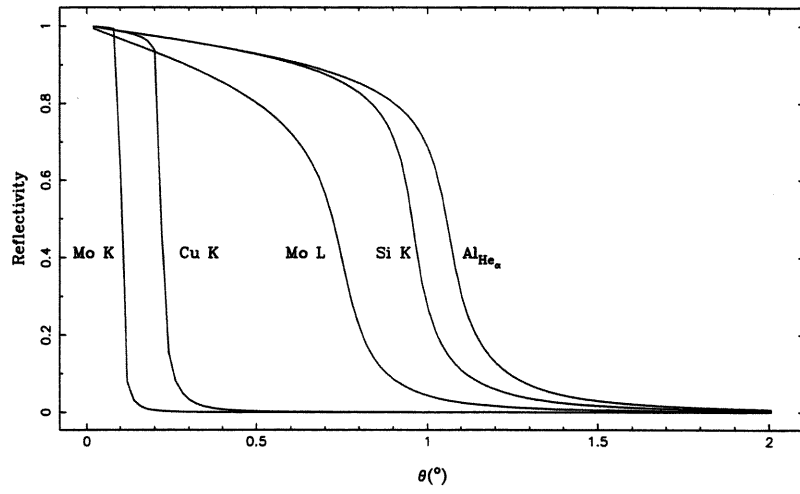
Figure 2.2: X-ray reflectivity curves for silica (SiO_2 density $2.2g/cm^3$) The line energies are as indicated in figure 2.1

1. Generate a ray at the X-ray source.

2. Find where the ray meets the front of the MCP.

3. Decide whether the ray enters a channel or not.

4. Calculate reflection positions and reflected directions as the ray goes down the channel, checking whether it gets absorbed at each reflection and whether it has passed out of the other end of the channel.

5. When the ray comes out of the channel, find the position where it hits the detector.

2.3.1 Co-ordinate origin

For each programme the origin is chosen to be the most convenient point. In the case of flat MCPs this turns out to be on the optic axis at the centre of the MCP. In the case of slumped plates, the best position to choose as the origin is the centre of curvature, as all the channel axes cross at this point. Other positions are measured relative to this origin (figure 2.3).

We need to be able to simulate both the lobster eye and beam expander geometries of section 1.4.2. The equations which define the slumped plate are, of course, the same whether the plate is in beam expander or lobster-eye mode. Hence no modification of the code is required to ray-trace either geometry, we only have to set up the source and detector positions relative to the origin and make sure that the rays propagate in the positive z-direction.

The z-axis is defined as the optic axis of the system. The conventional vectors $\mathbf{i,j}$ and $\mathbf{k}$ will be used to describe unit vectors in the x,y and z directions, respectively.

2.3.2 Generation of rays

The programmes need to be sufficiently flexible to represent the Leicester MCP test chamber (section 3.1). Hence a choice is available between a circular or an elliptical source spot, in addition to an idealised point source. Random positions within the source spot are generated, using polar coordinates. The radial position in the source spot r is found by generating a uniform

26

Flat Plate

-1_s

O

1_i

Beam Expander

O

$R_{slump}- 1_s$

R_{slump}

$R_{slump}+1_i$

Lobster Eye

$-R_{slump}$

-1_i

O

$-(R_{slump}+1_s)$

z
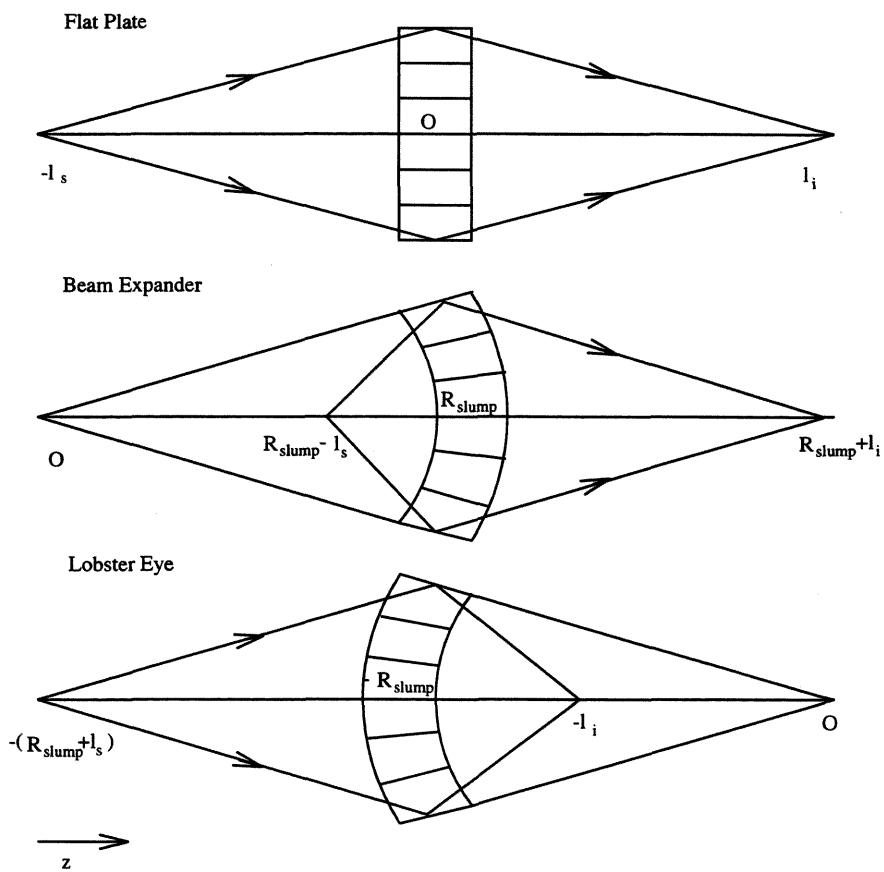
Figure 2.3: Co-ordinates used for Monte Carlo simulations

random number n where $0 < n < 1$ then $r = \sqrt{n} r_{spot}$. This weighting is necessary because as the radius increases the enclosed area increases as r^2. This gives an equal density of rays starting at any point on the spot. For the elliptical source spot positions are generated on a circle with the same radius as the semi-major axis, then any points that lie outside the ellipse are discarded.

The ray direction is generated, using spherical polar co-ordinates, with the optical axis being z. Rays are only generated over a small range of azimuthal angles θ to avoid wasting time with rays that will not hit the MCP. For this reason the θ angle is found by generating a uniform random number n where $0 < n < 1$ then $\theta = \sqrt{n} \theta_{max}$, again, because as θ increases the solid angle that the rays are going into increases as $\sqrt{\theta}$ This gives an even illumination on the channel plate. The co-ordinates are then converted from polars to Cartesians and we have a ray described by $\mathbf{r} = \mathbf{a} + t\mathbf{b}$ where $\mathbf{a}$ is the start point and $\mathbf{b}$ is a unit vector in the the ray direction.

2.3.3 Intersection of the ray with the MCP front surface

To find the point of intersection between the ray and the front surface of the MCP in the case of planar MCPs, we simply calculate where our ray $\mathbf{r} = \mathbf{a} + t\mathbf{b}$ meets the plane: $\mathbf{r}.\hat{n} = -L/2$, subject to the constraint: $x^2 + y^2 < R_{mcp}^2$, where: $\hat{n}$ denotes a unit normal vector to the front plane of the MCP; L is the channel length and R_{mcp} is the radius of the MCP. The normal vector is not simply $-\mathbf{k}$ because the MCP may have a bias angle θ_{bias} as described in section 1.2 This bias angle, means that the normal vector is given in general by $\hat{n} = -sin\theta_{bias}\mathbf{i} - cos\theta_{bias}\mathbf{k}$ where the inclination is to the yz plane.

If we are dealing with a slumped MCP then the front surface will be defined by a sphere centered on the origin (section 2.3.1). Hence we have to calculate the intersection of $\mathbf{r} = \mathbf{a} + t\mathbf{b}$ with the sphere: $\mathbf{r}.\mathbf{r} = R_{slump}^2$. Substituting for $\mathbf{r}$ gives a quadratic in t:

$$b^2 t^2 + 2\mathbf{a}.\mathbf{b}t + (a^2 - R_{slump}^2) = 0 \tag{2.12}$$

We must substitute the *smaller* solution value of t into the ray equation, to find the first time the ray meets the sphere.
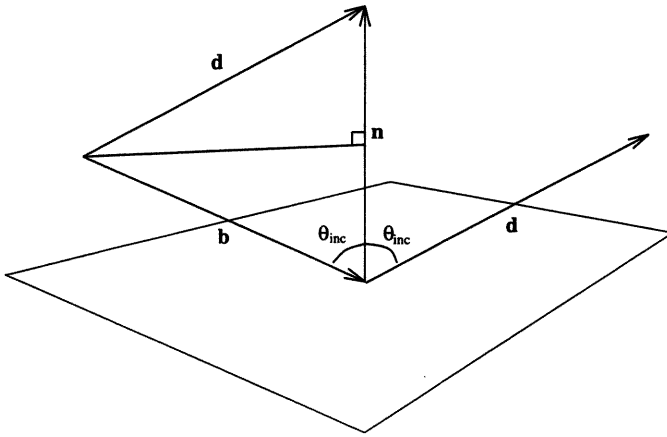
Figure 2.4: Specular reflection from a surface, $\mathbf{d} = 2\hat{\mathbf{n}}cos\theta_{inc} + \mathbf{b}$.

2.3.4 Specular reflection

When a ray, $\mathbf{r} = \mathbf{a} + t\mathbf{b}$ is reflected from a surface at a point $\mathbf{c}$, a new ray $\mathbf{c} + s\mathbf{d}$ is formed. From the construction indicated in figure 2.4 we can easily see that:

$$\mathbf{d} = 2\hat{\mathbf{n}}cos\theta_{inc} + \mathbf{b} \qquad (2.13)$$

where $\hat{\mathbf{n}}$ is a unit normal vector to the surface at point $\mathbf{c}$ and θ_{inc} is the angle of incidence, which is given by $-\hat{\mathbf{n}}.\mathbf{b} = cos\theta_{inc}$.

2.3.5 Progress of the ray along the channel

When a ray enters a channel we calculate its intersection point with the channel interior surface. Whether it is a set of planes or a cylinder, we solve the equation that defines the surface simultaneously with the ray equation $\mathbf{r} = \mathbf{a} + t\mathbf{b}$. This solution will yield some values of the parameter t which represent intersection positions. The correct one is the smallest positive one, which represents the first time the ray will meet the channel surface while going in a forward direction.

If the projection of the reflection position onto the channel axis is further than $L/2$ from the

29
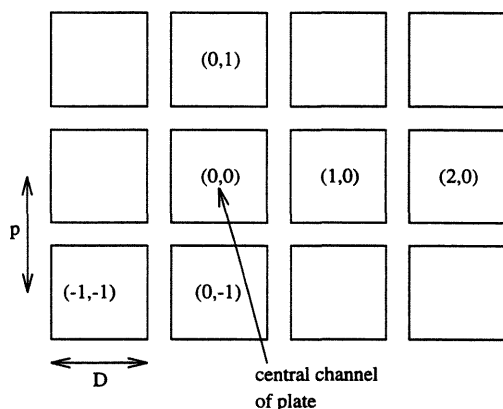
Figure 2.5: A front view of a square pore MCP showing the channel packing geometry.

channel centre then the ray has passed out of the end of the channel so we let it carry on and find where it meets the detector plane, when that ray becomes part of the image. Otherwise we test for X-ray absorption (section 2.2) and if the ray is absorbed we abandon it; if not, we calculate the reflected direction as above and iterate to find the next reflection point.

2.4 Flat square pore MCPs

Flat square pore MCPs are probably the simplest to simulate by ray tracing. The channel walls are treated as ideal planes, parallel to the z axis. The channels are packed in a regular, square array, as shown in figure 2.5. Strictly speaking, if the plate is a biased one (section1.2), the array will not be square but oblong, due to the front surface being cut at an angle to one of the channel axes. In practice, this eccentricity can be neglected, since, for an eight degree bias angle, the largest that has been encountered experimentally, the deviation from squareness is less than one percent.

The ray tracing is as described in section 2.3 until the ray hits the front of the MCP. We then have to decide whether the ray entered a channel or not.

2.4.1 Determine whether the ray goes in a channel or not

Treating the channels as being arranged on a regular square grid, there are two parameters needed to define the grid. These are the channel side length D and the channel pitch, or centre to centre distance p. This geometry gives an open area ratio of:

$$A_{open} = \frac{D^2}{p^2} \tag{2.14}$$

The process of finding which channel the ray enters is split into two parts: (i) determine which channel centre the ray ends up nearest to and (ii) determine whether the ray is close enough to this centre to actually enter the channel. The first part is dealt with by defining a central channel with its axis on the z axis of the coordinate system. The other channels are identified relative to this central one by the integers (C_x, C_y) (figure 2.5). The channel which our ray falls nearest to is given by:

$$C_x = NINT(x/p) \quad and \quad C_y = NINT(y/p) \tag{2.15}$$

Here $NINT$ is the fortran "find nearest integer" function and (x, y, z) is the position where the ray meets the front plane of the MCP.

Now if the ray actually enters this channel the logical statement

$$|C_x p - x| < D/2 \cap |C_y p - y| < D/2 \tag{2.16}$$

will be true. If not, the ray has hit the solid glass in between channels and will be absorbed.

2.4.2 Reflection position and normal

The channel is defined by four planes parallel to the xz or yz planes. Hence the t parameters and positions for intersection points, of section 2.3.5 are easily calculated as described in section 2.3.3 and the normal vector at the reflection point is just $\mathbf{i}, \mathbf{j}, -\mathbf{i}$ or $-\mathbf{j}$ depending which wall the ray hits.

2.4.3 Results

A sample ray-traced image is presented in figure 2.6. This is a simulation of an experiment performed at the Rutherford Appleton Laboratory's Central Laser Facility, using the picosecond-pulsed excimer laser plasma X-ray source. The Galileo MCP known as GEO4 (see section 3.3.1 for a description of this plate) was illuminated with 0.37keV X-rays. The source-MCP and MCP-film distances were 197mm (see section 5.4.4 for an account of the experiment and figure 5.12(b) for the actual image recorded). The glass composition modelled was SiO_2 with $\rho = 2.2g/cm^3$.

A discussion of the structures present in this image will serve to explain the focusing mechanism of square pore MCPs in a little more detail than the introduction in section 1.4.2 and also to verify the operation of the Monte Carlo code.

The rays emerging from the MCP optic can be divided into three categories (Chapman, Nugent & Wilkins 1991):

o The diffuse, or unfocused component which consists of rays which have been reflected an even number of times (including zero) both by channel walls parallel to the xz plane and by walls parallel to the yz plane.

o The one dimensionally focused component, which forms the characteristic cruxiform structure; this consists of rays which have been reflected an odd number of times by walls parallel to one axis and an even number of times by walls parallel to the other.

o The focused component which makes up the central peak; this is made up of rays which have been reflected an odd number of times by both orientations of channel wall.

In most practical focusing experiments "odd" will mean 1 and "even" will mean 0 or 2 in the great majority of cases. This is simply because it is undesirable to have more reflections than necessary as the reflectivity is always less (and often substantially less) than unity, so excess reflections diminish throughput and the geometry would be set to avoid them.

The number of counts in the three components of figure 2.6 are roughly equal. Figure 2.6(a) shows the dominance of the central peak above the cruxiform and diffuse (which is too low in
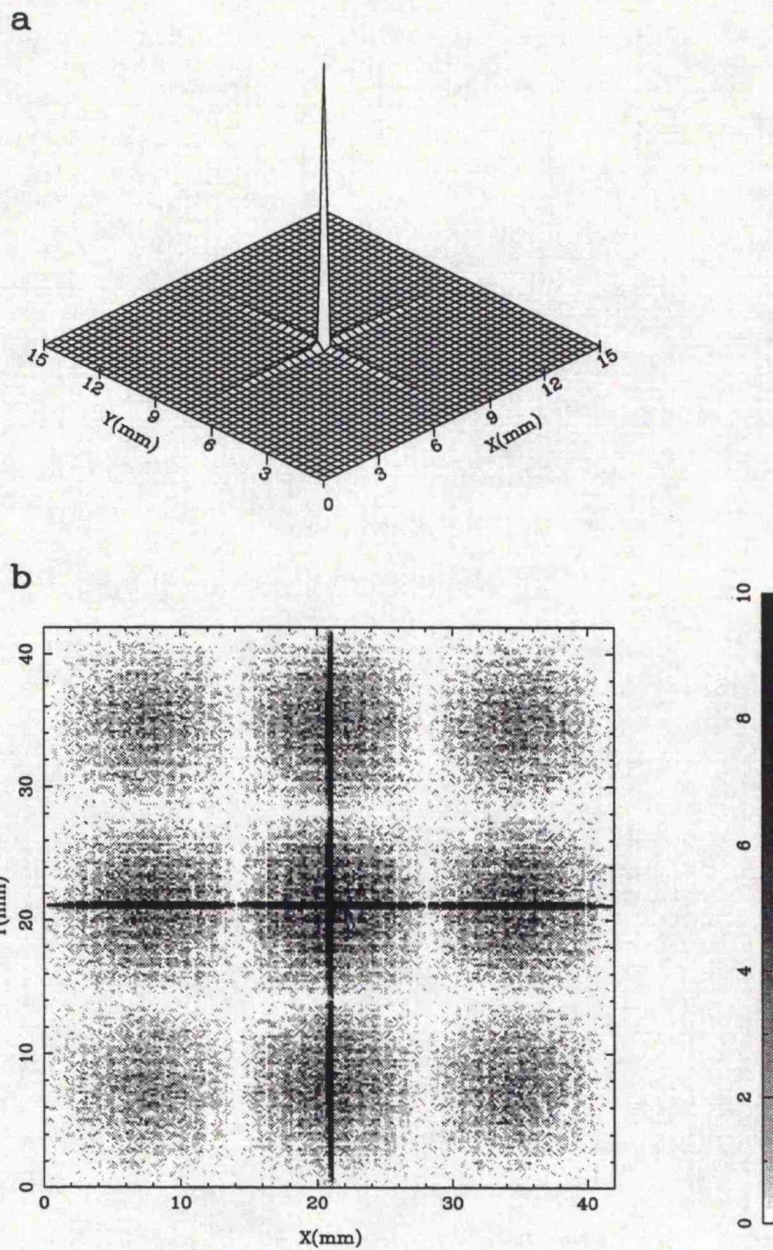
Figure 2.6: A simulation of a flat square pore MCP illuminated with 0.37keV X-rays, (a) shows the theoretical strength of the central peak above the cruxiform and diffuse components while (b) shows the low intensity "chequerboard" structure of the diffuse image component, here the cruxiform and peak components are too intense for the grey-scale used.
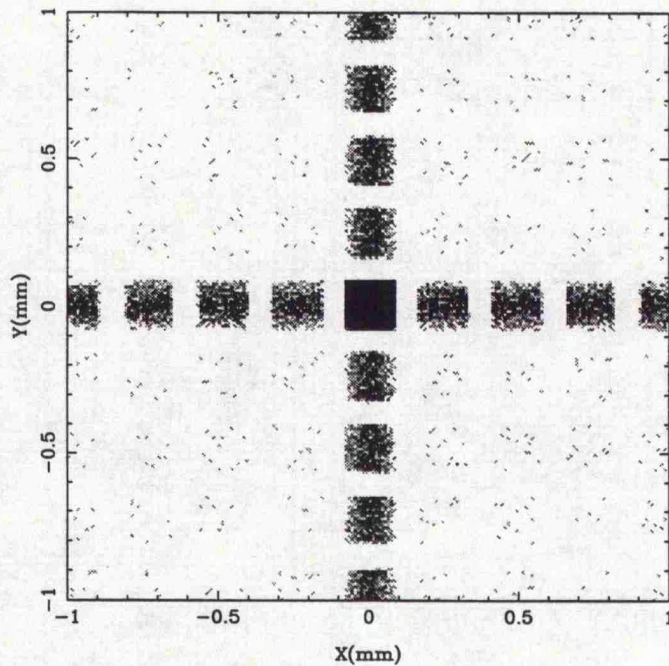
Figure 2.7: A simulation of a flat square pore MCP illuminated with 0.37keV X-rays, close up to show detail.

intensity to be seen) components. Plainly the reason for the relative intensities being so different is the relative areas that the image components occupy. The analytical model of Chapman, Nugent & Wilkins (1991) states that the width of the line foci is twice the channel side length ($2D$) and that in consequence the central focus is a square of side $2D$. The Monte Carlo results confirm this, (figure 2.7). A useful figure of merit is the "intensity gain": defined as the peak intensity of the focal spot divided by the intensity which would be recorded without the MCP in place, with the same X-ray exposure. The tight central focus leads to an intensity gain of 12000.

In figure 2.7 we see that both the line foci and the diffuse component are broken into squares of side $2D$. The explanation of this is that the inter-channel glass casts a shadow on the image plane. The image structure is twice the size that it is on the MCP because, as $l_s = l_i$, there is a $2\times$ magnification factor.

Figure 2.6(b) highlights the low level "chequerboard" structure in the diffuse component. The dark bands in the chequerboard are the regions where the rays are most efficiently reflected into

34
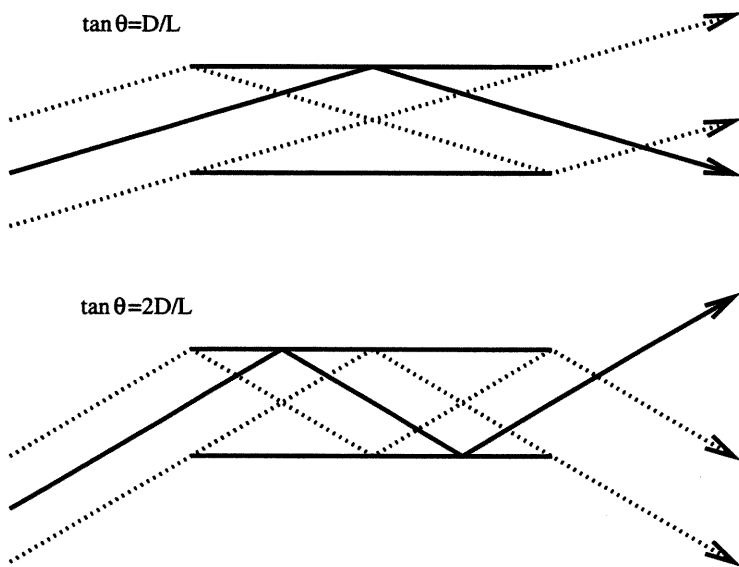
Figure 2.8: Focusing efficiency depends on incident position on the front surface of the plate. If, as in (a), $\theta = D/L$ the principal (solid) ray will be reflected towards the focus, but the dotted ray paths are prohibited. If, as in (b), $\theta = 2D/L$ the principal ray will be reflected away from the focus, and the dotted ray paths, corresponding to a focusing action, are prohibited.

the line and central foci, hence they are missing from the diffuse component. Consideration of figure 2.8 makes the reason for this clear. If the off axis distance of the channel, y, means that rays strike its walls at a grazing angle:

$$\theta = tan^{-1}y/l_s = tan^{-1}nD/L \qquad n = 1, 3, 5... \qquad (2.17)$$

then the ray will be reflected towards the focus. Conversely if

$$\theta = tan^{-1}y/l_s = tan^{-1}nD/L \qquad n = 0, 2, 4... \qquad (2.18)$$

the ray will be doubly reflected away from the focus. The reflection probabilities vary linearly between these maxima and minima making a saw-tooth type function (Chapman, Nugent & Wilkins 1991), which when combined with the reflectivity roll-off with angle, defines the diffuse intensity at a given position. In section 3.2.3 we will encounter this effect in an actual X-ray image.

In the soft X-ray region where a linear reflectivity *vs* angle function is used, the possibility of multiple reflections

2.5 Slumped square pore MCPs

The basic programme format is the same as for the flat plate. The difference is that the channels, rather than being parallel to one another are now normal to the surface of a sphere. In other words, their axes all point to a common centre. For simplicity this centre is defined as the origin.

The Monte Carlo code has been written to simulate an MCP either in telescope ("lobster eye") or beam expander mode. The source point merely has to be shifted relative to the origin, or centre of curvature, along the z axis as shown in figure 2.3 and the code, rather elegantly, works in either direction.

2.5.1 Determine whether the ray enters a channel or not

The code, up until the point where the MCP hits the spherical front surface of the MCP, is as described in section 2.3. Before we can decide whether a ray enters a channel or not we have

Square grid defining channel centres
before slumping

Distorted grid after slumping to
spherical figure
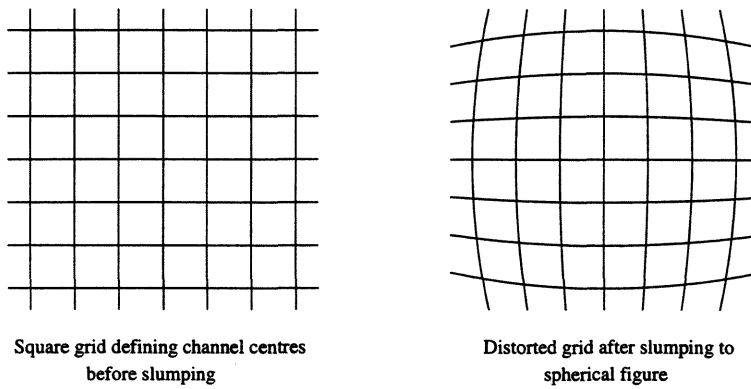
Figure 2.9: Model of the channel grid after slumping
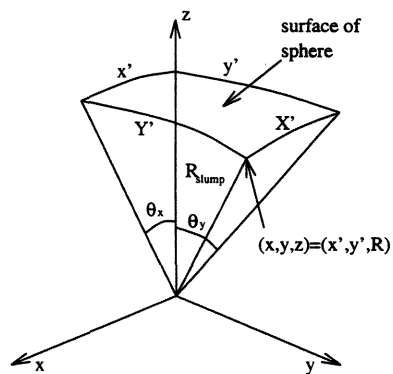
Figure 2.10: The co-ordinates used to describe slumped MCPs x', y', X' and Y' are all great-circle arcs. but, strictly, the lengths X', Y' differ from x' and y'

to address the question of what the channel array will look like. In the manufacture of slumped plates a flat MCP with a regular square array of channels is bent into a spherical figure. It is not clear what will happen to the channel array, in detail, when subjected to this treatment.

The model that I have used is that a square grid, describing the position of the channel centres on the planar front surface of a non-slumped MCP, would be subject to a barrel distortion, the centre cells being bowed outwards, while the ones at the edge are compressed (figure 2.9). I have described this situation by representing the straight lines of the original grid, after slumping, as great-circle arcs that is arcs which are centered on the centre of the sphere, inclined to the yz and xz planes by an angle proportional to their original x and y co-ordinates, so the two angles θ_x and θ_y, the inclinations to the yz and xz planes, respectively, define a position on the spherical front surface of the plate.

The co-ordinate system could be likened to a globe with four poles (north,south,east and west) rather than the conventional two, and with the lines of latitude emanating from the W and E poles as the longitude lines do from the N and S on a conventional globe. Visualising the above globe conjures up an impression of a non-linear co-ordinate system, however as we use only the central region, mid-way between the four poles, locally it is really very linear. The angular extent of the channel plate, even for soft C K (0.28keV) X-rays cannot be more than about $\pm5°$ as the reflectivity falls rapidly to zero at greater angles (figures 2.1 and 2.2). In this region the approximation implicit in the co-ordinate system, namely that with reference to figure 2.10 we say that X' and Y' are the same lengths as x' and y', when, strictly, they are not is a good one.

After making this co-ordinate change, the same method that was used for planar square pore plates can be used to determine which, if any, channel a ray entered.

2.5.2 Channel definition

The four planes which define a channel are set up as follows... The four corners of the channel, where it meets the front sphere of the MCP, are calculated by taking the point $\mathbf{p}$ where the channel axis meets the front surface and adding on increments to x' and y' to give the corners (figure 2.11):

$$\mathbf{c}_1 = \mathbf{p} + (D/2)(-\hat{\mathbf{x}}' - \hat{\mathbf{y}}')$$

(2.19)

38
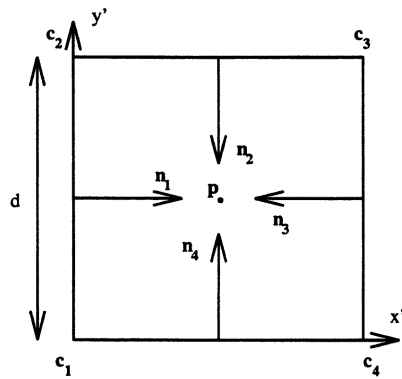
Figure 2.11: Position vectors of channel centre and corners, normal vectors.

etc, where $\hat{x}'$ and $\hat{y}'$ are unit great circle vectors, as described above. The normal vectors to the walls can be generated from the vectors C_i $(i = 1, 2, 3, 4)$.

$$n_1 = (1/2)(c_1 + c_2) - p \qquad (2.20)$$

and so on.

The channels are planes with equations of the form $r.\hat{n} = D/2$ as all the channel axes pass through the origin, so further calculations of reflection position and reflected direction are straightforward.

2.5.3 Results

An ideal lobster eye telescope has been simulated as an example of the operation of this code (figure 2.12). It is similar to the baseline MCP optic of the hard X-ray telescope described in section 1.5, 42mm in diameter with 12μm channels on a 15μm pitch, with a radius of curvature of 10m and $L{:}D{=}700{:}1$. The glass simulated is the Philips unreduced composition: $Si_5O_{12}KNaPb$, $\rho = 3.3g/cm^3$. The plate is illuminated by a parallel beam of 17.4keV X-rays.

The lobster eye focuses the parallel beam to a point, surrounded by the familiar cruxiform and diffuse components of the image. The dimensions of the plate are optimised for 17.4keV - the critical angle for reflection from the glass at this energy is 21mrad. Figure 2.13 shows that the

39
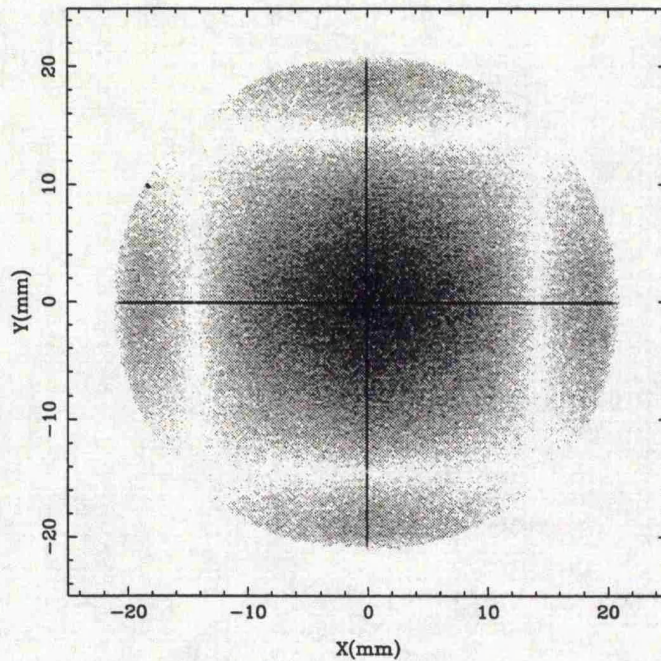
Figure 2.12: A simulation of a slumped square pore MCP illuminated with a parallel beam of 17.4 keV X-rays and focusing them to a point.

mean grazing incidence angle at a given channel position is the off axis distance, y, divided by the radius of curvature, R_{slump}, ie 21mm/10m gives a maximum grazing angle which was chosen to be equal to θ_{crit}. The ratio $D/L=1/700$ is very close to $0.021/\sqrt{2}$, the optimum aspect ratio (section 2.4.3). The peak gain in this image is 6000; the focus is only $24\mu m$ ie $2D$ wide.

The diffuse component in this image further illustrates the chequerboard pattern of section 2.4.3. Recall that in one dimension the diffuse ray distribution is a triangular saw-tooth fiction. It follows that in two dimensions it is a series of pyramids. The intensity variation of the diffuse component in the central part of figure 2.12 is just such a pyramid. Needless to say, the cruxiform and peak components of this image are much more intense than the features just discussed, so they appear as solid black on the grey-scale used.
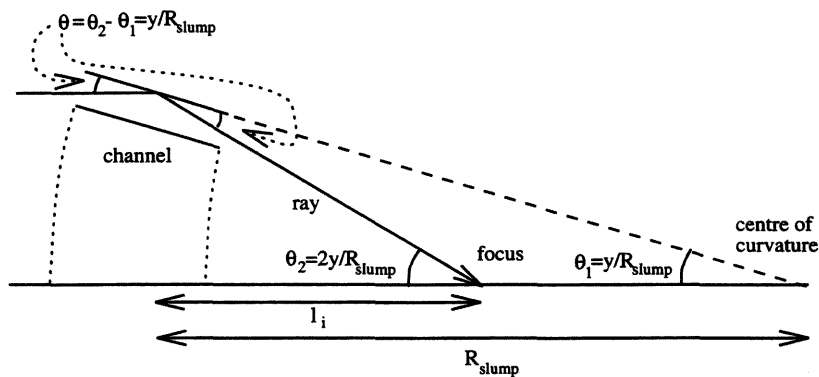
Figure 2.13: Incident angle for a lobster eye telescope, the small angle approximation $tan\theta \approx \theta$ has been made.

2.6 Flat circular pore MCPs

Very little experimental work has been done at Leicester on flat circular pore MCPs, although the Melbourne/CSIRO group has studied them to a considerable extent (Wilkins *et al.* 1989; Chapman, Nugent & Wilkins 1993b). The code described here was written both for completeness and as a precursor to writing the circular channel slumped plate code. Xiao *et al.* (1992) have developed several tricks to facilitate simulation of the circular cross-section channels of a Kumakhov lens. Some of these, particularly the fact that for a cylindrical channel all the reflections along the channel length are at the same incidence angle, also reported by Fraser (1982), could be of use here. Due to the availability, at Leicester, of fast computers, none of these algorithms have been implemented and the codes directly solve the quadratic formed by substituting the ray-equation into the equation of a cylinder. Again the code follows the common structure of section 2.3 up until the point where the ray hits the MCP.

2.6.1 Determine whether the ray enters a channel or not

The circular channels are arranged with a hexagonal packing geometry as this allows the greatest "open area ratio" of open channel area to the total area of the channel plate surface, (figure
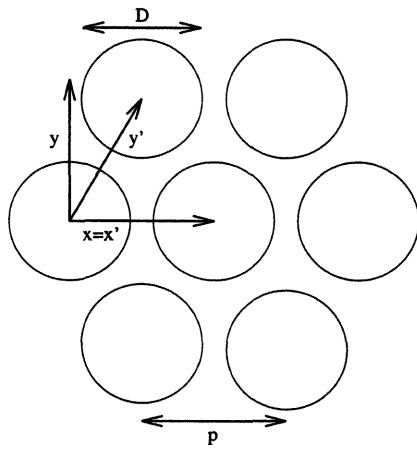
Figure 2.14: The co-ordinates needed for a round pore MCP, dictated by the hexagonal channel packing geometry.

2.14).

$$A_{open} = \frac{2\pi}{\sqrt{3}} \left(\frac{D}{2p} \right)^2 \tag{2.21}$$

This means that the channel centres do not fall on a rectangular Cartesian co-ordinate grid as they do in the case of a square pore plate. The solution to this problem is to define a new co-ordinate system $(\hat{x}', \hat{y}')$ where

$$\hat{x}' = \mathbf{i} \; ; \qquad \qquad \hat{y}' = (1/2)\mathbf{i} + (\sqrt{3}/2)\mathbf{j} \tag{2.22}$$

which as figure 2.14 shows, follows the hexagonal structure of the MCP. In $(\hat{x}', \hat{y}')$ space we have a square array and can use a similar method to the one used for square pore plates to find the nearest channel centre to the point where our ray has met the MCP surface. This has to be done by the slightly convoluted method which follows, due to the fact that the circles which define the channel mouths are elliptical in this space.

We take the position $\mathbf{r} = (x, y)$ where the ray hit the front of the MCP and convert to (x', y') as above. Then we find the four channel centres that surround this point and convert their positions $\mathbf{p}'_i$ where $i = 1, 2, 3, 4$ to regular (x, y) space $\mathbf{p}_i$. We see if $|\mathbf{r} - \mathbf{p}_i| < D/2$ for any of the channels. If so, then that is the channel that the ray entered, if not the ray fell between

channels and was absorbed.

2.6.2 Intersection of the ray with the channel wall

The channel is, of course, a right cylinder with its axis parallel to the z axis. It can be represented by an equation

$$(x - x_0)^2 + (y - y_0)^2 = (D/2)^2 \tag{2.23}$$

where x_0, y_0 are the x and y co-ordinates of the channel axis. If we write our ray $\mathbf{r} = \mathbf{a} + t\mathbf{b}$ as

$$x\mathbf{i} + y\mathbf{j} + z\mathbf{k} = (a_x + tb_x)\mathbf{i} + (a_y + tb_y)\mathbf{j} + (a_z + tb_z)\mathbf{k} \tag{2.24}$$

then substituting for x and y yields the quadratic

$$(b_x + b_y)^2 t^2 + 2\left[b_x(a_x - x_0) + b_y(a_y - y_0)\right] t + (a_x - x_0)^2 + (a_y - y_0)^2 - (d/2)^2 = 0 \tag{2.25}$$

which we must solve and then substitute the smallest positive solution value of t into the ray equation to find the point where the ray first hits the cylinder.

When we have found the reflection point $\mathbf{m}$, the normal vector

$$\mathbf{n} = (x_0 - m_x)\mathbf{i} + (y_0 - m_y)\mathbf{j} \tag{2.26}$$

is easily obtained. We can then use the standard reflecting code to work out what happens to the ray on its way down the channel.

2.6.3 Results

An image resulting from a simulation of a circular pore MCP in the same experimental set up as the square pore one described in sections 2.4.3 and 5.4.4 is shown in figure 2.15. The plate simulated had 12.5μm channels with a 15μm pitch, the $L{:}D$ ratio was 56:1 and the plate diameter 29mm; the glass composition was that of silica. Apart from the channel size (85μm on a 122μm pitch is unrealistic for a circular pore MCP) which leads to $A_{open} = 0.63$ rather than 0.49 in the case of the square channel plate, all parameters of the simulation were the same.

The first thing to note is the much broader peak; the FWHM is 0.6mm in this one whereas the central focus was square with a side length of $2D$ or 170μm. As a result of the peak being

43
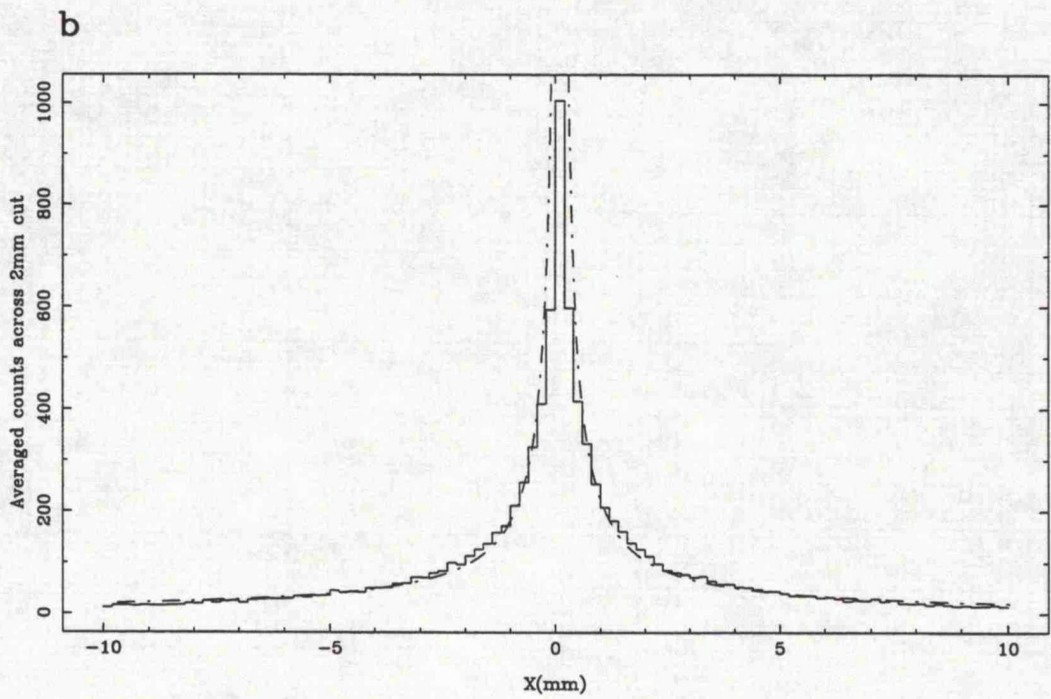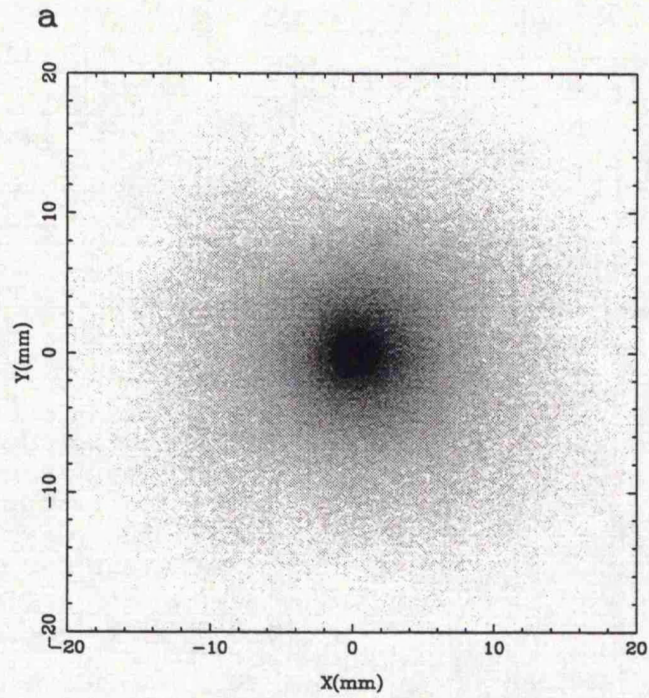
Figure 2.15: A simulation of a flat circular pore MCP illuminated with 0.37keV X-rays (a) shows the full distribution of rays and (b) is a 0.4mm thick slice across the central peak. The dashed lines in (b) represent the curve $y = A/|x|$ where A is a constant chosen for an optimum fit.

44
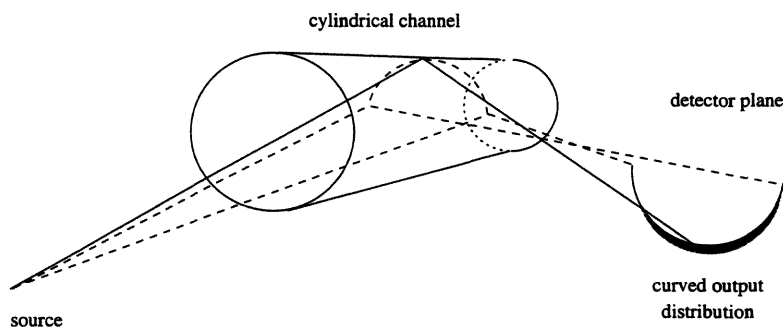
Figure 2.16: Rays reflected from a cylindrical channel form an output distribution which is a circle (or part of a circle) due to the range of azimuthal angles at which they can strike the curved surface. Here the dashed rays represent the extreme angles at which X-rays can impinge on the channel wall while the solid ray represents the centre of the distribution.

broader it is reduced in height and the peak intensity gain in this image is only 564 (cf 12000 for the square pore plate or 15500 when adjusted for the difference in A_{open}).

The reason for this difference is most easily explained with reference to figure 2.16. Rays entering a cylindrical channel can strike its curved surface at a range of angles and so be reflected in a range of directions, resulting in an output distribution of rays which is a cone, or part of a cone. Looking at the MCP from the source spot, the channels appear as circles - just the ends are visible. A ray coming from the source will meet the the wall of the channel that it enters on the side furthest from the source. If it strikes at such an angle that it appears normal to the circle representing the channel, as viewed from the source spot, it will be redirected to the central focus. If it intersects the wall away from this meridional position, it will emerge at some other angle around the output cone. There is some probability distribution of incident angles, due to variation in the solid angle subtended at different points around the channel, resulting in the circular arcs recorded where the cone meets the image plane being intense in the centre (where they intersect to form the focus) but tailing off towards the ends like the one in figure 2.16. When the arcs due to all the channels on the plate are summed, they make up the distribution shown in figure 2.15.

Chapman *et al.* (1992) report that the point spread function (PSF) for a flat, circular-pore plate should be such that $PSF(r) \propto 1/r$ according to their analytical calculations. The dotted lines on figure 2.15(b) represent a curve $y = A/|x|$ with A chosen for an optimum fit. The fit is not perfect but the mismatch is explicable in terms of the finite cut thickness (0.4mm) and pixel size (0.2mm square) and does not indicate a disagreement between the two models.

The situation is complicated by multiple reflections, though in a more subtle way than for a square pore plate. Subsequent incident angles are the same all the way along the channel, so successive bounces move the output ray around the cone described above. There is, of course, a further uncertainty in the output direction due to the channel length.

An excellent illustration of the "summing of circular arcs" described above is provided by figure 2.17. This is an actual X-ray illumination of a device made by Hamamatsu Photonics[4] with tapered circular channels 70μm in diameter at the input end, expanding to 250μm at the output (figure 2.18). $A_{open} = 0.1$ only and the device is positioned close to (50mm) the source (Brunton *et al.* 1993). Arcs due to individual channels can be resolved and the increase in intensity where they cross is clearly visible; the fact that the channels are tapered does not affect the principle of summing overlapping arcs.

2.7 Slumped circular pore MCPs

A significant fraction of the experiments presented in this thesis have been performed with round pore MCPs, slumped to a spherical figure. The results described in chapter 4 are the first reported with this type of MCP. A model was therefore needed to determine whether the results were as one would expect, or otherwise. Following the success of the square pore code, at predicting and verifying experimental results, a Monte Carlo code was written to model circular pore, slumped plates. Again, the basic format is the same as for the other programmes, particularly the round pore flat plate code. The programme, as usual, "goes its own way" at the point where we need to find whether the ray enters a channel or not.

---

[4]Hamamatsu Photonics K.K., 314-5, Shimokanzo, Toyooka-village, Iwata-gun, Shizuoka-ken, Japan.
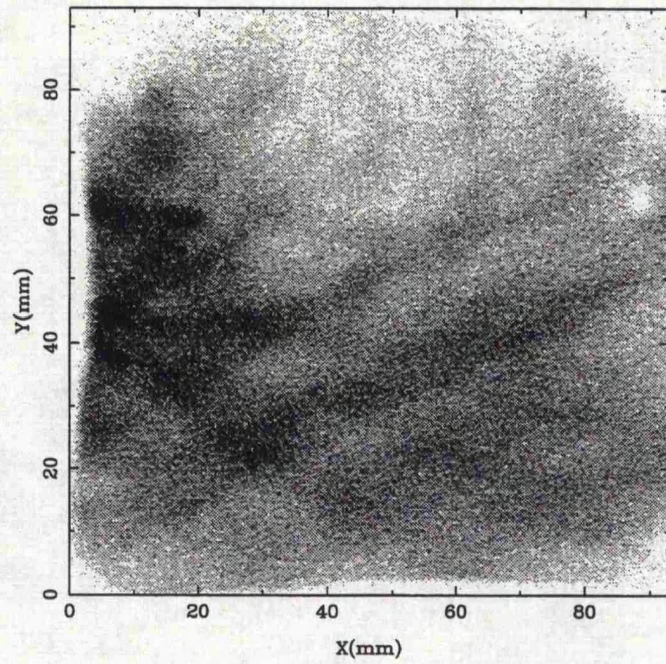
Figure 2.17: Image produced by X-ray illumination of a tapered capillary array showing circular arcs.
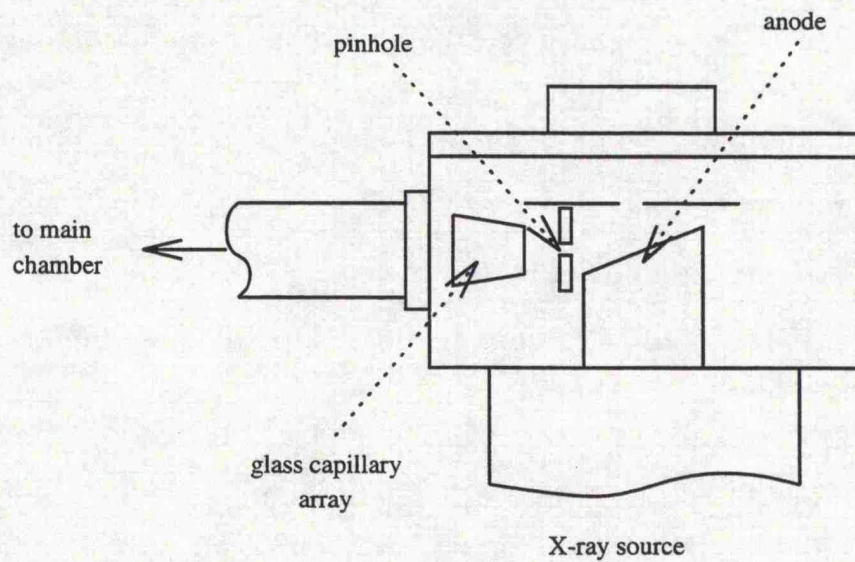
Figure 2.18: The tapered glass capillary array manufactured by Hamamatsu Photonics installed in the VTF X-ray source (section 3.1).

2.7.1 Determine whether the ray enters a channel or not

To find out whether the ray enters a channel or not, we use a hybrid of the algorithms for square pore slumped plates and round pore flat MCPs. Firstly we convert to great circle co-ordinates as described in section 2.5.1; this is needed because the plate is spherically slumped. Secondly, we use method of section 2.6.1 on the great circle co-ordinates, to determine which channel the ray enters; this is required because the slumped plate has the hexagonal packing common to all circular pore MCPs.

2.7.2 Intersection of the ray with the channel wall

The cylinder which defines the channel wall, in this case, has an axis which passes through the origin and is inclined, in the co-ordinate system of section 2.5.1 at angles θ_x, θ_y to the yz and xz planes. We can represent the channel surface by an equation:

$$\left(\frac{x - x_a}{\chi}\right)^2 + \left(\frac{y - y_a}{\psi}\right)^2 = 1 \tag{2.27}$$

where

$$x_a = z tan\theta_x \qquad y_a = z tan\theta_y$$
$$\chi = d/2cos\theta_x \qquad \psi = d/2cos\theta_y$$

We solve equation 2.27 simultaneously with the ray equation and as always take the smallest positive value of t to find the reflection point.

We can then calculate a normal vector. Referring to figure 2.19 we have a normal vector $\mathbf{n} = (\mathbf{q} - \mathbf{m})$, where $\mathbf{m}$ is the position vector of the reflection point and $\mathbf{q}$ is its projection onto the channel axis. We also have $(\mathbf{m} - \mathbf{q}).\mathbf{l} = 0$ where $\mathbf{l}$ is a vector in the direction of the channel axis. As the channel axis passes through the origin, $\mathbf{q} = \kappa\mathbf{l}$, where κ is some scalar. So substituting, we obtain $(\kappa\mathbf{l} - \mathbf{m}).\mathbf{l} = 0$, hence $\kappa = \mathbf{m}.\mathbf{l}/l^2$ and $\mathbf{n} = \kappa\mathbf{l} - \mathbf{m}$.
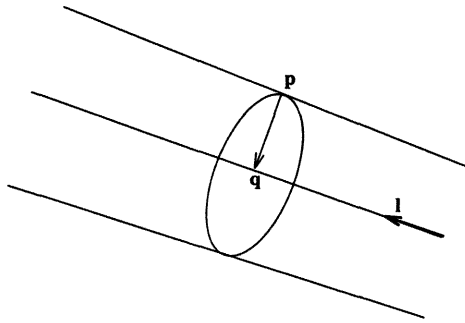
Figure 2.19: The normal vector to a cylindrical channel of a slumped MCP.

2.7.3 Results

An example of a slumped circular pore MCP being used as a beam expander for C K (0.28keV) X-rays is shown in figure 2.20. The pertinent dimensions are: $D = 12.5\mu$m; $p = 15\mu$m; $L{:}D{=}80{:}1$; $R_{slump} = 1.4$m; $R_{mcp} = 46$mm and $l_s = l_i = 0.7m$. The image is made up of two components; the parallel beam part and the diffuse component which, essentially, passes straight through the plate. These combine to give the characteristic intensity profile of figure 2.20(b).

In Fraser *et al.* (1993a) we introduced a one dimensional analytical model to verify the structure seen in Monte Carlo beam expander images such as figure 2.20 and its real-life counterparts (figures 4.1(a) and (b)). The model is basically a formalisation of the discussion of the chequerboard pattern in section 2.4.3. Although the chequerboard is a phenomenon seen in images resulting from square-pore plates, its origin is the same as that of the ring structure produced by these circular-pore ones.

With the source placed at a distance $0.5R_{slump}$ away from the MCP, on the concave side, the X-ray intensity distribution in the image plane may be approximated by:

$$I(y) = uT(uy) + S(y) \qquad (2.28)$$

where y is the off axis distance and $u = l_s/(l_s + l_i)$ is a multiplying factor to take into account the expansion of the diffuse component, T, between the MCP and the image plane. S is the reflected component which emerges parallel to the optical (z) axis. The grazing angle θ for

a

b
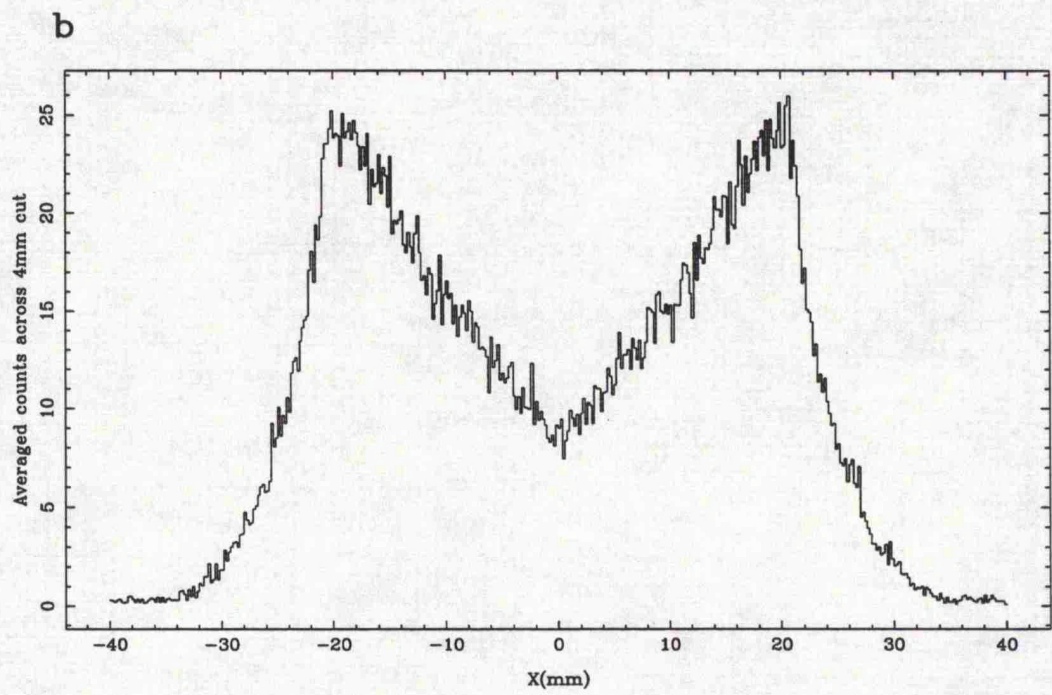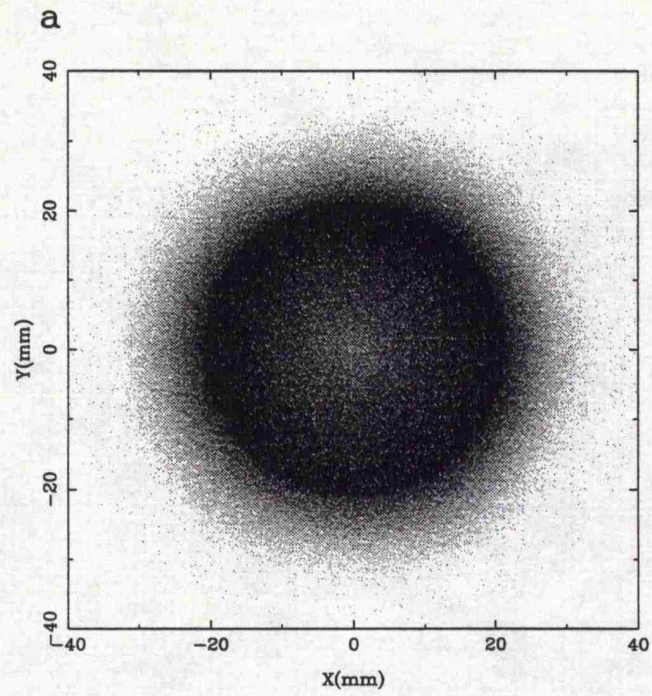
Figure 2.20: A simulation of a slumped circular pore MCP being used as a 0.28keV X-ray beam expander.

X-rays striking the channel plate a distance y from the axis is given by:

$$\theta(y) = sin^{-1}(2y/R_{slump}) - sin^{-1}(y/R_{slump}). \tag{2.29}$$

The function T is given by:

$$T(\theta) = \begin{cases} (R_F)^{n-1}\left[n - \theta/\theta_t\right]; & n-1 < \theta/\theta_t < n & n = 1,3,5,... \\ (R_F)^{n-1}\left[\theta/\theta_t - n\right]; & n < \theta/\theta_t < n+1 \end{cases} \tag{2.30}$$

where $\theta_t = tan^{-1}(D/L)$ is the "transparency angle" of the plate and R_F is the Fresnel reflectivity as calculated in section 2.2.

The function S is given by:

$$S(\theta) = \begin{cases} (R_F)^{n-1}\left[\theta/\theta_t - (n-1)\right]; & n-1 < \theta/\theta_t < n & n = 1,3,5,... \\ (R_F)^{n-1}\left[(n+1) - \theta/\theta_t\right]; & n < \theta/\theta_t < n+1 \end{cases} \tag{2.31}$$

Figure 2.21 shows the application of this model to a channel plate with the same dimensions as the one simulated by Monte Carlo means to obtain figure 2.20. Good agreement is observed between the Monte Carlo and analytical results.
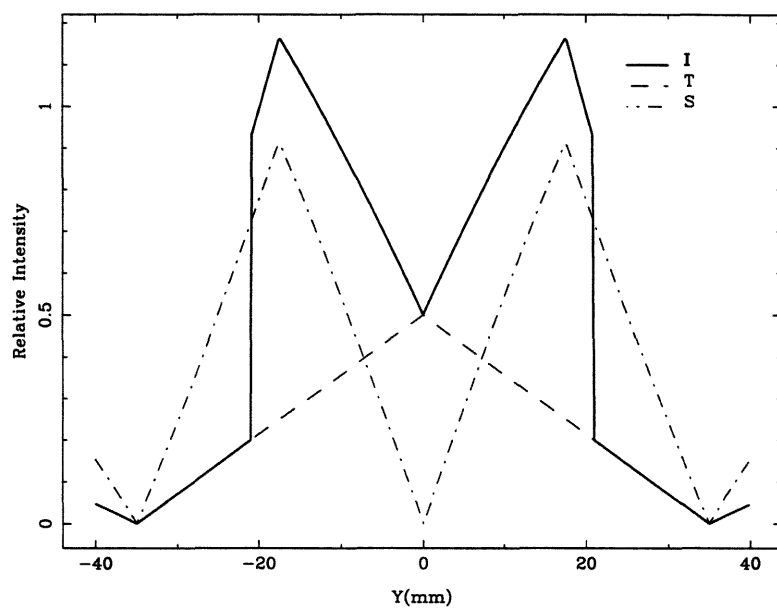
Figure 2.21: The intensity profile for the MCP simulated in figure 2.20 as produced by the 1-D model. The two components, T and S are shown, these two components are summed to form the overall distribution.

52

Chapter 3

Experimental results from square pore MCPs

3.1 The experimental set up in the Leicester Laboratory

All the data generated in the lab at Leicester came out of one test system, known as the Vacuum Test Facility (VTF). The primary use of this system is testing MCPs for X-ray detection. Currently, it is being used for testing large area, low noise, MCPs for the High Resolution Camera on NASA's Advanced X-ray Astrophysics Facility (AXAF) (Winkler *et al.* 1993). The design of the VTF is described in detail in the PhD thesis of Pearson (1984), although it has been modified slightly since its original construction.

The VTF is a turbo-molecular pumped, stainless steel vacuum chamber which generally runs at a pressure of less than 10^{-7}mbar: Such a vacuum is required for the operation of MCP detectors. The system takes about six hours to pump down to a pressure where the detector can operate without breakdown but it is generally considered to be desirable to leave it pumping overnight before applying any high voltage. Various X-ray sources can be attached to the VTF: The ones which have been used in the present research are an electron bombardment source (built in house) and a commercial Kevex[1] model K5010SMo tube.

---

[1]Kevex X-ray Inc., 320 Pueblo Road, Scots Valley, Ca 95066, USA
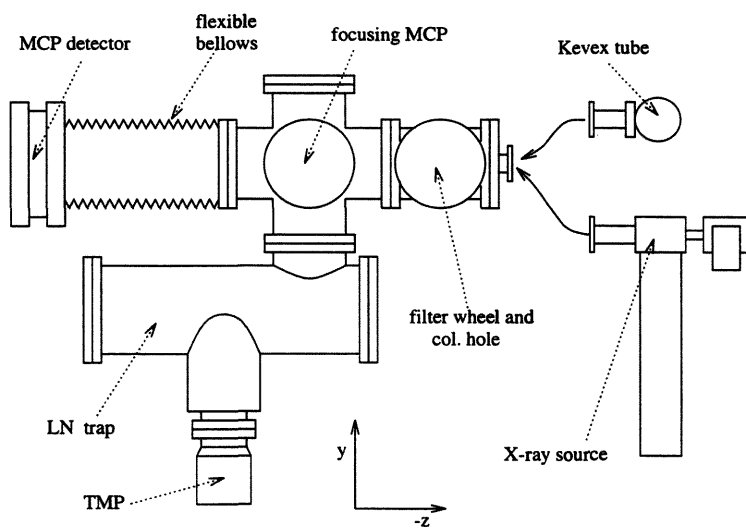
Figure 3.1: The VTF and the two X-ray sources that were used with it, see table 3.1 for relevant dimensions.

Measurement	Length(mm)
anode centre - source col. hole	10
anode centre - middle col. hole	439.5
anode centre - focusing MCP	697
anode centre - detector MCP	1386
middle col. hole - focusing MCP	257.5
focusing MCP - detector MCP	689

Table 3.1: Important dimensions within the VTF, these dimensions are the same with either of the X-ray sources in the configurations that were used for square pore experiments.

The VTF (figure 3.1) is basically tubular in construction. At one end is the X-ray source. Next to this is a "filter wheel" holding four filters any one of which can be moved in front of the source without breaking vacuum allowing, in conjunction with variation of the source HT, selection of X-ray wavelength. A mask with a 1mm diameter circular collimating hole, mounted on a linear drive, is located just on the far side of the filter wheel from the X-ray source. The mask is large enough so that when it is driven into the beam, it prevents all X-rays, apart from ones passing through the hole, from reaching the focusing and detector MCPs. The drive is calibrated so that one can tell how far from the axis of the VTF tubing the hole is. In the centre of the VTF we can fit a specially designed carriage for the focusing MCP which firmly holds MCPs of various dimensions and allows tilts of up to about ten degrees to the xz and yz planes to be set. At the opposite end to the source, a large area imaging microchannel plate detector is mounted on a 150mm inside diameter flexible bellows; it can therefore be moved in the x and y directions by plus or minus 50 millimetres, and also tilted by plus or minus 10 degrees. Some of the dimensions of the VTF are listed in table 3.1.

3.1.1 The Leicester built electron bombardment source

For a full description of the Leicester built source see Pearson (1984). This source is separated from the rest of the VTF by a polypropylene window, approximately 1μm thick, and is pumped by its own ion pump to a pressure better than 10^{-9} mbar. It is water cooled. The operation of

initial location of collimating hole

ground plane

filament

vacuum chamber

exit to VTF

plate with collimating hole as used in focusing expts.

entrance for cooling water
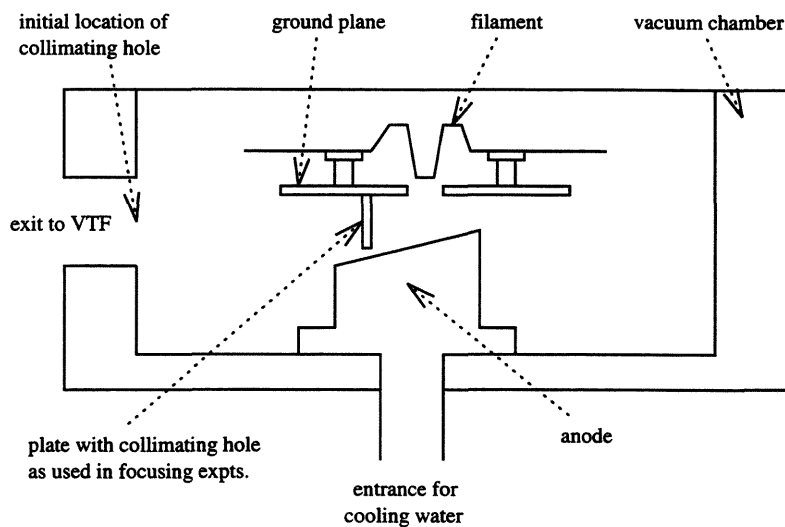
anode

Figure 3.2: The Leicester built electron bombardment X-ray source

the source is straightforward: electrons are thermionically emitted from the cathode filament, and accelerated by a potential of up to 5kV between it and the anode. (figure 3.2). The electrons pass through the hole in the ground plane and strike the anode, where they emit bremsstrahlung radiation and cause the emission of characteristic X-ray lines. The anode is made of copper and has silicon carbide deposited on it so that either silicon (1.74keV) or carbon (0.28keV) K shell X-rays can be generated by the source. Generally an accelerating voltage of about 500V would be used to generate C K X-rays and about 2kV for Si K. Variation of the HT and of the emission current can be used to alter the flux on the detector.

After the source has been in use for some time the region from which X-rays are emitted can be seen due to discolouration of the SiC. The spot is a circle of 4mm diameter. When viewed from the direction of the focusing MCP, the spot appears elliptical in projection because the top of the anode is cut at 15° to the horizontal (figure 3.2).

This spot size was deemed to be too large for characterisation of MCP optics where the expected focal spot size, for an ideal optic, is twice the channel side length; in this case approximately
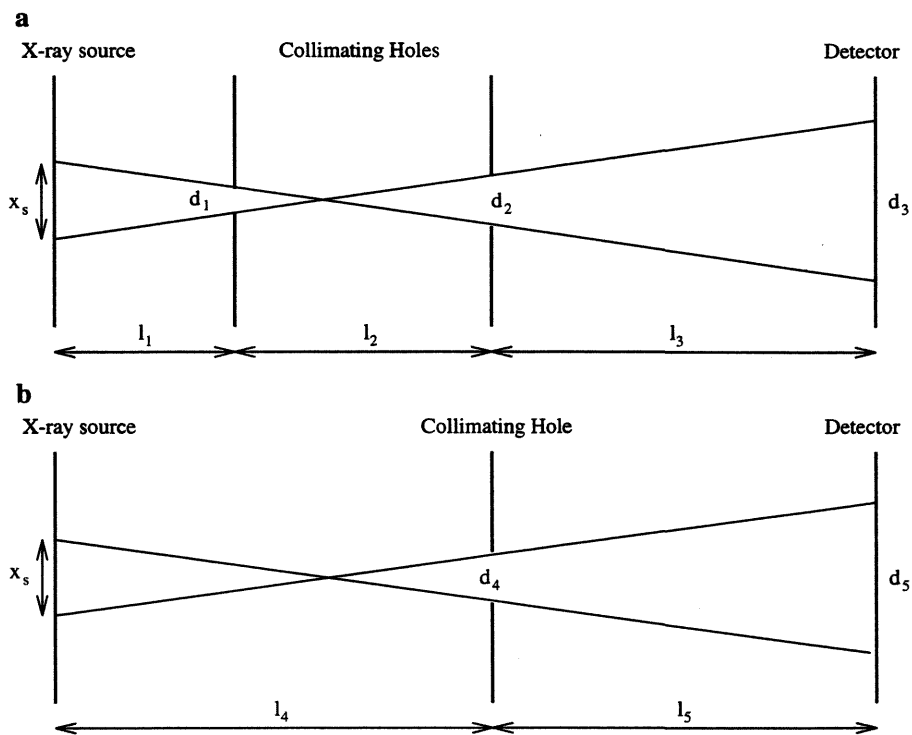
Figure 3.3: Pinhole camera constructions for the determination of source spot sizes.

200μm. It was decided that an effective source spot of 0.5mm diameter would be adequate for MCP focusing experiments. The first lab work that had to be done for this thesis was to determine what collimating hole arrangement would be required to obtain a sufficiently small effective source spot area. At the time when this work commenced there was a fixed 0.5mm collimating hole in the source, 50mm from the anode centre. The collimating hole on the linear drive (section 3.1) was used as a pinhole camera to determine the effective source diameter. Figure 3.3 (a) suggests that the spot size, x_s, is given by:

$$x_s = \frac{(l_1 + l_2)(d_3 - d_2)}{l_3} - d_2 \qquad (3.1)$$

Measurement of the pinhole camera image (figure 3.4 (a)) and application of equation 3.1 revealed that the focusing MCP was "seeing" an elliptical spot 3mm×1mm. Some attempts were made to reduce the source-spot diameter by adjusting the filament to ground plane distance by 2mm or so, which Pearson (1984) considered to have an effect on the electric field distribution between the two, and hence a focusing effect on the electrons. This had no noticeable effect, however, and neither did adjustment of the accelerating voltage throughout the available range.

It was calculated that a 100μm collimating hole located about 10mm from the anode centre (*ie* $d_1 = 100\mu$m and $l_1 = 10$mm) would restrict the amount of the source that the focusing MCP could see to a circle of approximately 0.5mm diameter, yet still allow an acceptable flux through. This was checked experimentally, indeed giving a value of 0.5mm for the spot diameter (figure 3.4 (b)) and allowing a count-rate of $2000s^{-1}$. This is the source configuration that was used to obtain all the Si K (1.74keV) and C K (0.28keV) data from the square pore plates reported below.

3.1.2 The Kevex tube

A Kevex model K5010SMo source was used for the Mo L (2.29keV), Mo K (17.4keV) and Cu K (8.05keV) experiments. The tube had a primary molybdenum target in it, from which characteristic Mo X-rays plus a bremsstrahlung continuum were excited by electron bombardment. A secondary target could be fitted which, when illuminated by the primary, would emit fluorescent K shell X-rays (the L shell fluorescence cross-section is smaller than the K shell one by a factor of about 20). By this means copper K X-rays could be generated with no continuum. The source
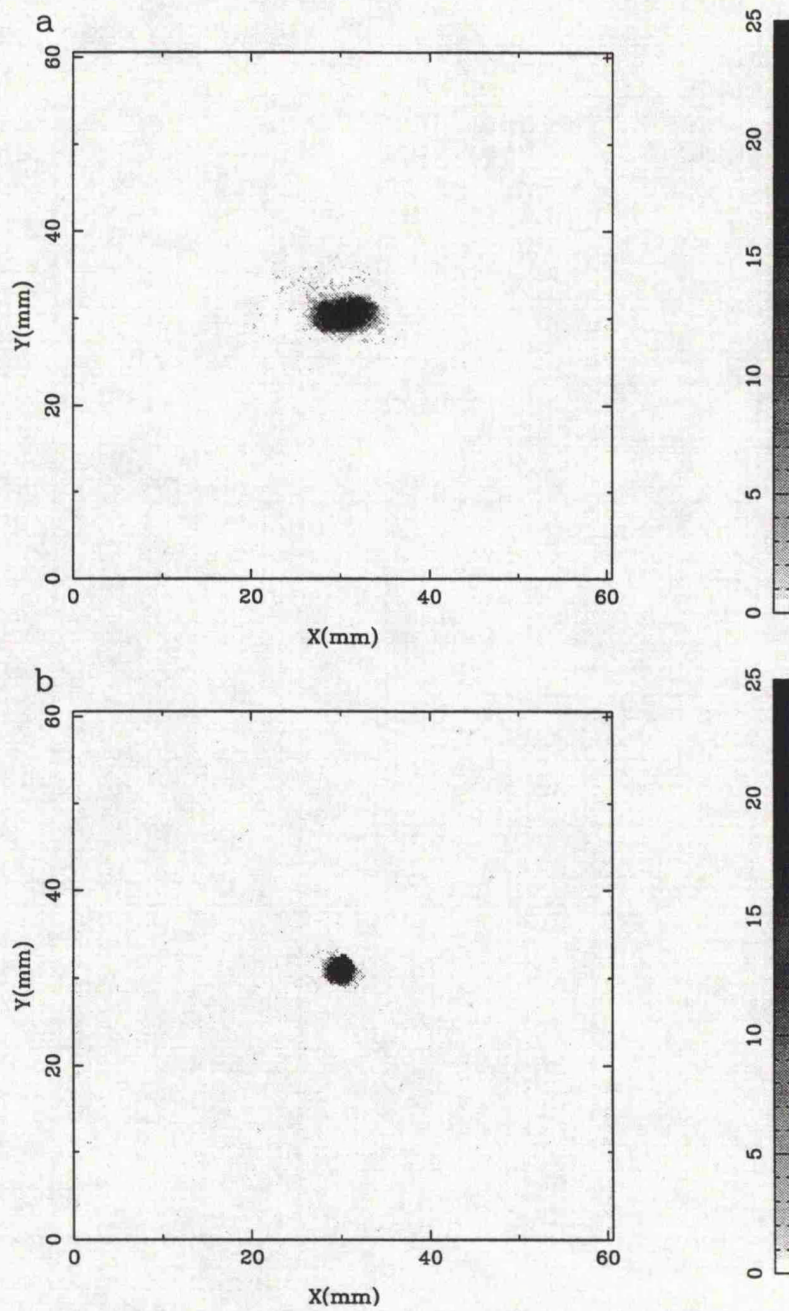
Figure 3.4: Pinhole camera images used for measurement of the source spot size. (a) with a 0.5mm collimating hole 50mm from the anode centre and (b) with a 100μm collimating hole 10mm from the anode centre.

had a 50kV power supply; the Mo K 17.4keV line was generated with an acceleration voltage of 20kV, or up to 30kV when being used to generate fluorescent Cu K X-rays from the secondary target, while the Mo L line was excited with 3.5-4kV. For the square pore experiments the Kevex tube was fitted to the VTF with tubing of such a length that its anode centre was at the same position as the anode centre of the other source had been. This source was not pumped as the tubes are supplied in a sealed, evacuated, state. A beryllium window allows the X-rays to pass from the Kevex source into the main chamber.

The spot size was calculated for this source, again using the collimating hole on the linear drive as a pin-hole camera. In neither the primary target only or primary plus secondary target configuration was any collimation used in the source. So we use the construction of figure 3.3 (b) to obtain:

$$x_s = \frac{l_4(d_5 - d_4)}{l_5} - d_4 \qquad (3.2)$$

for x_s the extent of the source spot. The source spot on the primary target was found to be a 0.8mm$\times$2.2mm ellipse with the long axis vertical. On the secondary target, the source spot was found to be roughly circular, with a diameter of 5.5mm. This large size was unfortunate and it would have been desirable to use a collimating hole in the source to reduce it, however the flux from the fluorescent target was so weak that even a moderately sized hole reduced it to a level where no image was recorded above the detector noise.

3.1.3 The filter wheel

The filter wheel holds four filters which are chosen, along with the X-ray source accelerating voltage and target, to produce reasonably "clean" X-ray lines to illuminate the focusing MCP. The filters can be changed, under vacuum, simply by turning the wheel round. The Lexan[2] silver, copper and molybdenum filters which were used for the experiments described in this thesis are listed in table 3.2 and their transmissions are plotted in figures 3.5 and 3.6.

---

[2]Lexan is a trademark of General Electric Plastics
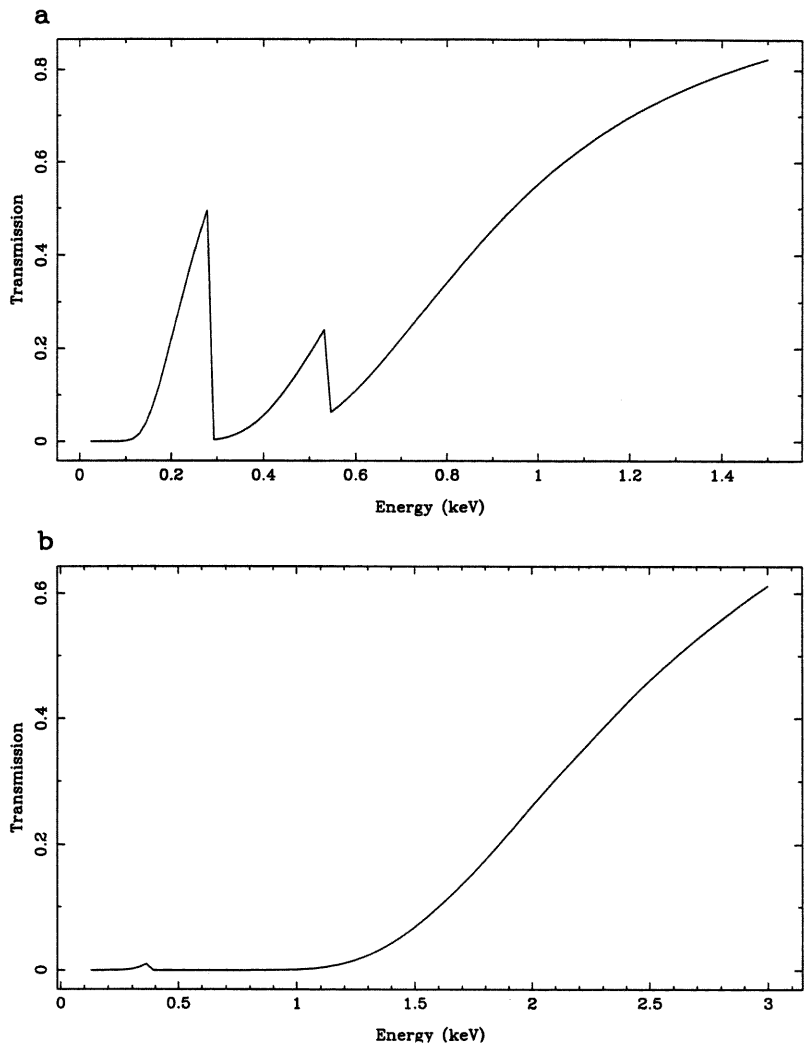
Figure 3.5: Transmissions of filters used in the VTF (a) 2μm Lexan, the polycarbonate $C_6H_{14}O_3$ and (b) 1μm silver. See table 3.2 for the lines which these filters isolate.
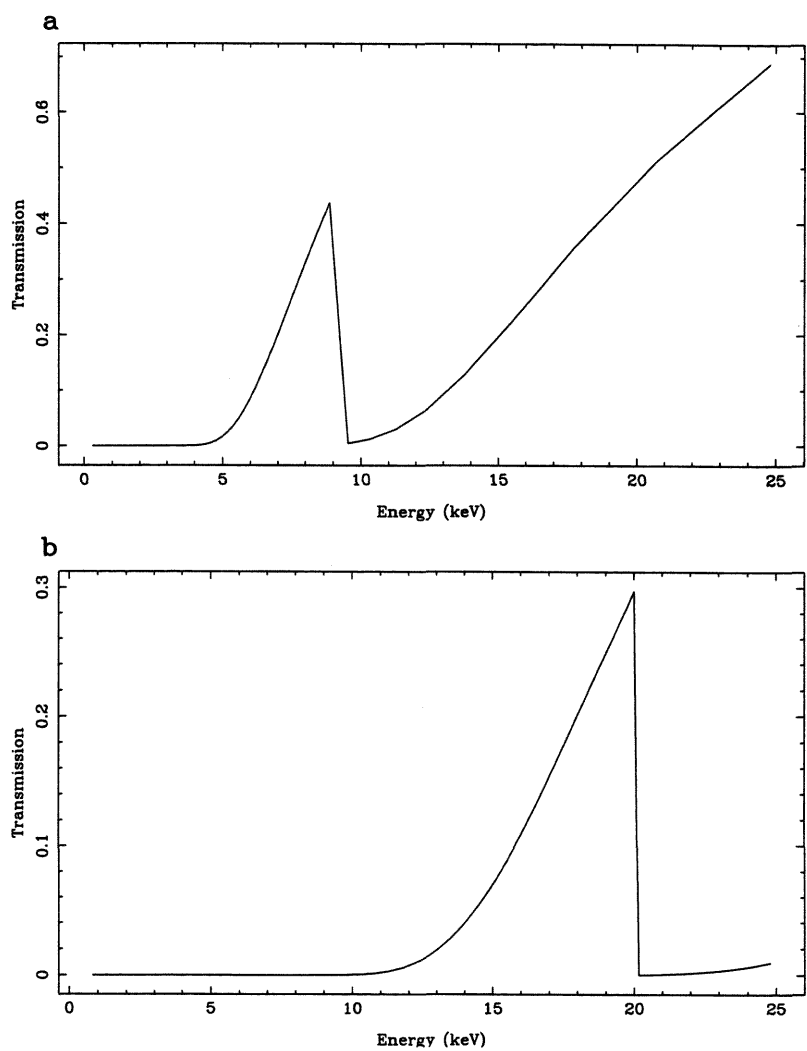
Figure 3.6: Transmissions of filters used in the VTF (a) 25μm copper, and (b) 100μm molybdenum. Table 3.2 gives the applications of these filters.

Line	Energy (keV)	Material	Thickness
C K	0.28	Lexan	$2\mu m$
Si K and Mo L	1.74 and 2.29	Silver	$1\mu m$
Cu K	8.05	Copper	$25\mu m$
Mo K	17.4	Molybdenum	$100\mu m$

Table 3.2: Filters used in the VTF during MCP focusing experiments

3.1.4 The focusing MCP mount

A device which holds a focusing MCP with its centre half way along the axis of the VTF and allows tilts with respect to both the xz and yz planes to be set, was constructed in the Leicester workshop, prior to the commencement of the research described in this thesis (figure 3.7). The device, known as the "focusing jig", can accommodate MCPs of up to 50mm diameter and 7mm thickness, by means of PCTFE[3] spacers. It fits on the 150mm flange in the middle of the VTF (figure 3.1).

When it was first built, and for the main part of this work the tilts could only be adjusted by letting the chamber up to air, removing the flange opposite and reaching inside the VTF to adjust knobs on the focusing jig. This process invariably had to be repeated several times as alignment on the bench proved very difficult, especially for biased MCPs. The most serious consequence of this need to cycle the chamber was that it was not possible to align the MCPs as precisely as one would have liked. Each cycle took a whole day and some time limit had to be set on each experiment.

Between the square pore experiments described in this chapter and the round pore ones described in the next, a pair of vacuum drives were fitted to the focusing jig, so that adjustment could be made under vacuum. This is a much more satisfactory set up, because as the MCP can be lined up while the resulting image is viewed on the screen of the computer, both the ultimate alignment and the time taken to achieve it are improved.

In its current form the focusing jig allows $+7°$ to $-6°$ tilt to the xz plane and approximately

---

[3]Poly-Chloro-Tetra-Fluoro-Ethylene, Fluorocarbon Company Ltd, Caxton Hill, Hertford, England, SG13 7NH

$\pm 9°$ tilt to the yz plane. The relationship between number of turns of the drive and tilt of the MCP is fairly linear, the xz tilt drive has been calibrated at 13.8 ± 0.7 turns/degree.

3.1.5 The large area detector (LAD)

For this work, a large active area (93mmx93mm) photon counting detector (Fraser, Barstow & Pearson 1988; Lees *et al.* 1994) has been an invaluable asset. The LAD is a development detector for the 100mmx100mm MCPs which will be central to AXAF's high resolution camera (HRC) (Murray & Chappell 1988). The detector, which has recorded all the images from the Leicester test chamber, is made up of a chevron pair of the aforementioned 100mm square MCPs, made by Philips Photonics. The MCPs have 12.5μm (circular) channels on a 15μm pitch and a $L:D$ ratio of 120:1. The active area of the detector is, as quoted above, 93mmx93mm, limited by the size of the front electrode. The chevron is read out by a uniform resistive anode and the signals from its four corners (figure 3.8) are fed into charge sensitive pre-amplifiers, then via filter amps into the Camac[4] 11bit ADCs used for digitisation. Separate lines from the pre-amps lead into a box which sums the four signals. The output of the summing amp. leads into a filter amp., then to a single channel analyser (SCA) on which upper and lower discriminator levels can be set in order to reject very large or small signals, which cause dynamic range problems in the ADCs. If the pulse is within the correct size range the SCA will "strobe" or switch on the Camac crate resulting in digitisation and transfer to an Acorn[5] Archimedes computer, of the four pulses corresponding to the event. The Archimedes saves the resulting data to disc and converts the four signals to an $x - y$ position: It displays the image on its screen as it is accumulated. The system can image at a rate of about 2000 counts per second, limited by the image capture system rather than the MCPs or resistive anode. The image resolution is 200μm. The background noise count-rate is approx $28s^{-1}$ determined by the presence of the naturally occurring radioactive isotope, potassium 40, in the MCP glass.

It is easy to see that this type of detector with its combination of: (i) good resolution; (ii) large area; (iii) instant digitisation, which facilitates computer manipulation of the image and (iv) a lack of "structure" in the image *cf* the window support mesh of an imaging proportional counter

---

[4]Kinetic Systems International, SA., 6 Chemin de Tarvernay, 1218 Geneva, Switzerland.

[5]Acorn Computers Ltd, Fulbourn Rd., Cherry Hinton, Cambridge, CB1 4JN, UK.
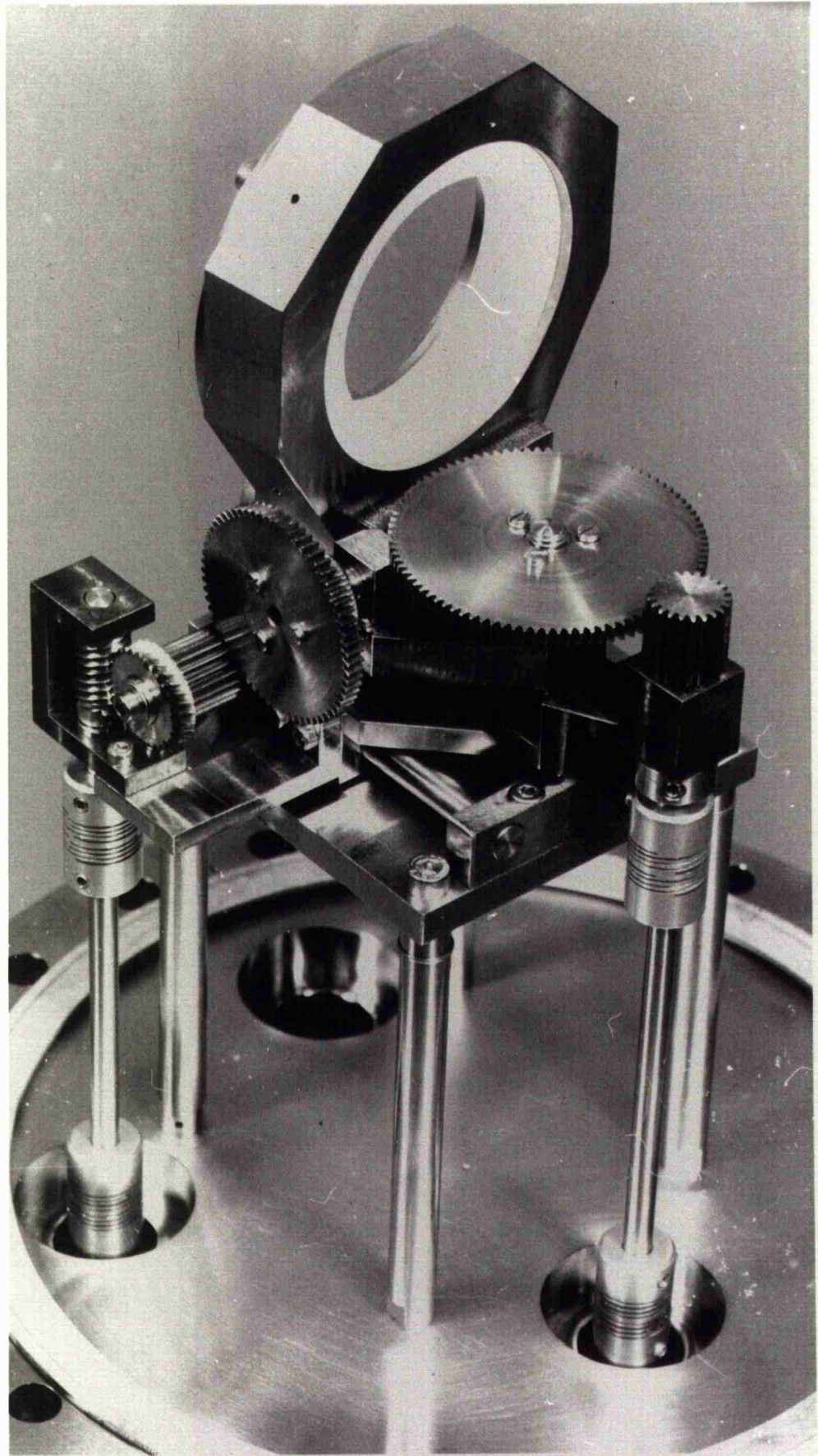
Figure 3.7: The focusing jig with vacuum drives attached.

charge sensitive preamps **filter amps** **Camac crate 4 ADCs**

from 4 corners of resistive anode

to Archimedes

strobe

summing box   filter amp   SCA
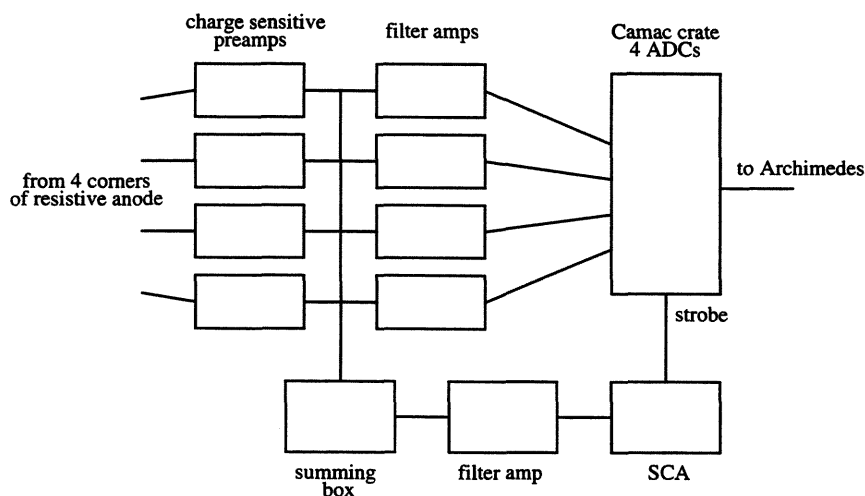
Figure 3.8: The electronics chain used to digitise the signals from the four corners of the LADs resistive anode

is ideally suited to recording images from MCP focusing experiments.

Images recorded with a resistive anode read-out exhibit distortion (Fraser & Mathieson 1981). Features near the centre tend to be expanded while regions near the edges, and particularly near the corners, tend to be squashed. This effect is due to the anode being a uniform resistive sheet with charge collected at the corners, hence charge collection for position encoding in x is not independent of collection for encoding in y. This leads to events being mispositioned in a way which is dependent on the position at which they occur. The distortion is particularly troublesome with this detector because the size of the MCPs (100mm×100mm) is comparable with that of the anode (110mm×110mm). Ideally an anode which is somewhat larger than the MCPs is used as the central region responds fairly uniformly.

The solution to the distortion problem is to make a look-up table of points on a square grid with known positions and the corresponding points recorded by the detector. This is achieved by illuminating the detector through a mask with a regular square array of pinholes, whose positions are accurately known. The image is then "linearised" by repositioning each detected

66

X-ray with reference to this table (Barstow & Sansom 1990). This technique has been applied, successfully, to the LAD so the images presented here are faithful reproductions.

3.2 Philips MCPs

3.2.1 Description

Philips Photonics manufactured a square pore boule known as LD061. Several plates from it were delivered to Leicester. They have been used in investigations into the high soft X-ray quantum efficiency and polarisation sensitivity, theoretically offered by square channel plates (Fraser *et al.* 1991a; Kaaret *et al.* 1989). Their focusing properties have also been examined. Indeed some were specially treated, by Philips, with a weak acid (sodium citrate) glass polishing etch, designed to reduce surface roughness of the channel walls and hence improve focusing efficiency. The general characteristics of these plates are: a diameter of 46mm with a "soft edge", that is channels extending right up to the edge of the MCP; an *L:D* ratio of 80:1 or 120:1; a pitch $p = 30\mu$m and a channel side length $D = 25\mu$m. These plates were designed with a large open area ratio in mind, ($A_{open} = (D/p)^2 = 0.695$). It may well be that due to this, some rigidity, and hence some channel regularity, has been sacrificed. As A_{open} and MCP rigidity both depend on wall thickness (p-D), but in opposite, senses there must be a trade-off between open area and structural regularity.

The three plates which have been tested for focusing properties all had *L:D*=80:1 and were examples of:

- A plate which had been etched only (LD061-14);

- A plate which had been etched and "hydrogen fired" (section 1.3) (LD061-2)

- A plate which had been subjected to the special polishing etch (LD061-15).

The only further differences between them were that LD061-2 was cut with an 8° bias angle, whereas the other two had channels perpendicular to the front surfaces and by the time that

X-ray testing was performed LD061-14 had had a piece broken off it for surface roughness testing with an atomic force microscope (section 6.4.2).

3.2.2 Tests

The test matrix which was established for each of these plates was as follows:

- Illuminate the full face of the plate with C K (0.28keV) X-rays.

- Illuminate the full face of the plate with Si K (1.74keV) X-rays.

- Illuminate a 2mm diameter spot on the plate with C K X-rays by placing the 1mm collimating hole and mask, first of all on the central axis of the VTF and then 5mm and 10mm off axis.

When a 46mm MCP is installed in the focusing jig it has an active diameter of 42mm set by the clear aperture of the PCTFE spacers which hold it in place. Some of the images obtained are discussed below.

3.2.3 Discussion

The full face illuminated images of figure 3.9 are typical of the images from all this batch of plates. they show four cross arms and a central focus, as one would expect, but the arms are by no means straight and the central focus is split into multiple sub-foci. All three plates showed equally bad focusing properties. There was very little difference between the 1.74keV Si K images and the 0.28keV C K ones, except that the ends of the cross arms are missing in the Si K image. This is because the reflectivity of the glass drops off much more rapidly with angle at the shorter wavelength.

The zig-zagging and divided line foci combined with multiple central foci, have been found by Monte Carlo simulation, to be symptoms of misalignment between the multifibres which make up the MCP (section 6.3).
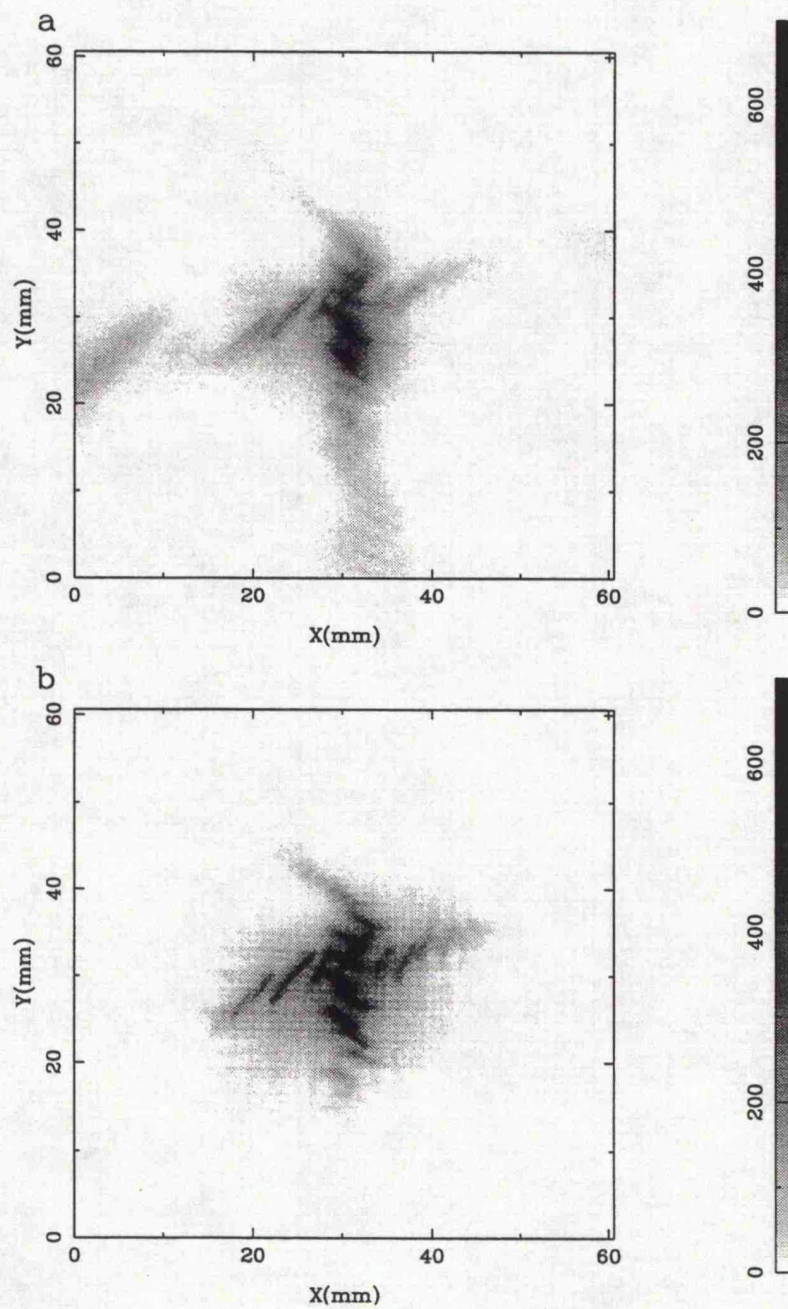
Figure 3.9: Images produced by full face illumination of Philips MCP LD061-15 (etched and polished) with (a) C K X-rays and (b) Si K X-rays. Note how the cross arms are not straight and the central focus is broken up into a series of sub-foci due to individual multifibres pointing in different directions.
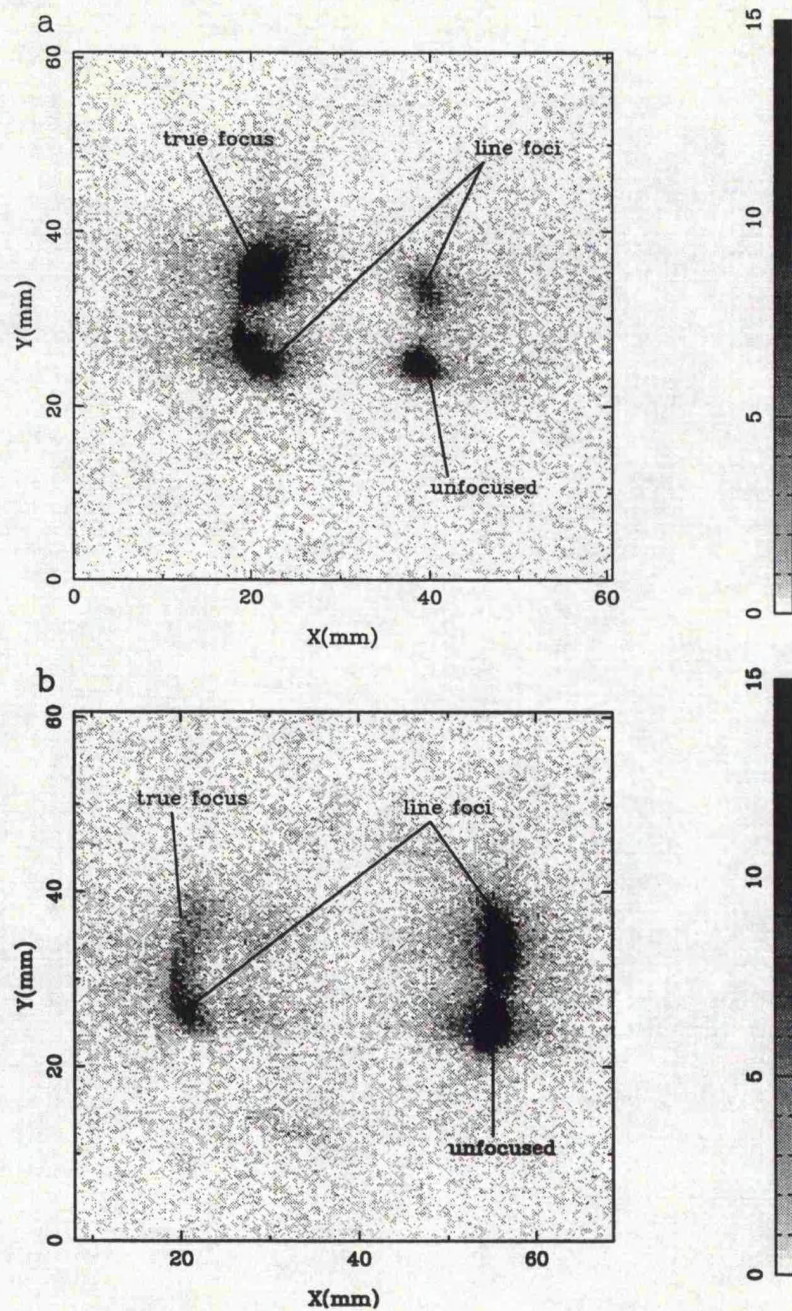
Figure 3.10: Image produced by illumination of Philips MCP LD061-14 (etched only) with C K X-rays through a 1mm diameter collimating hole (a) 5mm and (b) 10mm from the axis of the VTF. Ideally we would have two spots only because the collimating hole is off axis in the x direction only. The reason for the separation into four spots is a slight misalignment (tilt) of the focusing MCP.

The images where the plate has been illuminated through the 1mm collimating hole (figure 3.10) clearly show the four components one would expect in such an image, namely an unfocused component, two line foci and a "true" focus. Obviously, if the MCP were perfectly aligned, with the collimating hole on axis, there would just be one spot as all the rays would pass straight through the plate. The fact that there are four spots shows that (i) the channels of the plate were not lying parallel to the VTF axis (not surprising as this image was recorded in the days when vacuum had to be broken to allow any adjustment to the tilts of the MCP, hence accurate alignment was very difficult and there is a residual tilt here in one direction) and (ii) the collimating hole had been wound out from the central axis of the VTF by (a) 5mm and (b) 10mm.

The four spots are very broad, once again suggesting channel misalignment. Equation 3.1 tells us that a circular area of 1.9mm diameter is illuminated on the surface of the focus MCP. The multifibres composing these plates are 40x40 channels and the channel pitch is 30μm, hence a multifibre is 1.2mm square. We are illuminating very few (about 5) multifibres here but quite a large number of channels (about 3500). So misalignment between the individual channels is probably the main cause of broadening.

Comparing the two images, one notices that in (a) the true focus, and bottom left hand line focus are very strong, whereas in (b) they are relatively weak. The reason for this is that the incident angles of the X-rays on the plate are (obviously) different. In Fraser et al. (1993a) and in section 2.7.3 above, we describe a 1-D model of MCP focusing. This says that the foci have an intensity maximum when the incident angle of the X-rays on the front surface of the plate $\theta = D/L$ because X-rays have a good chance of reflecting once only at this angle see fig 2.21. Similarly the foci have a minimum at $\theta = 2D/L$ because the rays have a poor chance of being reflected once but a good chance of being reflected twice, or back into the diffuse spot. This MCP has $D/L = 0.0125$. When the collimating hole is 5mm from the axis the incident angle is $\theta = 0.011$radian, this is very close to the optimum focusing angle. When the off axis distance is increased to 10mm, $\theta = 0.022$radian, right in the efficiency trough. It should be noted that fall off of X-ray reflectivity with angle is a minor effect here as $\theta_{crit} = 0.075$radian for C K X-rays interacting with Philips MCP glass, see 2.1. Hence these results verify the model.

Inspection of the plates under light and electron microscopes, did not indicate particularly bad

misalignment of tiles or channels, see chapter 6.3.1. Of course inspection of the front and back surfaces of the plate does not provide any information on the alignment of the channels inside. A discussion with David Emberson of Philips Photonics, who was involved in the manufacture of these plates, revealed that the boule was "unusually twisted." Such a twisting would certainly lead to misalignment of the channel long axes and if the torsion occurred during the second draw, (section 1.3) it seems reasonable that it would affect the alignment of the multifibres more profoundly than that of the individual channels. This seems to be a reasonable explanation for the poor performance of these cosmetically good plates.

These plates should have been very interesting, due to having three different surface finishes (viz unreduced, reduced, unreduced but polished) in the same format of plate. Unfortunately the channel alignment of the plates is so poor that the effect of this distortion completely dominates the X-ray images, making it impossible to tell what effect the surface finish is having on the images.

3.3   Galileo MCPs

3.3.1   Description

Galileo Electro-Optics manufactured a boule of prototype square pore MCPs and examples of these have been exhaustively tested for X-ray focusing properties. Four plates were supplied to Leicester University, without serial numbers, so they have been designated GEO1 to GEO4. The general dimensions are: a diameter of 33mm with a soft edge (*ie* there are channels right to the edge of the pate); a square channel-side length of 85μm; a channel pitch of 122μm; and a thickness of 4.8mm, hence $L{:}D{=}56{:}1$. All the plates have a bias angle of $8°$. Two of the plates, GEO1 and GEO4, have been etched and hydrogen reduced, the other two, GEO2 and GEO3, have only been etched. These plates are thick walled - the open area ratio $A_{open} = 0.49$. It was thought that this low value for A_{open} (*cf* Philips MCPs described in section 3.2) would lead to a robust MCP with good channel alignment.

3.3.2 Tests

Plates GEO1, GEO2 and GEO4 have been tested by means of X-ray illumination. All three plates were subjected to the following investigations:

- Illuminate the full face of the plate with C K (0.28keV) X-rays.

- Illuminate the full face of the plate with Si K (1.74keV) X-rays.

GEO1 and GEO2 were further examined:

- Illuminate 2mm diameter spots on the plate with C K X-rays by placing the 1mm collimating hole and mask on the central axis of the VTF and then 5mm and 10mm off axis.

The following tests were performed on GEO1 alone

- Illuminate the full face of the plate with Mo L (2.29keV) X-rays.

- Illuminate 2mm diameter spots on the plate with Mo L X-rays by placing the 1mm collimating hole and mask on axis, then 5 and 10mm off axis.

- Illuminate the full face of the plate with Mo K (17.4keV) X-rays.

- Illuminate the full face of the plate with Cu K (8.05keV) X-rays.

3.3.3 Reduced glass MCPs GEO1 and GEO4

Figures 3.11 and 3.12 reveal the superior focusing properties of the Galileo MCP compared to those exhibited by the Philips plates. Figure 3.11 (a) clearly shows the two line foci, the central peak and the diffuse component described in 2.4.3. The cross arms are relatively straight and unbroken. The central focus is sharp to the extent that measurement of the full width at half the maximum (FWHM) is a reasonable measure of quality. This has been derived from the

73
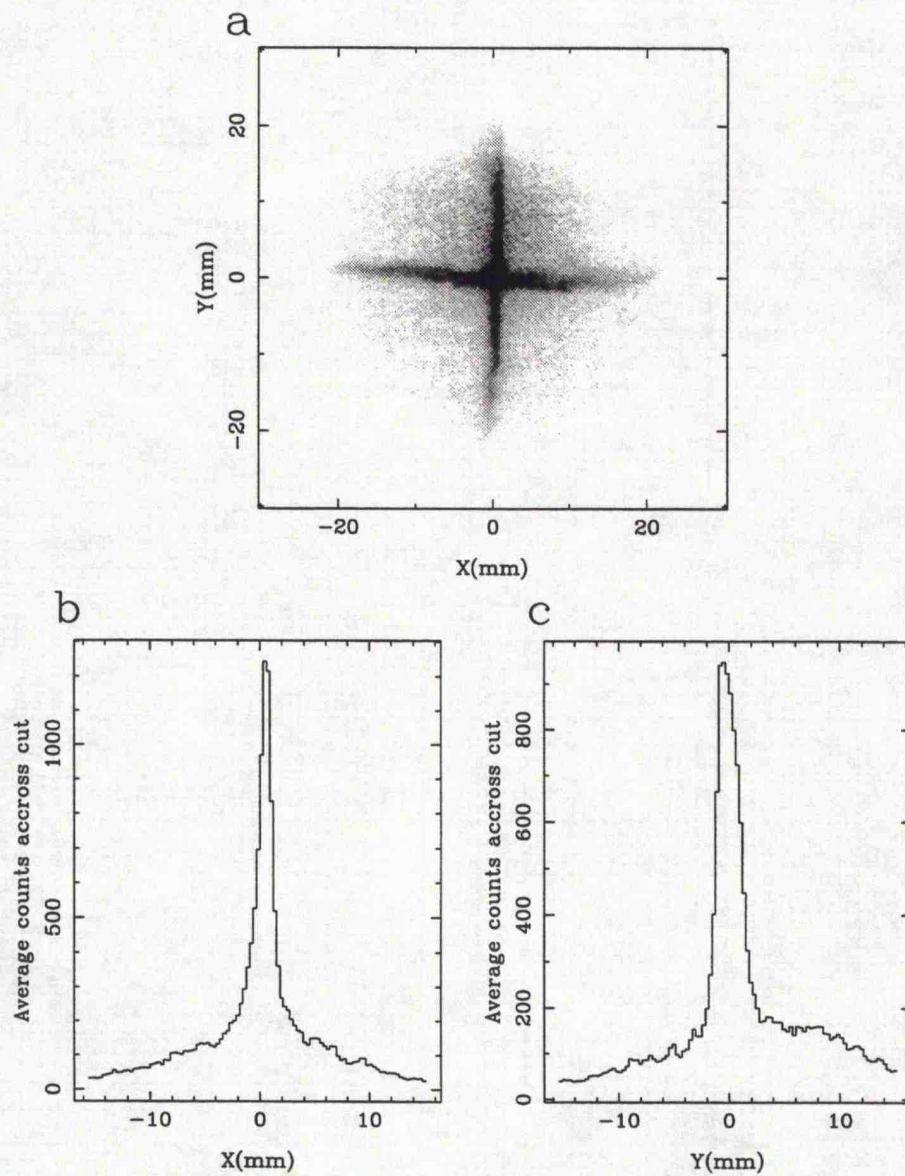
Figure 3.11: (a) Image produced by illumination of Galileo MCP GEO1 (etched and hydrogen fired) with C K (0.28keV) X-rays. (b) A cut across the x axis showing the relative intensity along the cross arm. (c) A similar cut along the y axis.

74
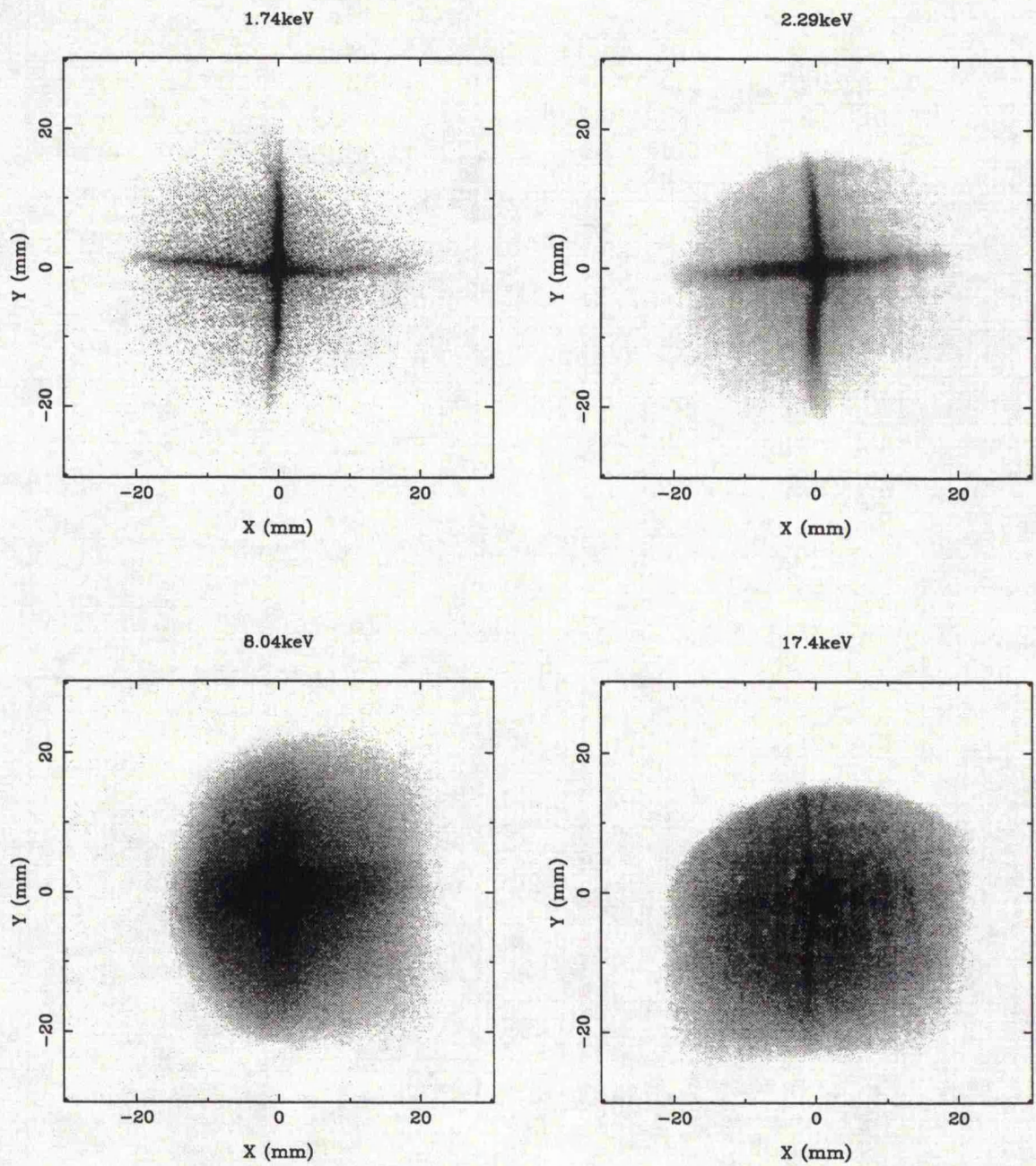
Figure 3.12: Images produced by illumination of Galileo MCP GEO1 (etched and hydrogen fired) with X-rays of various energies. Note that for the 8.0keV copper K image the source spot was very large compared to the others, hence the focus is rather broad.

cuts shown in 3.11 (b) and (c), and also from similar cuts across the images of figure 3.12. The results are presented in table 3.3.

The asymmetry in the cross arms, visible in figure 3.11 (a), is an inherent feature of the plate and is due to multifibre misalignments. The "hump" in the y-direction cross arm visible in figure 3.11 (c) is due to a variation in detection efficiency with angle of incidence on the detector MCP, this is described in detail in section 4.5.2.

The C K and Si K images were recorded at low count rates, about $200s^{-1}$, in order to avoid blurring due to "spatial aliasing". This effect occurs when two X-ray events occur close enough together temporally so that the charge from the first one has not left the resistive anode by the time the second one arrives. Hence pulses from the two merge, resulting in the two events being averaged and interpreted as a single event located in between the them (Clampin et $al.$ 1988). Comparison with similar images recorded at higher count-rates, however, seems to indicate that spatial aliasing has only a very slight effect, if any, at $1000s^{-1}$.

The C K and Si K experiments were repeated with a second reduced glass MCP, GEO4, which was found to have very similar properties to GEO1, even to the extent that the cruxiform arms exhibited similar "kinks", indicating that misalignments ran right along the MCP boule. The FWHM measurements are included table 3.3 for comparison. Results from plate GEO4 (figure 5.8) indicate structures in the cross arms which are broadly similar although different in detail, to those exhibited in images from GEO1, indicating that the misalignment varies only slightly with position along the boule, the main features seem to stretch right along it.

An attempt was made to assess the relative amount of counts in each of the components (diffuse, line foci and true focus) of the images, by simply counting the events which appeared to belong to each component. The results are presented in table 3.4, with results from a Monte Carlo simulation of an ideal plate with the same dimensions.

High energy results

Figure 3.12 shows some focusing effect at all energies, up to the 17.4keV molybdenum K line.

X-rays	FWHM_x(mm)	FWHM_y(mm)	Adj.FWHM_x(')	Adj.FWHM_y(')
C K	1.30	2.44	5.9	11.7
C K*	1.35	2.30	6.1	11.0
Si K	1.18	3.13	5.2	15.1
Si K*	1.42	2.02	6.5	9.6
Mo L	2.44	2.86	11.2	8.8

Table 3.3: FWHM of central foci in x and y directions corresponding to channel wall directions, both "raw" in mm and adjusted, by subtraction in quadrature of source size and detector resolution, in arc-minutes. Figures with an asterisk (*) indicate they are from plate GEO4, the others are from GEO1.

X-ray energy	Predicted			Measured		
(keV)	F_t	F_l	F_d	F_t	F_l	F_d
0.28	0.21	0.55	0.25	0.13	0.59	0.28
1.74	0.21	0.53	0.26	0.10	0.49	0.41

Table 3.4: Comparison of predicted (Monte Carlo) and measured image component intensities. F_t, F_l and F_d are the fractions of all X-ray events which appear in the true, line and diffuse components of the images 3.11 (a) and 3.12 (1.74keV), respectively.

The high energy results look, at first glance, rather unimpressive but in fact they are quite encouraging. Two factors have to be taken into account when considering theses images.

Firstly, when the copper K (8.05keV) image was recorded, a 5.5mm diameter source spot was being imaged by the focusing MCP (section 3.1.2). The second point that we must bear in mind is that the analytical model of Chapman, Nugent & Wilkins (1991) tells us that focusing efficiency at a given energy is a function of the aspect ratio $L{:}D$ or, conversely, at a given energy there is a unique value of $L{:}D$ which gives the maximum efficiency. This maximum occurs when:

$$\beta = \frac{L\theta_{crit}(E)}{D} = \sqrt{2} \tag{3.3}$$

Critical angles for MCP glass illuminated by X-rays of 8.0 and 17.4keV are calculated to be $\theta_{crit}(8keV) = 5$mrad and $\theta_{crit}(17.4keV) = 2$mrad. As the aspect ratio of this MCP was 56:1, the values of β are only 0.27 and 0.11 for Cu K and Mo K X-rays, respectively. This plate would, in fact, have optimum efficiency at 1.4keV.

Due to this inappropriate $L{:}D$ ratio the diffuse component has largely swamped the focused component in the 8.0keV and particularly the 17.4keV image so that no meaningful FWHM values could be measured for inclusion in table 3.3. Inspection of the 8.0keV image reveals a focus which is roughly circular and has a diameter of about 6-7mm, this is in accordance with the measurements obtained from cuts across the lower energy images when the 5.5mm diameter source-spot is subtracted off. The fact that *some* focused X-rays are present means that these are valuable, positive results. One expects the high energy operation limit of these optics to be defined by the point at which the scattering from surface roughness reaches an unacceptable level. These results imply the roughness is small enough to allow focusing at these energies, in fact the cross arms visible in the 17.4keV image, amongst the diffuse rays, appear quite sharp. This is very significant for the viability of the hard X-ray telescope whose optical requirements are described in section 1.5.

Surface finish effects

Figure 3.13 shows two images produced by illumination of plate GEO1 through the 1mm pinhole (a) with 0.28 keV X-rays and (b) with 2.3keV X-rays. The tilts of the MCP to the axes are almost the same in the two cases, as one can see from the spacings of the four spots. There are
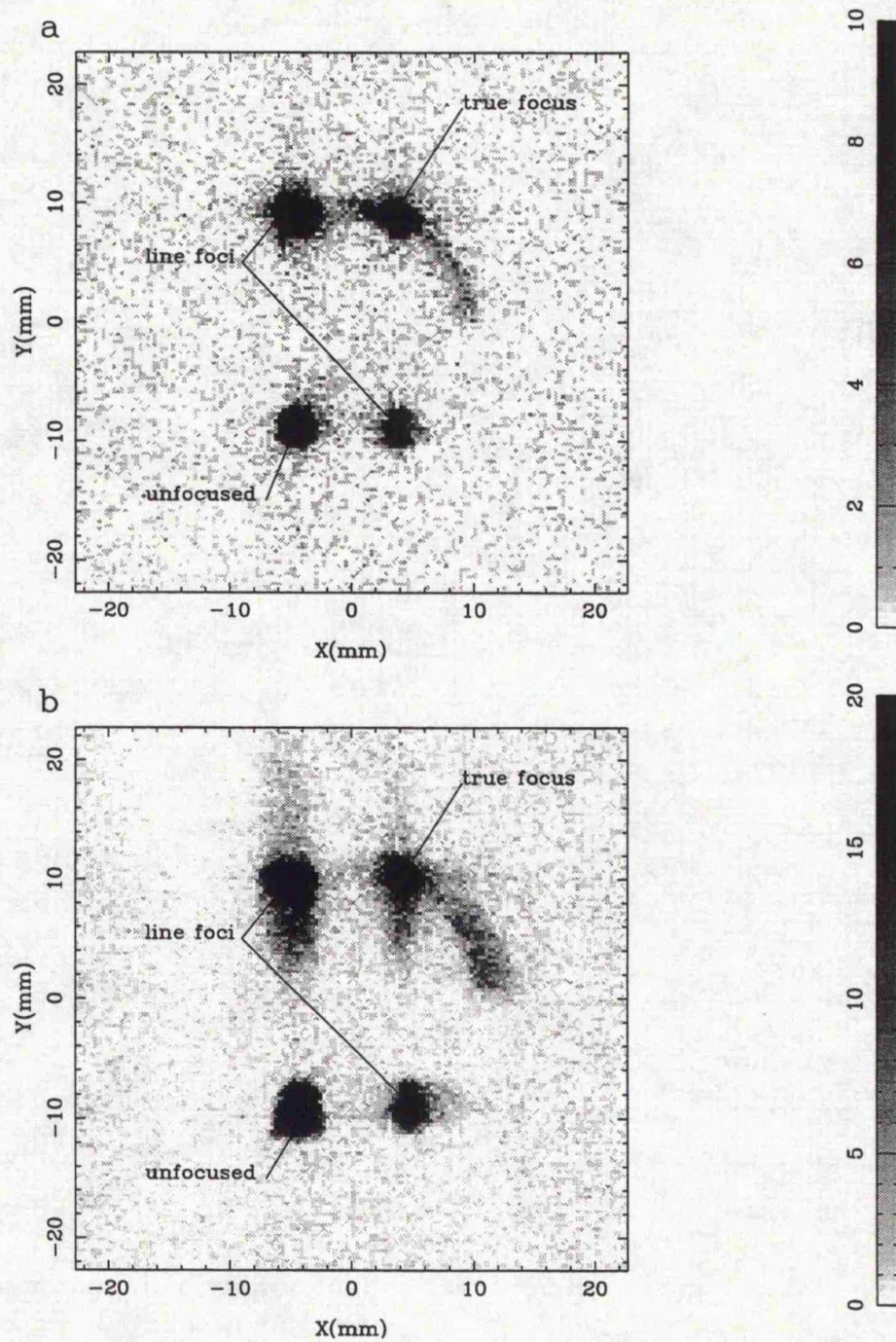
Figure 3.13: Images produced by illumination of Galileo MCP GEO1 through the 1mm collimating hole, with (a) 0.28keV and (b) 2.3keV X-rays.

some interesting features in these images:

In figure 3.13(b) we can see "scattering wings" on both the line and true foci. These are due to scattering of X-rays from surface micro-roughness. They are a well known feature of reflected beams from surfaces which are rough on the scale of the radiation wavelength. The extent of this scattering is wavelength dependent and hence it is not present in the C K image. As we move to shorter wavelengths this scattering becomes more and more of a problem, see the discussion of the high energy response from this place in the previous subsection. It warrants serious investigation and moves to reduce it, for instance the polishing etch applied to the Philips MCPs of section 3.2.

The 2.29keV image of figure 3.12 shows greater broadening of the central focus than that which would be expected by the slightly extended source spot alone. This confirms that there is scatter from surface micro-roughness on the channel walls.

Surface roughness analysis of MCPs by contact methods *eg* atomic force microscopy (AFM) is a difficult task (section 6.4.2) and analysis of the scattering wings may prove to be a valuable technique in future roughness investigations. In section 5.4.4 some preliminary analysis which was done on a similar image obtained at the RAL Central Laser Facility[6] is reported.

In both (a) and (b) we can see a curved structure near to the true focus. Experimenters at Columbia University have reported these structures in focused images from a similar MCP (Kaaret *et al.* 1992). They proposed an elaborate theory to explain them based on striations, which they observed running along the length of the channels, acting like a diffraction grating. The presence of very similar curves in these two images, despite a factor of eight difference in wavelength would appear to cast some doubt on this idea. The images suggest, instead, that it is due to some purely geometric phenomenon - pincushion distortion of the walls or the rounded-off channel corners. Scanning electron microscope (SEM) investigations performed on MCP channels at Leicester, do however, confirm the existence of the striations upon which the Columbia model is based (section 6.2).

---

[6]Central Laser Facility, DRAL Rutherford Appleton Laboratory, Chilton, Didcot, Oxfordshire OX11 0QX.
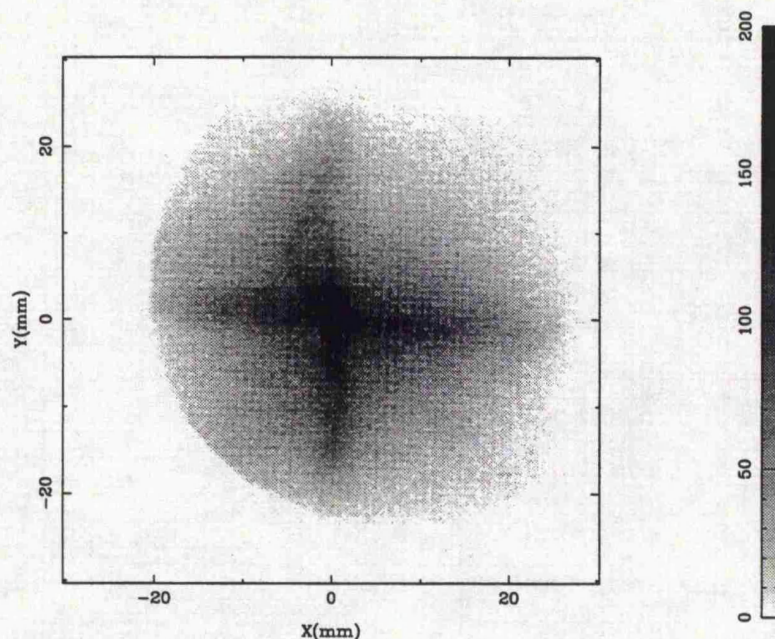
Figure 3.14: Image produced by illumination of Galileo MCP GEO2 with 0.28keV X-rays

3.3.4 Unreduced glass MCP GEO2

The results from plate GEO2, (figure 3.14) show poor focusing properties, the focus is broad, as are the cross arms. The focusing efficiency is also very poor. The image is, however, very different from the misalignment dominated images obtained with the Philips plates. At any rate this plate came from the same boule as GEO1 so one would expect the same accuracy of channel alignment. These images were initially interpreted as evidence that unreduced MCPs exhibit very rough channel surfaces. It was thought that the poor focus was caused by scattering from this roughness. The FWHM of the focus does vary with wavelength, since the 0.28keV image (figure 3.14) has a FWHM of $31.9' \times 37.9'$ yet the corresponding 1.74keV image has a FWHM of $59.8' \times 65.7'$. The central peak is so weak, however, that the slightly lower reflectivity at 1.74keV might reduce its height to the extent that it mingles with the cross-arms causing an apparent broadening, caused reflectivity rather than by scattering. AFM measurements did reveal that the surfaces of these channels were rather rough (section 6.4.2).

When plate GEO2 was examined under the SEM, it came to light that the channel opening side length D on one side was different to that on the other. This is evidence of a so called "aggressive

81

etch" at the time of manufacture, resulting in some of the cladding glass being etched away and hence a funnelling of the channels. For at least some of their length the individual channel walls are not parallel. The effect of this non-parallelism is not clear, but it will certainly be deleterious to the focus. Unfortunately, by the time the funneling was detected, the other unreduced plate, GEO3, had been cut into little pieces with a diamond saw so that the insides of its channels could be examined with the SEM and AFM (sections 6.2 and 6.4.2).

The presence of the channel funnelling means that the effect of the surface roughness, and indeed whether the roughness is any different to that of a reduced plate cannot confidently be assessed by means of X-rays. So, as in the case of the Philips LD061 plates, attempts to discover the effect of different channel surface finishes on focusing properties, were thwarted by shortcomings in the plate manufacture.

Chapter 4

Experimental results from spherically slumped, circular channel MCPs

4.1   Introduction

In chapter 1 several "milestones" in the development of MCP optics for a hard X-ray focusing telescope were outlined. Efforts towards two of them, namely (i) curving MCPs to a spherical figure and (ii) etching of "long" $L{:}D{=}320{:}1$ channels are described in this chapter. Ideally, square pore channel plates would have been slumped to the required spherical shape. Due to the lack of any such devices with the required $0°$ bias angle, and the lack of funds to commission a new square pore boule this initial proof-of-concept work has been done with 12.5μm diameter circular pore plates. All the manufacturing and slumping was carried out by Philips Photonics and the testing was performed in the VTF vacuum chamber at Leicester (section 3.1). The exact method by which the MCPs are curved is a proprietary technique of Philips; it is understood to involve elastically deforming the plate and then heating to anneal it, so the jargon "slumping" is something of a misnomer.

4.2 The MCPs

The X-ray optical properties of three slumped plates have been investigated. Initially two plates
with $L{:}D{=}80{:}1$ ie 1mm thick were supplied to Leicester. Slightly different slumping processes
had been applied to each of these although no details of the techniques were made available
by Philips. These MCPs are known by the serial numbers G12-46/DT/0/SA#1 and G12-
46/DT/0/SA#2. Some weeks later the more difficult task of slumping a plate with $L{:}D{=}320{:}1$,
which was 4mm thick was accomplished, aided by the experience gained with the thin plates.
This MCP has also been X-ray tested. It is referred to below as Slump 1-b. All three MCPs
are standard Philips stock and have not been hydrogen fired. They are 46mm in diameter with
$12.5\mu m$ diameter channels on a $15\mu m$ pitch. The composition of the glass of which they are
made is well known, it is $Si_5O_{12}KNaPb$ with a density of $3.3g/cm^3$ (Fraser 1982). The three
plates are all slumped to a nominal 1.4m radius of curvature. The slumping process does not,
however, produce perfectly consistent results nor, in its current state of development, does it
give exactly the desired radius. The radii of curvature of the plates were measured, at Philips,
by two methods.

The first technique involves the use of a microscope with a small depth of focus and a calibrated
scale for the height of the objective lens above the sample. The microscope is focused on the
MCP surface at the edge, then refocused at the centre. The calibrated scale is used to record
the height difference between the two positions, from which, by assuming a spherical figure, the
radius of curvature can be calculated using the equation:

$$R_{slump} = \frac{R_{mcp}}{8h} + \frac{h}{2} \tag{4.1}$$

where h is the sag depth. The figures for the central sag were supplied by Philips with an
error bar of $\pm 10\mu m$, presumably due to the finite depth of focus of the microscope lens. This
technique was applied to each slumped plate that was supplied; table 4.1 gives the calculated
radii of curvature for the three plates.

The second method employed at Philips was the conventional Talysurf [1] contact method, in
which a sharp point scrapes along the surface and its vertical movement is transmitted by a
system of levers to distort a piezo-electric crystal. The electrical signals from the crystal are

---

[1] Talysurf from Rank Taylor Hobson, 2 New Star Road, Leicester, U.K.

MCP	$L{:}D$	central sag (μm)	R_{slump} (m)
G12-46/DT/0/SA#1	80:1	198 ± 10	1.34 ± 0.07
G12-46/DT/0/SA#2	80:1	195 ± 10	1.36 ± 0.07
Slump 1-b	320:1	200 ± 10	1.32 ± 0.07

Table 4.1: Central sag depths and implied radii of curvature for the three MCPs used, these measurements were obtained by the non-contact method.

then converted back to relative height measurements by an electronics unit. This method was not deemed suitable for use on plates intended for use as optics due to the scratches it made on the surface (of course if the Philips personnel had considered the *modus operandi* of MCP optics they would not have worried). The Talysurf method was only used to obtain a surface profile from a third 80:1 MCP which was never delivered to Leicester. The results from this investigation are listed in table 4.2, they yield an average fractional deviation from the correct 1.4m radius spherical form of 4.8%±5.6% (one standard deviation error bar).

4.3 The experimental set-up

The experiments were performed in the VTF at Leicester. The equipment used was as described in the previous chapter (section 3.1) with two exceptions.

For the square pore experiments described in chapter 3 a piece of tubing was used to locate the anode of the Kevex tube in the same position as the anode of the Leicester built X-ray source, which is usually fitted to the system. When the Kevex tube was installed, in order to perform the tests described below this fortuitously sized pipe was unavailable and another one had to be used. This second pipe was somewhat shorter and its use resulted in modifications to the system dimensions listed in table 3.1. The measurements also differed depending on whether the primary (Mo) or secondary (Cu) target was in use. Table 4.3 gives the dimensions as used for the slumped plate experiments.

No collimating holes were used in either of the X-ray sources during the slumped plate characterisation. The focusing MCP was exposed to the full extent of each source spot. The dimensions

distance from edge (mm)	calculated sag (μm)	measured sag (μm)	
		x	y
3	3.2	4	3
5	8.9	10	9
7	17.5	19	19
9	28.9	30	29
11	43.2	43	42
13	60.4	62	63
15	80.3	87	80
17	103.2	105	103
19	128.9	131	135
21	157.5	155	157
23	188.9	176	182

Table 4.2: Measured and calculated sag depths at various distances from the centre of the plate. measurements have been made along two, orthogonal diagonals denoted by x and y. These measurements were made by the Talysurf method on an 80:1 plate with nominal $R_{slump} = 1.4$m which was not supplied to Leicester University.

	Length (mm)		
Measurement	LXRS	Kevex (Mo)	Kevex (Cu)
source spot diameter	2 × 4	0.8 × 2.2	5.5
anode centre - focusing MCP	697	687	656
anode centre - detector MCP	1386	1376	1345
focusing MCP - detector MCP	689	689	689

Table 4.3: Important dimensions within the VTF: "LXRS" refers to the Leicester built X-ray source; "Kevex (Mo)" to the Kevex tube with the Mo electron bombardment target facing the focusing MCP while "Kevex (Cu)" corresponds to the Kevex source with the Cu fluorescent target fitted.

of these spots are included in table 4.3, they were determined by the pinhole camera method described in sections 3.1.1 and 3.1.2.

4.4 Experimental geometry

The 1.4m radius of curvature for the MCPs, specified to Philips, was chosen because of the dimensions of the VTF. As l_s and l_i are more or less fixed and the system is nowhere near long enough to allow any approximation to a parallel beam illumination a decision was made to use the beam-expander geometry of section 2.7, in which equation 1.1 requires that $l_s = 0.5R_{slump}$ for $l_i = \infty$. The slight mismatches between l_s and R_{slump} depending on which MCP/source combination is in use are not important. The circular symmetry and uniformity of the output beam, which are the quantities believed to indicate the quality of the slumped MCP do not depend on the lengths being exactly correct. If l_s is a little short of $0.5R_{slump}$ the beam falling on the detector will be a little smaller than it would in the ideal case but should still exhibit good circular symmetry.

4.5   Plates with L:D=80:1

As noted in section 4.2, two plates with $L{:}D{=}80{:}1$ were supplied by Philips at the same time. They had been subjected to different slumping processes (presumably to different thermal cycles) and the Philips personnel were keen to know whether one or the other gave a noticeably better result in terms of channel alignment. These plates were illuminated with carbon K (0.28keV) and silicon K (1.74keV) X-rays both in the beam expander geometry mentioned in the previous section and with the focusing MCP reversed so that its convex side was facing the source, an arrangement which is known as "focusing mode". This work resulted in eight images, each one a record of 10^6 photons.

Figure 4.1 shows the results of illuminating these plates with C-K (0.28keV) X-rays: (a) and (b) were recorded with G12-46/DT/0/SA#1 and #2 respectively in beam expander mode; (c) and (d) were the results of illuminating plates #1 and #2 respectively in focusing mode.

4.5.1   Comparison with models

The beam expander images (figure 4.1 a and b) show good agreement with the Monte Carlo simulation described in section 2.7.3. The Monte Carlo simulation models an idealised MCP with the same dimensions as the ones described in this section.

Figure 4.2(a) shows a horizontal cut across figure 4.1(b) for comparison with figure 2.20(b) which shows a section through the Monte Carlo image. The agreement between the real and simulated image sections is very close, indicating that the slumping process worked very well.

Section 2.7.3 also describes a one dimensional model of the focusing action of a slumped MCP. Figure 2.21 shows the results of using this model to simulate the beam-expansion properties of the type of plate used experimentally. The good agreement between the two models has already been noted in section 2.7.3 and by Fraser *et al.* (1993a). It lends confidence to the analysis of these images.
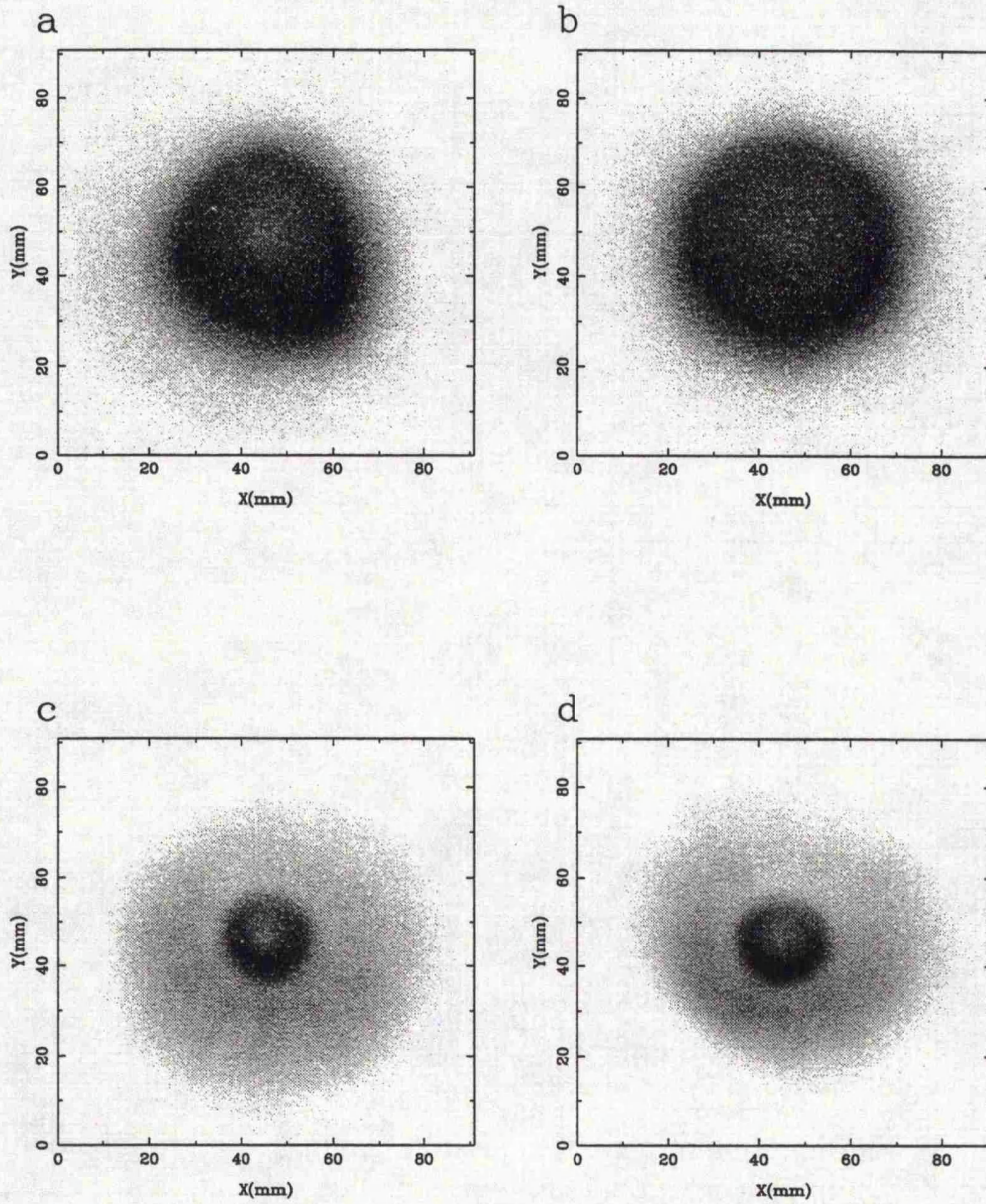
Figure 4.1: Images from plates G12-46/DT/0/SA#1 and #2, illuminated with C K (0.37keV) X-rays. (a) and (c) were recorded using plate #1, while (b) and (d) utilised plate #2, for (a) and (b) the MCPs were in the beam expander geometry and for (c) and (d) they were in focusing mode.

89
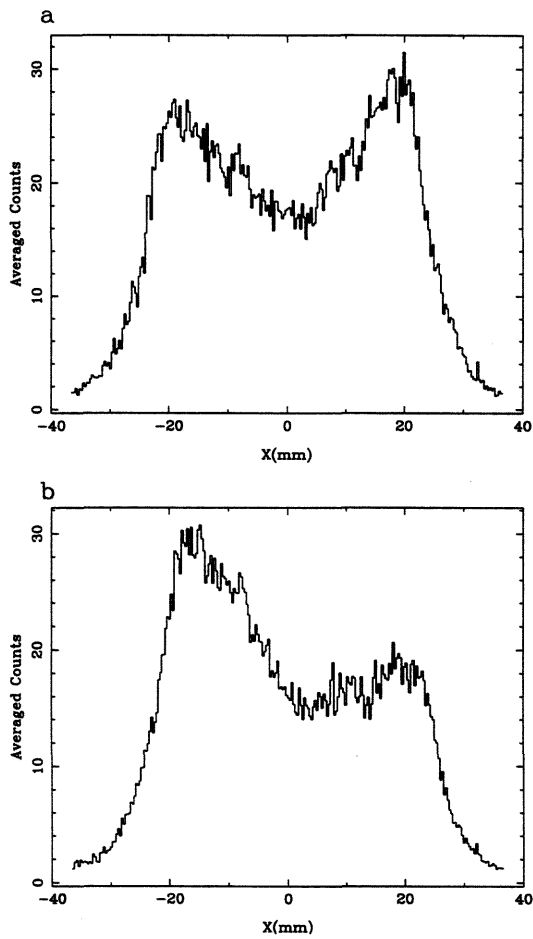
Figure 4.2: (a) horizontal and (b) vertical cuts through figure 4.1(b), plate #2 in use as a beam expander.
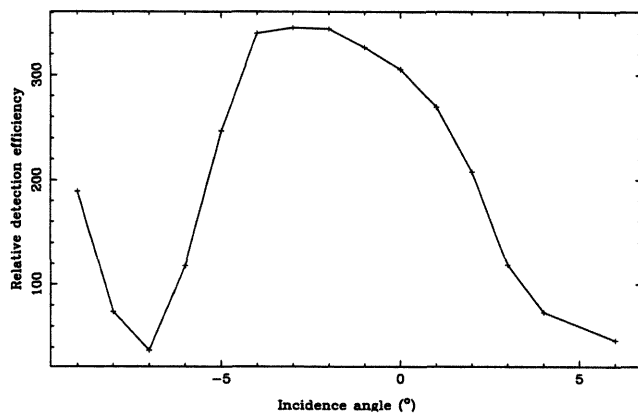
Figure 4.3: Relative detector efficiency against incident angle for 0.28keV X-rays.

4.5.2 Non-uniform detector response

Figure 4.2(b) shows a vertical section through figure 4.1(b). This plot initially caused great alarm, since it was thought that the intensity of the output beam from the slumped MCP varied greatly with position around the "doughnut".

Fortunately, there is a simple explanation for this non-uniformity: it is due to the response of the *detector* MCP varying with the angle at which photons enter its channels (Fraser *et al.* 1993a; Lees *et al.* 1994). The reason for this variation is that when a photon enters a channel parallel to its axis it can pass straight through the plate with no interaction. At small angles to the axis it can strike the channel at grazing incidence and be reflected - the very principle that MCP optics exploit. If the photon is so reflected it will not cause any ionisation and will not be detected. Conversely, at large angles of incidence photons tend to interact relatively deep within the glass, meaning that the low energy photoelectrons cannot escape into the channel for acceleration. These effects combine to generate the efficiency *vs* incident angle curve of figure 4.3 which was recorded by illuminating a small area on the detector using the collimating hole on the linear drive (section 3.1) and tilting the detector to vary the angle of incidence.

The LAD (section 3.1.5) is based on a chevron pair of MCPs. This means that there are two

91

MCPs, one in front of the other, with different bias angles, a configuration which inhibits ion feedback when operating at high gain (Wiza 1979). Conventionally, chevron detectors have a 0° bias angle plate in front and an $\sim 13°$ biased plate at the rear. In contrast, the LAD, designed as an MCP test bed for the AXAF HRC project, has a 7° biased plate *in front* and a 0° plate *at the back*. This is because the cone-angle from the 10m focal-length AXAF mirrors is so small that a 0° bias plate would have very poor quantum detection efficiency for the reflected X-rays.

The output beam from an MCP beam expander contains two basic classes of rays (section 2.7.3). Those which have passed straight through the plate without reflection diverge from the source spot to form a cone. The rays which have been reflected form a more or less parallel beam. The response to the parallel component is constant all over the plate but the diverging cone component makes an angle of up to 0.8° with the normal to the MCP. The variation in response to the divergent component is rapid in the plane containing the 7° bias angle as the incident angle adds directly to the bias. It is slow in the orthogonal plane because the sum is of perpendicular angles. This effect is clearly visible in figure 4.4 and maps through into figure 4.2. It makes the characterisation of the plates a more difficult task than it would be otherwise. Sections through the images in the x-direction (perpendicular to the channel bias direction) where detector response is relatively uniform have been used. The non-uniform detector response is also visible in the point-to-point focused images made by the square-pore plates, *eg* figure 3.11.

4.5.3   Comparison of the two plates

The images of figure 4.1 for which plate #2 was used to redirect the X-rays clearly show superior circular symmetry compared with the images where plate #1 was used. This is particularly clear in the case of the images recorded in beam expander mode. The difference between the two plates is borne out by the 1.74keV images which are not shown here. All other things being equal, the improved performance of plate #2 must be due to its channels being aligned more closely than those of plate #1 with the idealised radial geometry that we would hope for. This was duly reported to the relevant Philips personnel to aid them in their efforts to curve a thick plate.
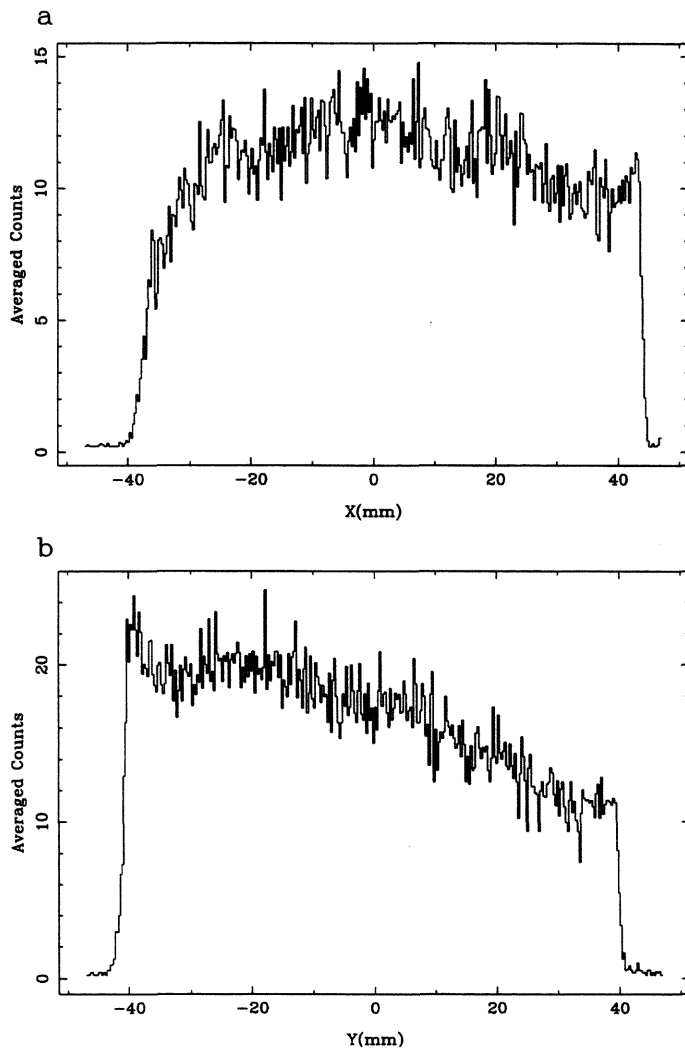
Figure 4.4: (a) horizontal and (b) vertical sections through an image resulting from illumination of the LAD with 0.28keV X-rays.

4.6 Plate with L:D=320:1

A third plate was supplied by Philips. It had the same dimensions as the previous pair except that it was 4mm thick, implying a an $L:D$ ratio of 320:1. According to the analysis of Wilkins et al. (1989) a circular pore MCP exhibits the greatest collecting area when $D/L = \theta_{crit}$ - the critical grazing angle. Therefore a plate with $L:D$=320:1, made of perfectly smooth, unreduced, Philips glass (section 4.2) is optimised for X-rays of 11.3keV. This plate was illuminated with X-rays of five different energies: C K (0.28keV), Si K (1.74keV), Mo L (2.29keV), Cu K (8.05keV) and Mo K (17.4keV). Section 4.3 above, describes slight modifications to the Kevex source configuration which were made for the slumped-plate work. This plate was tested only in beam expander mode. Images recorded with the five different X-ray energies are shown in figures 4.5 and 4.6(a).

4.6.1 Low energy results

The lower energy (0.28-2.29keV) images consist of alternating bright and dark rings. These are caused by rays entering the plate at different radial distances from the centre being reflected either into the parallel beam or away from it into the expanding diffuse cone. The $L:D$ ratio of the plate is so large that as we consider rays entering at increasing distances from the plate centre, the first rays pass straight through the plate, then, further out, they are reflected into the beam, then they are doubly reflected into the diffuse component, then triply into the beam and so on, as described in the one dimensional model of section 2.7.3.

The rings would, of course, be perfectly circular in the case of an ideal plate. Even at the lowest energy we can see that the rings are somewhat distorted. This is an indication of imperfect alignment of the channels within the optic. The misalignment is almost certainly a product of the slumping process as the thin (80:1) plate G12-46/DT/0/SA#2, made from the same standard channel plate stock, exhibited an almost perfectly circular ring structure. The task of slumping a thick plate must be inherently more difficult than that of slumping a thin one if only due to the difficulty in elastically deforming such a rigid piece of glass. It should be noted that the images from Slump 1-b exhibit a similar level of deviation from circular symmetry to that seen in the images from the thin plate G12-46/DT/0/SA#1. By altering the slumping process slightly the
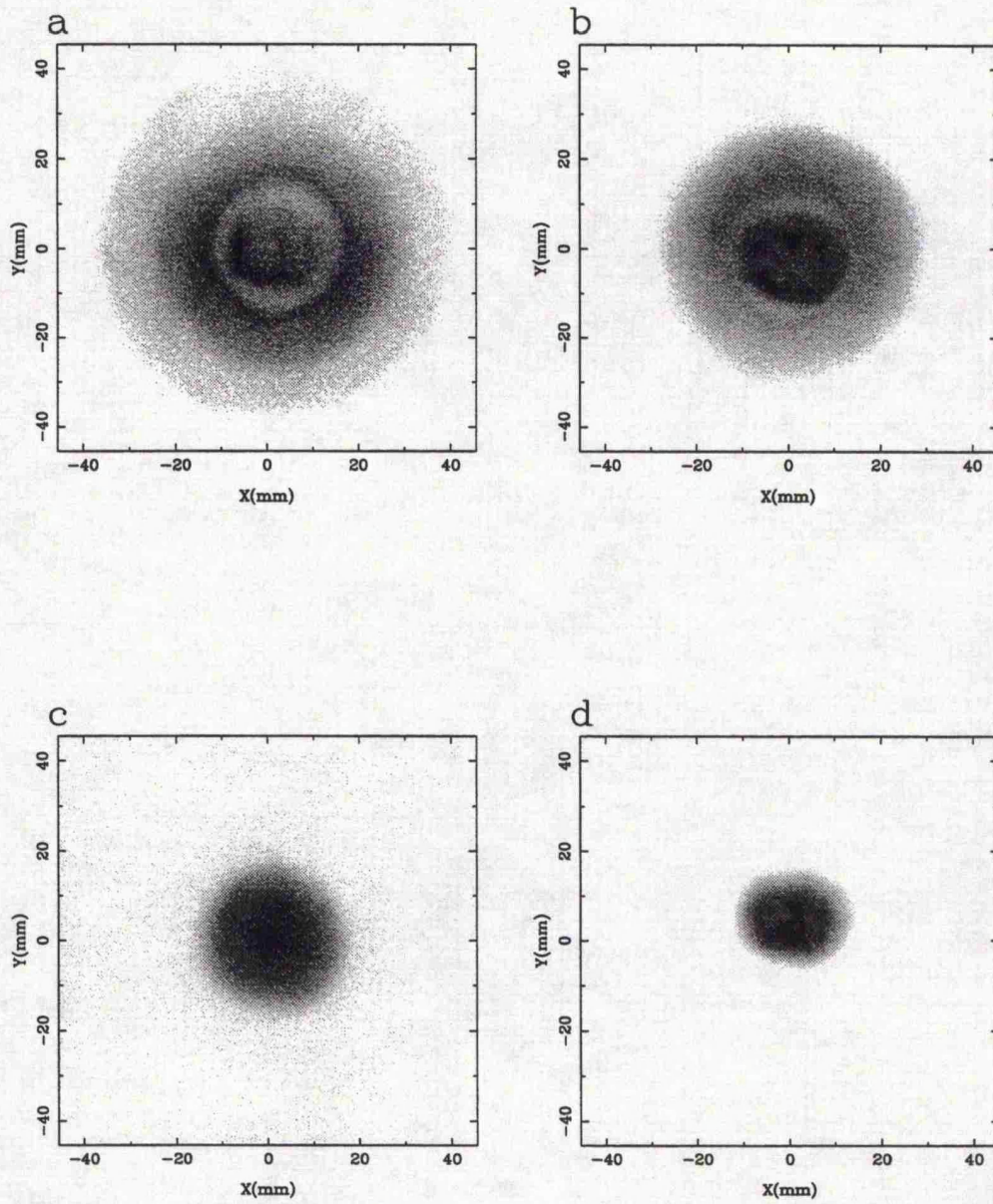
Figure 4.5: Images from the Slump 1-b 320:1 MCP acting as a beam expander at various energies: (a) C K (0.28keV); (b) Mo L (2.29keV); (c) Cu K (8.05keV) and (d) Mo K (17.4keV).
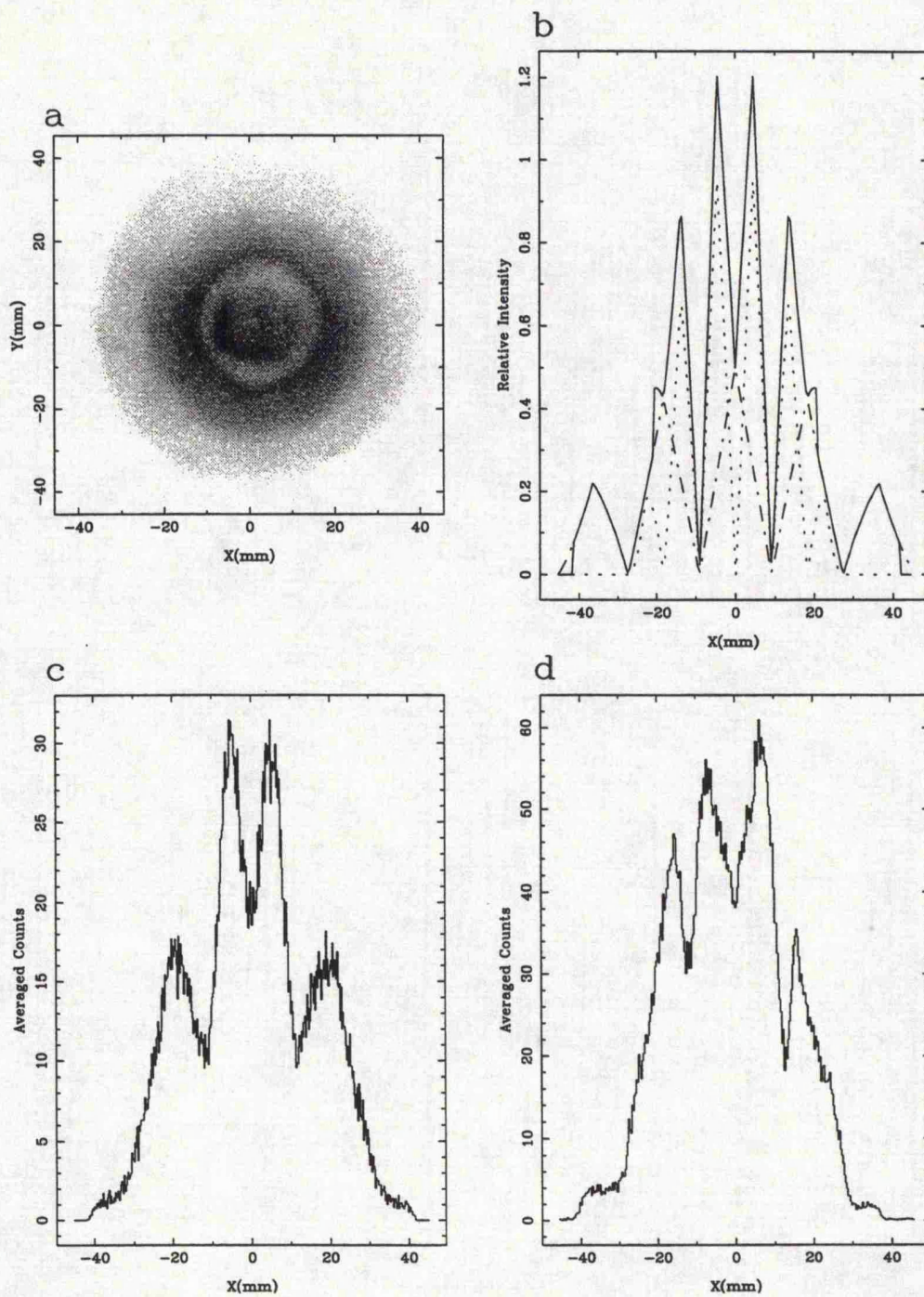
Figure 4.6: (a) image from the Slump 1-b 320:1 MCP acting as a beam expander for Si K (1.74keV) X-rays; (b) Predictions of the one dimensional analytical model, where the dotted and dashed lines represent the parallel and diffuse components respectively; (c) A Monte Carlo simulation of Slump 1-b illuminated with 1.74keV X-rays and (d) a section through the X-ray image (a).

improvements between G12-46/DT/0/SA#1 and #2 were made. It may well be that a similar improvement could be made with the thick plates by a further modification of the process. In any case, the 1.4m radius of curvature here is much more extreme than the $\geq$5m which would be required for a hard X-ray telescope. In figure 4.6(b) we see an application of the one dimensional analytical model to a 320:1 MCP illuminated with 1.74keV X-rays. Figures 4.6(c) and (d) show sections through a Monte Carlo simulation and an actual X-ray image of 1.74keV X-rays illuminating Slump 1-b. The Monte Carlo results show reasonable agreement with the experimental data, although the X-ray image is seen to be quite distorted when compared with the ideal represented by the ray-traced one. The main structures (*ie* the double bright ring) are present in both the Monte Carlo and the X-ray images, this confirms at least that the plate is working as one would expect it to. Part of the distortion will be due to the varying response of the detector MCP, an overall slant across the cut is clearly visible. Another cause must be misalignments of the channels from the ideal radial geometry.

## 4.6.2 Break-down of the analytical model

The one dimensional analytical model represented by figure 4.6(b) does not agree so well with the experimental results, despite its good agreement when applied to the 80:1 plate. In a real optic, the rays are "non-meridional". In addition to being reflected from one side of the channel to the other, in order to make the major redirections described by the 1-d model, some reflections will be such that the reflection point moves round the channel by only a small angle from reflection to reflection. These small angle reflections slightly affect the output direction of the ray causing blurring of the image. More importantly several of them may occur as the ray passes along the channel, resulting in rays being subjected to many more reflections than the 1-d model would suggest. As reported by Fraser (1982) the grazing incidence angle is the same in each of these successive reflections. In the soft X-ray spectral region the reflectivity *vs* grazing angle curve is not a step function (figure 2.1) and at most of the grazing angles experienced whilst passing through the channel plate a photon has a finite probability of being absorbed. Therefore the more times a photon is reflected the more likely it is to be absorbed. The probability of absorption, $P(A) = R^n$ where R is the reflectivity of the glass at the (constant) grazing angle for a particular ray and n is the number of reflections. Considering this, it is easy to see that the 1-d model will fall down when the number of reflections becomes large, due to long channels, as
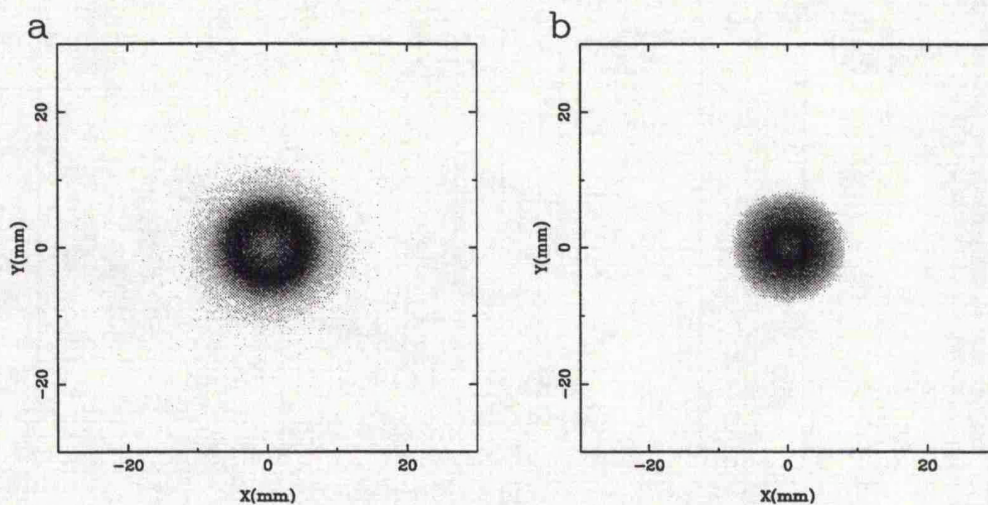
Figure 4.7: Monte Carlo simulations of an ideal plate with the dimensions of Slump 1-b illuminated by a point source of (a) 8.05keV and (b) 17.4keV X-rays.

its underestimate of the reflection count will become more significant.

The failure to account for blurring and loss of large grazing angle rays *ie* rays falling near the edges of the output distribution results in the difference between the real and Monte Carlo results and the 1-d model. The 1-d model still provides a valuable qualitative picture of the MCP beam expander, even with these long channels.

4.6.3   High energy results

The high energy (8.05keV and 17.4keV) X-ray images shown in figure 4.5 both look rather devoid of any structure. This is not what we would expect from an ideal MCP, figure 4.7 shows images obtained by Monte Carlo simulation of an ideal MCP with the dimensions of Slump 1-b illuminated with X-rays of these energies, emanating from a point source. These show a single reflected ring. The reason for this is that at the radial distances from the plate centre required to give the second ring the grazing angles are too large for there to be any reflection with these photon energies. Hence, the aperture of the MCP optic is effectively reduced at high energies, this is a well known phenomenon for all grazing incidence optics.

The structure is missing from the Cu K image because of the very large (5.5mm diameter)
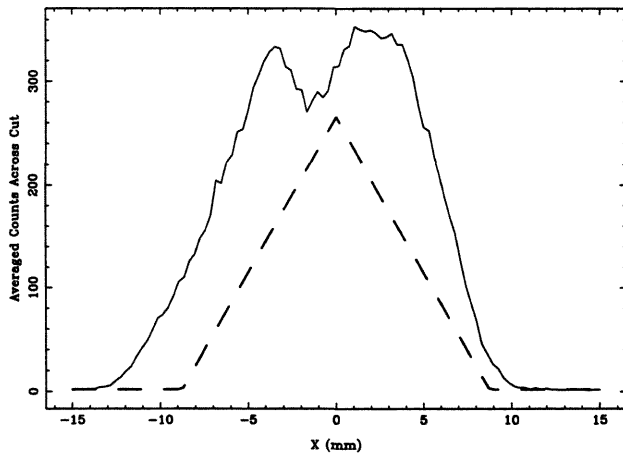
Figure 4.8: The solid line is a section through the 17.4keV X-ray image of the output beam from slump 1-b (figure 4.5d). The dashed line represents the straight through component predicted by the 1-D analytical model.

source spot with the Kevex tube in the secondary target configuration. The blurring introduced by this source size is sufficient to swamp any other effects. The Mo K image shows some ring-like structure though it is certainly not circular. The reasons for this must be firstly the highly elliptical source spot; secondly the channel misalignment, which mars even the low energy images and thirdly the effect of scattering from surface roughness (section 5.4.4). Figure 4.8 shows a cut across the Mo K image, figure 4.5(d) and also the triangular profile of the component which would pass straight through the plate, as predicted by the 1-D analytical model. The image is considerably broader than this straight-through component. One might suppose that this is due to X-rays penetrating the channel plate glass; it can be shown that this is not so. Calculation of the 1/e absorption length for Philips lead glass ($Si_5O_{12}KNaPb$; $\rho = 3.3gcm^{-3}$) yields a figure of $\mu = 144.38cm^{-1}$ (Cromer & Liberman 1970; Henke 1981). Due to the grazing incidence of the X-rays on the channel walls, rays passing through the plate by transmission must pass through a thickness of glass given by:

$$t = \frac{ns}{sin\theta} \approx \frac{ns}{\theta} \qquad (4.2)$$

where s is the septal glass thickness, θ is the grazing angle and n is the number of channel walls

the ray penetrates. The small angle approximation $sin\theta \approx \theta$ is valid for the range of angles encountered in this geometry. This approximation, applied to equation 2.29 gives:

$$\theta = \frac{y}{2R} \tag{4.3}$$

The number of channel walls, n, that the ray must pass through is obtained by dividing the grazing angle θ by the transparency angle D/L and, strictly, truncating the result to its integer part. To an accuracy of ± 1 channel, however:

$$n = \frac{\theta L}{D} \tag{4.4}$$

Combining equations 4.2, 4.3 and 4.4 we find:

$$t \approx \frac{Ls}{D} \tag{4.5}$$

The length t is more or less independent of the off-axis distance y. As y increases the distance travelled through each channel wall decreases but the number of walls the ray passes through increases commensurately. In the case of this plate $s = (p - D)/2 = 1.25\mu m$ at least, therefore $t \geq 400\mu m$ and the transmission $T = e^{-\mu t} \leq 0.3\%$. This indicates that the broadening is indeed due to reflection of X-rays in the channels. One of the problems with these images is that although the channel $L{:}D$ ratio is of the correct order for X-rays of these energies, the slump radius is very small. This means that reasonable grazing angles, resulting in reflection are only available in the channels very close to the centre of the plate. For a viable hard X-ray telescope a focal length of around 10m would have to be used.

Chapter 5

Focusing X-rays emitted by a laser-plasma source

5.1 Intro   duction

This chapter is an account of the illumination of MCP optics by the picosecond-pulsed laser-plasma X-ray source of the Central Laser Facility (CLF) at the Rutherford Appleton Laboratory. The work had two main purposes. One was characterisation of the MCPs themselves and development of characterisation techniques using the intense, 10μm diameter point source provided by the laser-induced plasma. Measurements of focusing efficiency and intensity gain were made for the Galileo square pore plate GEO4; some measurements of scattering due to surface roughness were made with the same plate. One image was also obtained using a slumped circular pore plate from Philips.

The second objective of the campaign was to investigate the viability of an "X-ray beam-line" providing strong, focused X-ray illumination at some distance from the primary source. For many applications (*eg* microscopy Stead *et al.* 1993 or lithography Turcu *et al.* 1994b) it is desirable to remove the object onto which the X-rays are directed, to some distance from the plasma as a certain amount of flying debris is generated by ablation of the target. This debris can damage delicate objects positioned nearby. The idea is particularly topical as the combination of

a laser-plasma source and an MCP optic is a strong candidate technology to provide a laboratory-based, relatively inexpensive source of illumination for X-ray lithography of the next generation of integrated circuits, obviating the need for a synchrotron source (Turcu *et al.* 1994b; Turcu *et al.* 1994a).

5.2   The RAL repetitive laser-plasma X-ray source

The principle on which the laser plasma X-ray source operates is that if an intense laser beam is focused onto a suitable target, the target will be vaporised and heated to the extent that it forms an X-ray emitting plasma. The source used in this experiment (Turcu *et al.* 1994b) is a "repetitive" one. The laser can be fired at the target with a high repetition rate (up to 100Hz). A metal or plastic tape is used as a target because the region irradiated by the laser is vaporised by each shot and a method of rapid replacement is required. The tape is wound continuously between two spools with the laser shooting at a position between the two. In this way the laser is supplied with a fresh target for each shot. By employing target tapes of different materials, plasmas can be generated with temperatures of the order of 1keV, which emit X-ray lines with particular wavelengths. For this work aluminium and Mylar[1] tapes were used to generate lines with photon energies of 1.59keV (an Al XII helium-like line) and 0.37keV (the C VI Lyman α line) respectively. The laser is large and complex and occupies most of the room which houses the source. The ultra-violet (248nm wavelength) beam from its final 40W KrF excimer amplifier enters the X-ray source chamber through a window. Each laser "shot" is, in fact, two trains of four 7ps pulses. Each train is focused by a lens onto a near diffraction limited 10μm diameter spot. The two spots are 20μm apart, resulting in X-ray emission from two plasmas about 15μm in diameter. If a very small source size is important, one of the pulse trains can be blocked, resulting in a single plasma albeit generating only half the X-ray flux. The source can generate 200mW (0.65mJ/sr/shot) of 0.37keV $C_{Ly-\alpha}$ X-rays or 10mW (0.03mJ/sr/shot) of Al_{He_α} X-rays. The flux follows a $\cos\theta$ distribution centred on the "target normal"; over the range of angles that the MCP subtends in these experiments the illumination is very uniform.

Figure 5.1 shows a spectrum for the source with aluminium target tape as used for the bulk of

---

[1] Mylar: the polyester $C_{10}H_8O_4$
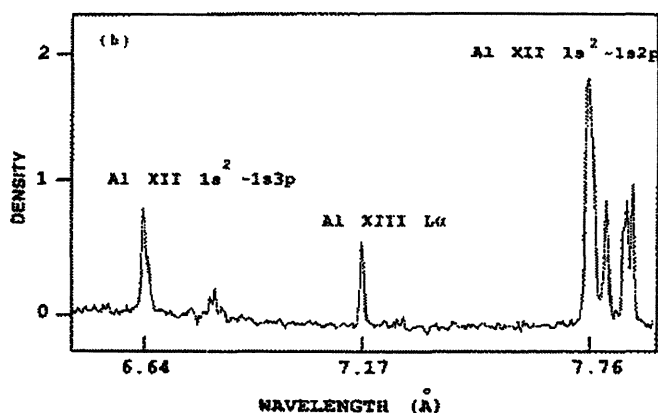
Figure 5.1: A spectrum for the repetitive laser plasma source when shooting aluminium tape, reproduced from (Turcu, Ross & Tallents 1993).

the work described in this chapter. Unfortunately no spectrum is available for the Mylar target but the $C_{Ly-\alpha}$ line is known to be dominant when filtered with nitrogen gas (section 5.3).

This type of source is rather different to the one used by Chapman, Nugent & Wilkins (1993b) in their MCP optics study. Here a single pulse from a large Nd:glass infra-red laser generates a comparatively large plasma (10J of $1.05\mu m$ radiation is deposited into a $100\mu m$ diameter circle) albeit with a similar temperature to the RAL source plasma. The X-ray flux generated per shot is very large in the Australian National University source but there is a considerable delay between shots while capacitors charge, in contrast with the 100Hz repetition rate of the RAL system.

In the RAL system the target is located at the centre of a cylindrical, aluminium chamber which is 0.5m in diameter (figure 5.2). The tank can be pumped down to a rough vacuum ($\sim 10^{-3}$mbar) or filled with gas (eg nitrogen or helium) at up to atmospheric pressure to contain the debris from the source and to act as a filter in order to isolate a spectral line. Pressure in the tank is monitored using a Pirani gauge. Objects to be irradiated with X-rays, in this case MCP optics, may be placed within the tank or in a 70mm inside-diameter tube which is attached to a flange on the main chamber. The axis of the tube corresponds to the target normal. Tubes

103
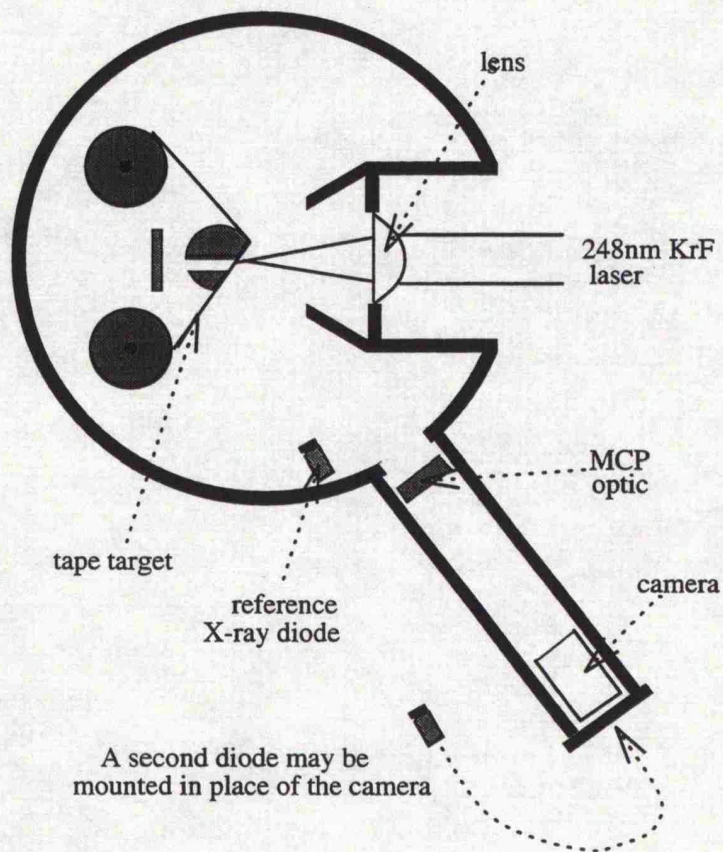
Figure 5.2: The vacuum system containing the laser plasma source with a pipe attached containing an MCP optic and camera.

104

of various lengths are available so almost any desired l_s and l_i distances were attainable. In keeping with the account of the work done at Leicester, described elsewhere in this thesis, the target normal will be referred to as the z-axis and the horizontal and vertical directions will be the known as x and y respectively.

5.3   The experimental set-up

To standardise the geometry between the two X-ray energies, l_s and hence l_i were chosen so that the maximum grazing angle of X-ray incidence on the channel walls was equal to the critical angle or angle which gave 50% reflectivity. This maximum angle is equal to half the angle subtended at the source by the MCP. In the 1.59keV experiments, the required source-MCP and MCP-detector distances were $l_s = l_i = 644$mm so a 1m pipe had to be fitted to the chamber and the MCP had to be positioned within it. A means of holding the MCP at various positions along the pipe was needed. For illumination with 0.37keV X-rays the l_s and l_i values which meet the above criterion are only 197mm so the MCP had to be located within the tank and a means of holding it in this situation was also required. As film was used to record the focused images some kind of camera was necessary. Fortunately at both wavelengths the desired image plane lay outside the tank, so that in both cases the camera would have to be in the extension pipe *ie* only one type of camera was required. The 1.59keV work was carried out in helium at a pressure of 1bar. This gas served to contain the debris from the source yet is essentially transparent to 1.59keV X-rays. A gas transmission *vs* X-ray energy curve is shown in figure 5.6(c). The 0.37keV experiments were performed in a nitrogen atmosphere at a pressure of 3mbar which was maintained by continuously pumping the chamber while leaking nitrogen into it and monitoring the pressure on a Pirani gauge (see figure 5.7(a) for the transmission curve of this gas). The reasons for using a nitrogen atmosphere are to monochromatise the X-rays, and by absorption reduce the intensity falling on the diodes whose response to excessive X-ray flux is non-linear.

Since the MCP tilt could not be adjusted without opening the tank (section 5.3.2), it was desirable to be able to align the channel plate to a good degree of accuracy before sealing it in the first place. A useful technique for achieving this was developed during the experimental

campaign. The RAL source has a 300mW HeNe laser (red light) coaligned with the excimer, and focused onto the same point on the target as the excimer. If the target tape is replaced with a strip of white paper, the HeNe laser light scattered from it is sufficiently strong that when focused by the MCP onto a piece of tracing paper at the end of the extension pipe, the characteristic cruxiform image is plainly visible with the room lights dimmed. The positioning and sharpness of this image could be adjusted by tilting the MCP in its holder (section 5.3.2) or by moving it up or down the pipe. The optimum position for the visible image, of course, corresponds to the optimum position for its X-ray counterpart, hence accurate alignment is possible prior to sealing up the chamber.

5.3.1 The MCPs

The great majority of the results obtained at RAL were from a Galileo square pore MCP known as GEO4. Some laboratory work with this plate is reported in chapter 3. To recapitulate, its physical dimensions are as follows: channel length or thickness L=4.8mm; square channel side length D=85μm; channel pitch p=122μm and plate diameter=33mm. The $L{:}D$ ratio is 56:1. The plate has been hydrogen fired and has a bias angle of 8°. One image was recorded using a Philips slumped circular pore plate denoted Slump 1-b. An account of experimental work with this plate, performed at Leicester, is given in chapter 4. The physical characteristics of this MCP are: channel length or thickness L=4.0mm; square channel side length D=12.5μm; channel pitch p=15μm; radius of curvature R_{slump}=1.4m and plate diameter=46mm, so the $L{:}D$ ratio is 320:1. The plate is "etched-only" *ie* it has not been hydrogen reduced.

5.3.2 The MCP holder

The solution to the problem of holding the MCP within the tank was straightforward: a standard optical mount was used, allowing tilts to the xz and yz planes by means of screw adjustments. The only modification that had to be made was to manufacture nylon spacers which would enable the 50mm diameter mount to hold the 33-46mm diameter MCPs.

The problem of holding the MCP in the pipe was rather more troublesome. A special device, which became known as the "bullet", was manufactured in the Leicester workshop (figure 5.3).
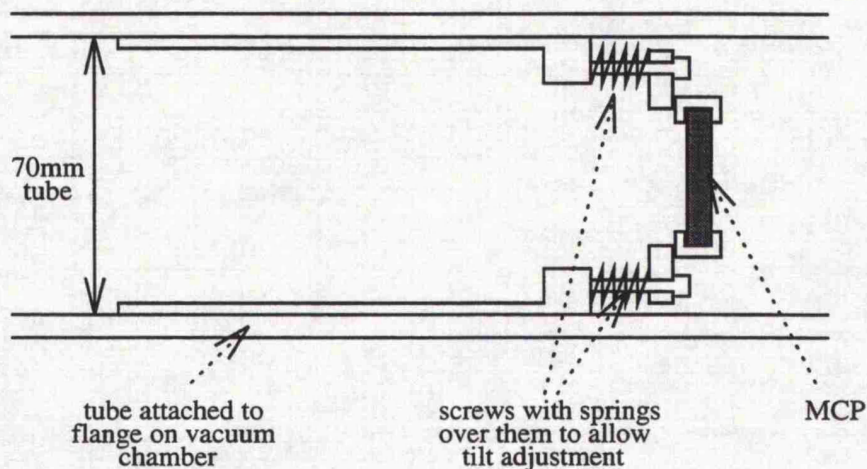
Figure 5.3: The "bullet" device used to hold the MCP within the 70mm inside-diameter tube on the RAL chamber.

It fits inside the 70mm pipe with just enough clearance to allow it to slide up and down It firmly holds an MCP in such a way that tilts to the xz and yz planes of up to 8° (necessary because of the bias angle on the Galileo square-pore plate) can be made by adjusting the three screws on the front.

5.3.3 The camera

Two cameras were constructed from aluminium film tins (figure 5.4). The tins were cylinders of 60mm diameter with screw tops. The ends of the tins were cut off and replaced with windows made of 1μm polypropylene with 0.1μm aluminium deposited on each side (figure 5.6(a) gives the X-ray transmission of this combination). The windows were supported by 100μm wires spaced 1cm apart. The purpose of the window was to block stray visible light, present when the camera was being mounted in the pipe (despite turning off the room lights) and also to filter out intense visible and ultra-violet light emitted from the plasma during exposure. Pumping holes were bored in the sides of the cans so that they would be evacuated when the chamber was pumped down, and filled with whatever ambient gas was used. The holes had to be loosely covered with black tape to avoid light shining through them onto the film (figure 5.4). Loading of the cameras was performed in the CLF dark-room: a circular piece of film was first cut from a large sheet and placed in the lid of the can. A rubber O-ring, whose external diameter was
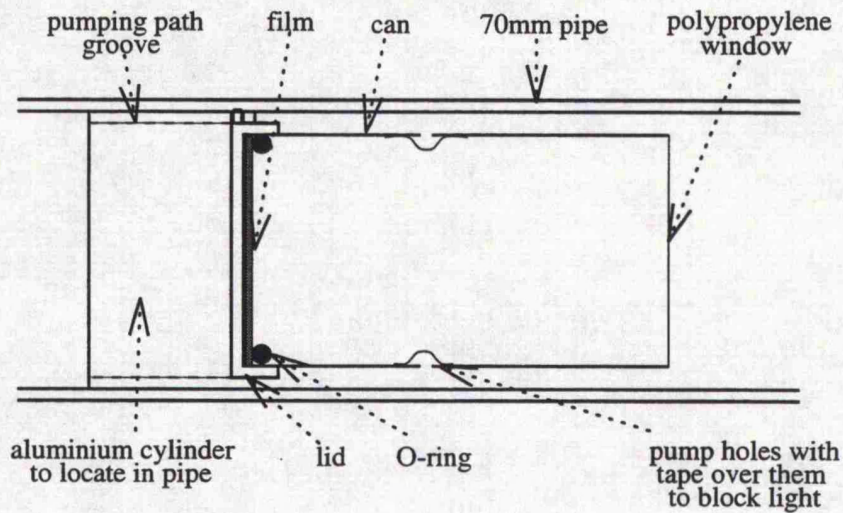
Figure 5.4: The camera used in the RAL experiment.

such that it fitted tightly in in the lid, was then placed on top of it so that it could not move. The lid was fitted to the camera and black tape was wound around the join to prevent light leakage. The assembled camera was fitted to a 70mm aluminium cylinder to ensure a good fit in the pipe. The cylinder had grooves cut in it to allow gas to be pumped past it and as a further precaution a tube was always used to connect the volume behind the camera to the main tank, in order to equalise pressures on both sides.

5.3.4 The X-ray film

Kodak direct exposure film (DEF) was used to record the 1.59keV images. The response of this film is well known, Rockett *et al.* (1985) and Henke *et al.* (1986) having investigated it in some detail. Optical density (OD) is the standard measure of opacity, measured using a microdensitometer (section 5.3.5). Obviously the greater the X-ray exposure to which a film is subjected, the higher the OD recorded on it after development will be. The above authors report that the OD increase with exposure is not linear and, furthermore, is wavelength dependent. They also, rather helpfully, provide us with calibration graphs for the 1.49keV neutral Al K line which are reproduced here as figure 5.5. Rockett *et al.* (1985) also present a calibration graph for the 1.74keV Si K line. This graph lies virtually on top of the 1.49keV plot, indicating
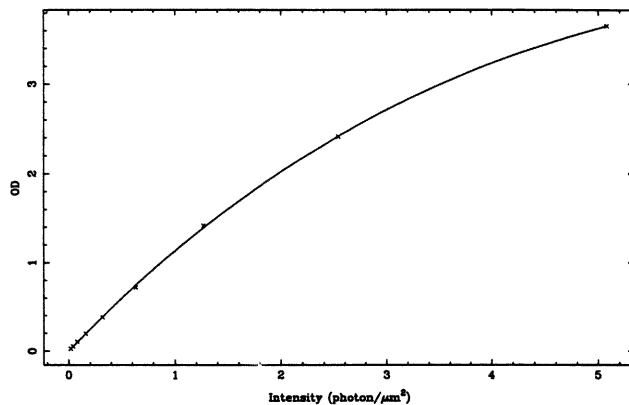
Figure 5.5: A calibration graph for Kodak DEF X-ray film, from data points measured with a diffuse microdensitometer by Rockett *et al.* (1985). The cross calibration to specular density with a numerical aperture of 0.25, as measured at Leicester, is due to Henke *et al.* (1986).

a small variation of response with energy in this region. Unfortunately the Al emission line complex produced by the laser, and in particular the bright $1s^2$-$1s2p$ line of Al XII at 1.598keV, straddles the Br L_{II} absorption edge at 1.596keV, introducing a significant, still unquantifiable uncertainty to the calibration. Nevertheless the 1.49keV calibration graph has been used to reduce the 1.59keV data.

DEF has emulsions on both sides and a supercoat which protects the emulsion. It can be exposed to a red safe-light without risk of fogging. These characteristics make its use straightforward although the supercoat precludes its use for X-ray energies below 1keV due to absorption of the radiation before it reaches the emulsion. The developing procedure used for DEF, at 20°C, was:

1. 4-5 minutes in Kodak D19 developer

2. 30 seconds in stop bath

3. 8 minutes in FX40 fixer

4. 20 minutes wash in running water

5. 30 seconds in Ilford wetting agent

109

Because of the 1keV cut-off DEF could not be used to image $C_{Ly-\alpha}$ X-rays. For these a medium known in RAL parlance as "Chinese film" (formally, Shanghai 5F no-supercoat XUV film) was used. A limited calibration of this film is provided by Lu *et al.* (1992). Only one image was recorded on this type of film and it was badly overexposed; due to time pressure the image could not be repeated. Owing to the lack of any correctly exposed images an exact knowledge of the properties of Chinese film was not required for this work and no calibration is presented here.

Chinese film has emulsion on one side only and has no supercoat. It is fogged by "safe"-lights so it has to be loaded and unloaded in complete darkness. These drawbacks are compounded by the long periods of time it has to spend in the chemicals during development, which was performed at 20°C as described below:

1. 30 seconds in distilled water

2. 20 minutes in Kodak D19 developer

3. 2 minutes in Amfix fixer

4. 20 minutes wash in running water

5.3.5 The microdensitometer

The microdensitometer used to determine the OD of the images recorded on film at the CLF (*eg* figure 5.8) was a Joyce Loebl [2] Mk3c with a ×10 magnification objective lens of numerical aperture 0.25. It belongs to the Astronomy group at Leicester. This device scans across an exposed film image and plots OD as a function of position. The OD is averaged over a slit, the height and width of which can be set by the operator. For the measurements reported here the slit height was set to 2mm and the width was 0.3mm, apart from when measuring the "scattering" images (figures 5.12 and 5.13). In this case the slit size was reduced to 1mm high × 0.2mm wide. These dimensions were reduced by a factor of twenty at the film by the optics of the device so the areas being sampled were less than the area of one microchannel aperture of the GEO4 optic.

---

[2] J.L. Automation, Unit 2c Hylton Business Park, Sunderland. SR5 3NR

5.3.6 The X-ray diodes

In this work a matched pair of Si(Li) PIN X-ray diodes from Quantrad [3] was used (Fraser 1989; Bar-Lev 1984). They had an area of 1cm^2 and an active depth of 125μm, the "window" (n-doped layer which X-rays must penetrate to enter the active (intrinsic) region) was 0.25μm thick. This layer causes significant attenuation of 0.37keV X-rays, although it is almost perfectly transparent when the photon energy is increased to 1.59keV (figure 5.6 b). One diode, with a 5mm diameter circular aperture, is permanently mounted within the tank at a distance of 17cm from the source and at an angle of 26° to the target normal. It was used throughout the experiment as a flux-monitor; this was necessary as the flux per shot varies quite considerably (by a factor of about 2) from shot to shot. The second diode was mounted on a special flange which fits onto the end of the 70mm pipe, or directly onto the side of the tank in place of the pipe. The flux concentration due to the MCP was measured using this second diode with both a 5mm and a 2mm diameter circular aperture. Absolute measurements of focusing efficiency cannot, at present, be made in the laboratory at Leicester. Fluxes incident on the diodes are recorded in terms of charge collected from the diode (of the order of nC). The charge is directly proportional to the number of photons falling on the diode which, due to the short plasma lifetime, integrates over each laser shot. The charge collected can be converted to the number of photons incident on the diode. In silicon one electron is liberated for every 3.65eV of X-ray energy deposited. The absorbing 0.25μm layer at the front of the diode must also be taken into account.

For the 1.59keV work 12.5μm beryllium windows were fitted to the front of the diodes (see figure 5.6(a) for the X-ray transmissions of these) while for the 0.37keV experiments 0.5μm vanadium filters supported by a mesh of 24μm nickel wires with a 90% open area were used (a transmission curve is shown in figure 5.7(b)).

5.3.7 Transmission curves

Various combinations of filters and ambient gases were used to energy-select the radiation and contain flying debris ablated from the source. In order to understand the effect of these filter/gas systems, transmission versus X-ray photon energy curves have been plotted for all of them

---

[3] Type 100-PIN-125: Quantrad Corporation, Torrance ,CA 90502, USA.

individually and also for the combinations that were used during the experiment. These plots are presented in figures 5.6 and 5.7.

5.4 Results

5.4.1 X-ray Diodes

Measurements of the flux concentrating effect of the MCP GEO4 were made by comparing the signal from a diode placed at the focus of the MCP with the signal from the diode in the same place but without the MCP present. The reference diode signals were used for normalisation ie elimination of the shot-to-shot variation of the source strength. Measurements were made for both 1.59keV and 0.37keV X-ray energies. The concentration factor F is defined as:

$$F = \frac{\Phi_{det}^{mcp}}{\Phi_{det}^{no\ mcp}} = \frac{(Q_{det}^{mcp}/Q_{ref}^{mcp})}{(Q_{det}^{no\ mcp}/Q_{ref}^{no\ mcp})} \tag{5.1}$$

where Φ_{det}^{mcp} and $\Phi_{det}^{no\ mcp}$ are the X-ray fluxes incident on the PIN diode detector with and without the focusing MCP present; Q_{det}^{mcp}, Q_{ref}^{mcp}, $Q_{det}^{no\ mcp}$ and $Q_{ref}^{no\ mcp}$ are the average charges recorded per shot, with and without the MCP present, by the detector and reference diodes. Another quantity, the focusing efficiency, may be defined:

$$E = \frac{\Phi_{det}^{mcp}}{\Phi_{mcp}} \tag{5.2}$$

where Φ_{mcp} is the flux falling on the MCP. As

$$\Phi_{det}^{no\ mcp} = \frac{\Phi_{mcp}\Omega_{det}}{\Omega_{mcp}} \tag{5.3}$$

where Ω_{det} and Ω_{mcp} are the solid angles subtended at the source by the detector diode and the focusing MCP, we can write

$$E = F\frac{\Omega_{det}}{\Omega_{mcp}}. \tag{5.4}$$

Table 5.1 shows the concentration factors and efficiencies for the two X-ray energies and, in the 1.59keV case, two diode apertures. Table 5.2 shows the absolute fluxes detected averaged over the entire diode aperture.

The measurements of flux concentration and hence focusing efficiency are affected by the size of the aperture in front of the detector diode as the diode sums the X-ray intensity over its
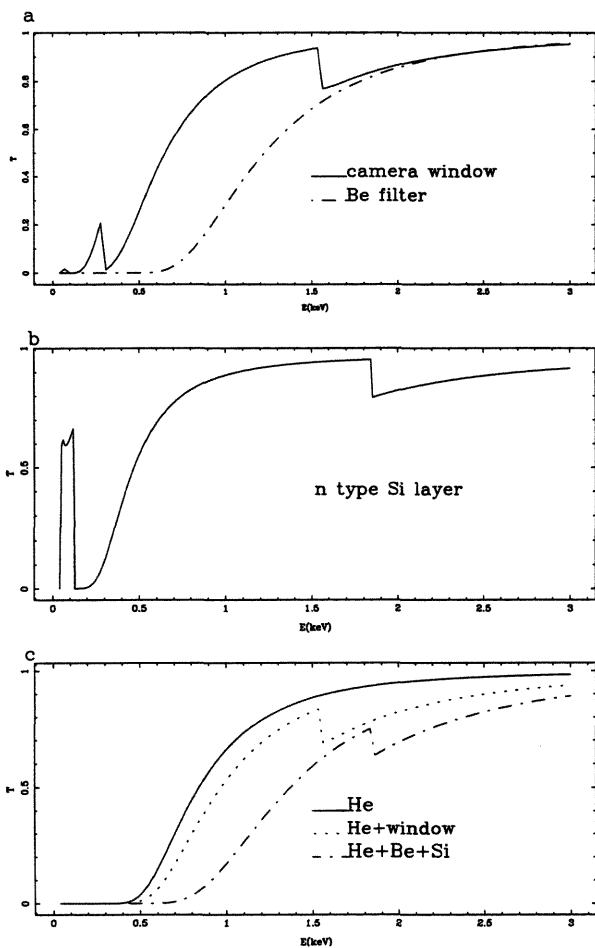
Figure 5.6: Transmission versus X-ray energy curves for: (a) The window on the front of the camera which consists of a 1μm thickness of polypropylene with 0.1μm of aluminium deposited on each side of it and the 12.5μm thick beryllium filter fitted to the front of the X-ray diodes; (b) The inactive n-type silicon layer at the front of the PIN detector diodes; (c) a 1288mm depth of helium at a pressure of one atmosphere and also compound transmissions for helium plus the camera window and helium plus the diode filter.
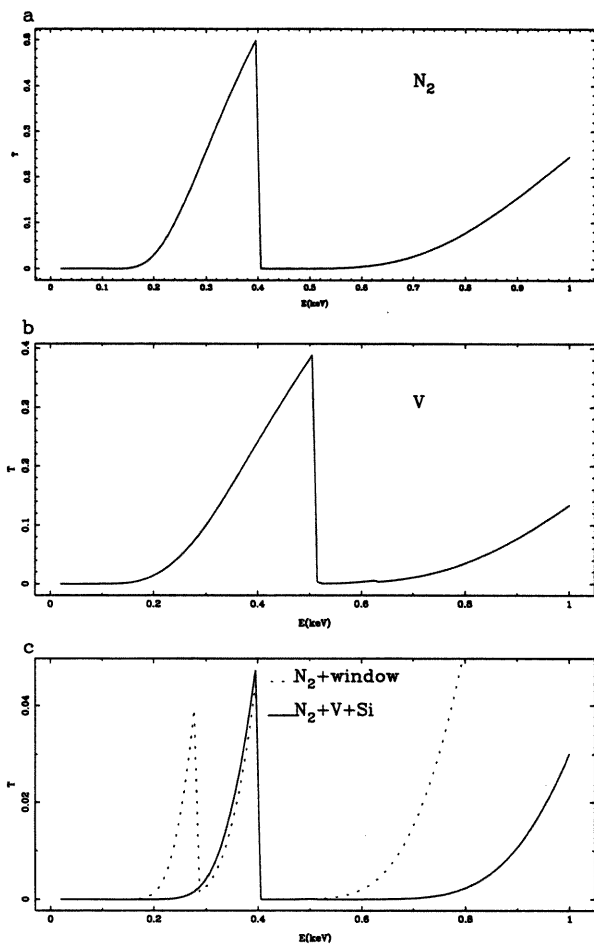
Figure 5.7: Transmission versus X-ray energy curves for: (a) a 394mm length of nitrogen at 3mbar; (b) the 0.5μm thick, 90% open-area vanadium filter, as used on the front of the X-ray diodes; (c) The combined transmissions of the N_2 with the V diode filter and with the camera window of figure 5.6(a).

Energy		1.59keV		0.37keV
Aperture		5mm	2mm	5mm
F	**expt**	**8.7**	**8.5**	**3.9**
	MC1	15.2	66	10.1
	MC2	8.9	37	7.9
	MC3	9.1	37	7.6
E	**expt**	**0.065**	**0.01**	**0.029**
	MC1	0.113	0.079	0.075
	MC2	0.066	0.045	0.058
	MC3	0.067	0.045	0.057

Table 5.1: Flux concentration factors and focusing efficiencies for the three experimental configurations. The "expt" rows indicate the experimental data while MC1-3 are Monte Carlo simulations with experimentally determined distortions (see chapter 6): MC1 is an MCP made of silica at a density of $2.15g/cm^3$ with perfectly smooth channels; MC2 is the same except that the density of the silica has been reduced to $1.4g/cm^3$; MC3 has density $2.15g/cm^3$ and an RMS surface roughness of 30Å.

Energy		1.59keV		0.37keV
Aperture		5mm	2mm	5mm
Absolute Flux	raw	2.3×10^5	2.2×10^5	2.4×10^6
(photon/shot/mm^2)	corrected	3.6×10^5	3.5×10^5	8.5×10^7

Table 5.2: Absolute fluxes, averaged over the diode aperture.

active area. It was reported in chapter 3 that the FWHM of the GEO4 focus was ~ 2mm in a geometry not very different from the one used here. This result will be confirmed for the current experiment in section 5.4.3 below. If the diode samples a small region at the peak of the focused spot (2mm aperture say) then the concentration factor will be high. If it samples a large area (5mm aperture), much of the aperture will be illuminated only by the less intense diffuse or cruxiform components, hence the concentration factor will be smaller.

In practice the concentration factors using 1.59keV X-rays with 5mm and 2mm diameter diode apertures are almost the same. One would expect the concentration factor with a 2mm aperture to be bigger than that with a 5mm aperture for the reasons outlined above. The fact that this is not the case is an indication of imperfect alignment of the focusing MCP with the diode aperture. The alignment techniques used (section 5.3 above) were sufficiently reliable that we may confidently say that the 5mm diode aperture would sample the *entire* true focus plus parts of the cruxiform and diffuse components. We cannot, however, be confident of the same thing in the case of the 2mm aperture. Iin fact the results indicate that the most intense part of the focused spot is missing the detector diode in the 2mm aperture case, therefore the apparent concentration factor is less than the true value.

Comparison of the results with 5mm apertures at the two X-ray energies shows a smaller concentration factor at 0.37keV. All the different types of distortion that an MCP can exhibit result in degradation of the focused image by introducing an angular deviation from the paths that rays would follow passing through an ideal MCP. For this reason we expect the focused spot at 1.59keV, owing to the fact that it is 644mm from the MCP, to be approximately three times broader than the spot in the 0.37keV experiment which is only 197mm (roughly 1/3 of the 1.59keV distance) from the plate. A 5mm aperture at 644mm will sample mainly the central focus (FWHM ~ 2mm or 10arcmin), plus a contribution from the line and diffuse components. A 5mm aperture at 197mm will contain the central focus (FWHM=10arcmin corresponds to 0.6mm at this distance) but also a much larger contribution from the relatively weak line and diffuse components. Hence the intensity, averaged over the aperture, will be smaller when compared to the intensity of a corresponding illumination with no MCP present, at a distance of 197mm from the plate than at a distance of 644mm. Monte Carlo simulation bears this result out to some extent: see below for a discussion of the modelling of this experiment.

Another interesting result from these diode measurements is that Monte Carlo simulations using reasonable compositions for the MCP glass: either $Si_5O_{12}KNaC$, $\rho = 3.3g/cm^3$ (Fraser 1982) or silica with $\rho = 2.2g/cm^3$ (MC1 in table 5.1) give rather better focusing efficiencies than are seen experimentally.

A 5mm diameter circle is a large area to sample compared with the FWHM of the central focus. The proportion of the total number of rays rays passing through the MCP that fall in the circle, and hence F and E are almost independent of MCP distortion. No distortion measured during the course of this work introduces a big enough deviation from the ideal ray-path to cause a ray in the true focus to fall 2.5mm from the centre of the distribution. The 5mm detector aperture also renders F and E insensitive to slight misalignments of the focusing MCP, as an uncertainty in the centre of the focal spot of about 1mm will still allow the entire true focus to fall on the detector.

These two facts indicate that the only explanation of the low F and E is that the MCP glass is not as reflective as one would expect it to be. The chemistry of the hydrogen reduction process applied to MCPs is complex, involving the formation of a lead-free, semiconducting surface layer. It could be that this reduction has some unexpected effect on the reflectivity. Alternatively the poor reflectivity could be due to surface roughness on very short length scales which causes scattering at such large angles that the scattered rays do not emerge from the channel exit (section 5.4.4).

Monte Carlo simulation with this type of surface roughness at an RMS height $\sigma = 30\text{Å}$ (tabulated as MC3) yields results which are in close agreement with the experimental data at 1.59keV as does a physically dubious simulation with a reduced density of the silica $\rho = 1.4g/cm^3$ (MC2). Unfortunately neither of these modifications lead to good agreement with the 0.37keV experimental data. The conclusion we must draw from this is that the microchannel surface is not well understood. The hydrogen reduction process, although there is tenuous evidence that it improves the surface roughness (sections 3.3.4 and 6.4.2), may in fact be reducing the overall reflectivity of the glass.

5.4.2 Depth of focus

Figure 5.8(b) was recorded with MCP GEO4 positioned to give the sharpest focus that could be obtained when illuminated by 1.59keV X-rays. In figures 5.8(a) and (c), the MCP has been moved 40mm towards and away from the source, respectively. The X-ray exposures were such that the integrated charge collected from the reference diode was 20nC in each case. The width and splitting of the line foci in these images are broadly in agreement with Monte Carlo simulations (figure 5.9). The model does not, however, predict the splitting of vertical cross arm in the out of focus images being greater at one end than the other. It is tempting to say that this is due to the plate having to be tilted because of the channel bias angle, so that one side of the plate is nearer to the correct focal position. To do so would be incorrect as there is only 4mm difference in z-position between the two extremes of the plate - an insufficient distance to cause this effect. The cause must be the internal alignment of the channels. In the modelling of channel distortion and misalignment (see chapter 6) misalignments were assumed to occur randomly and be normally distributed. It may well be that this is not the case in real MCPs. Channel long-axis misalignments may occur, as a result of some part of the manufacturing process, in such a way that their direction and extent is some slowly varying function of position on the plate. In this way channels on one side of the plate might tend to focus to a slightly different z-position compared with channels on the other side. This type of effect appears to be manifest in figure 5.8.

5.4.3 Microdensitometer scans

Microdensitometer scans were made across figure 5.8(b) and across a second image which was obtained in the same focusing geometry but with an exposure of only 2.3nC (corresponding to a single shot of the laser). These scans are shown in figure 5.10. The scans were made along each of the cross-arms and were made to pass through the region of highest density in each case. The optical densities recorded on film may be converted to X-ray intensities (in units of photons/mm^2) using the DEF calibration graph shown in figure 5.5. A third negative was also scanned, which had been exposed with the camera positioned as it was when the images described above were recorded but with no MCP present. In this case the OD recorded was a constant 1.02 with a fog level of 0.15 across the film, for an exposure of 100nC.
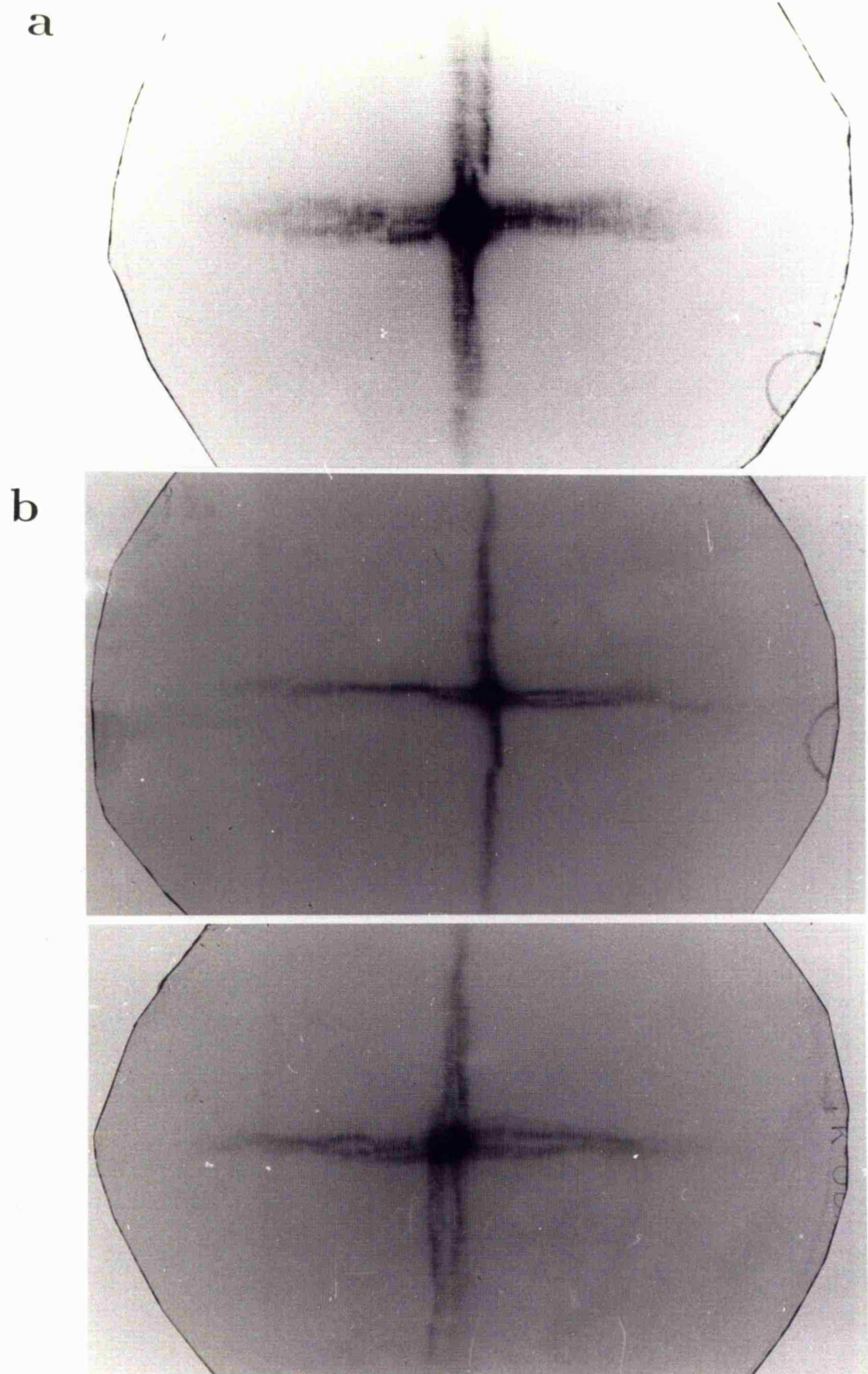
Figure 5.8: Point to point focusing of 1.59keV X-rays. In (b) l_s is as close in value to l_i as could be achieved. In (a) and (c) the MCP has been moved 40mm towards and away from the source, respectively.
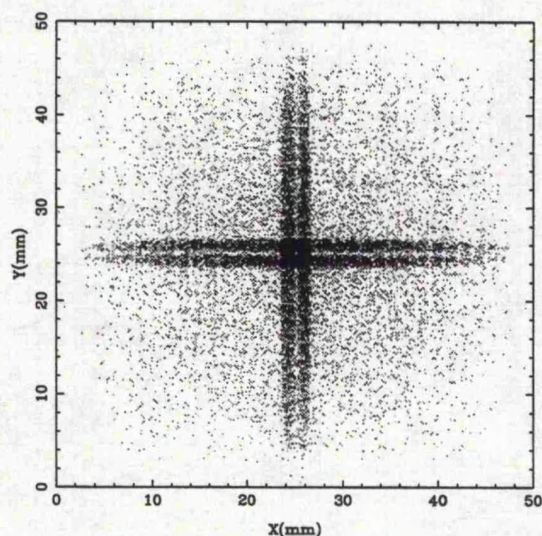
Figure 5.9: Monte Carlo simulation of an ideal MCP of the same dimensions as GEO4 focusing 1.59keV X-rays with $l_s = 604$mm and $l_i = 684$mm as they are in the X-ray image figure 5.8(a)

The intensity gain G, as defined in section 2.4.3 was measured by direct comparison of the X-ray intensities inferred from the OD at the peaks of the true foci on the films exposed through the MCP with the intensity found from the scan across the film exposed with no MCP present. Neither the 2.3nC nor 20nC exposures were ideal for this analysis: the former caused a peak OD of only 0.61 compared to the background fog level of 0.15, the latter resulted in a peak OD of 3.0. which is at the limit of the available calibration information. The results obtained from the two exposures were in reasonable agreement. The accuracy was limited in one case by the signal to noise ratio and in the other by non-linearity of the film response.

Table 5.3 shows the values for G along with the FWHM values for the peaks obtained from the scans and, for comparison, the FWHM of a focused Si K (1.74keV) X-ray spot obtained at Leicester (section 3.3.3). There is some discrepancy between the FWHM values obtained with the two different exposures and with those obtained at Leicester. The difference between the FWHM for the two exposures ties in with the difference in peak gain; note that the MCP was removed from the pipe and replaced between the times when the two images were recorded, as a result of this some alteration in the alignment may have occurred.

The FWHM values for the focused spot, confirm the assertion of section 5.4.1 that the entire

120
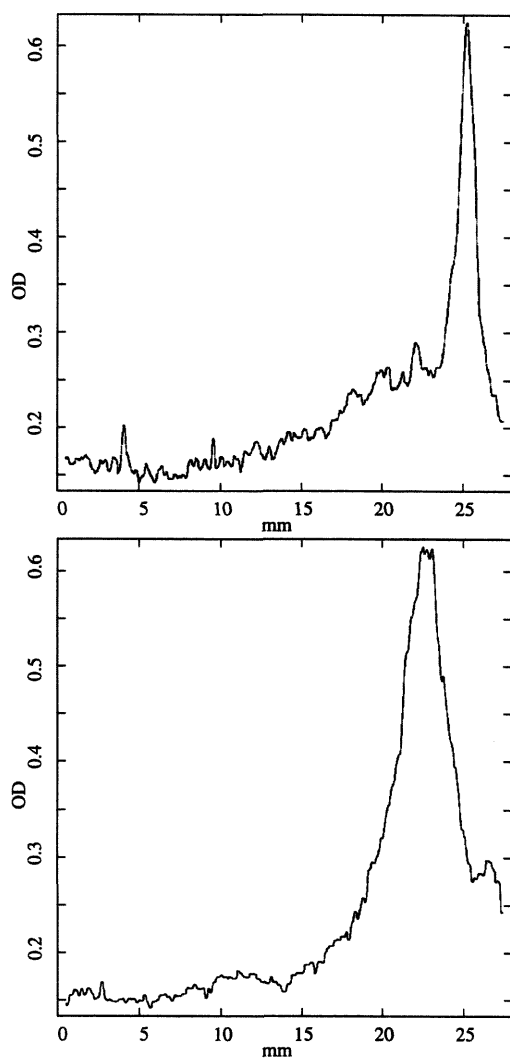
Figure 5.10: Microdensitometer scans along the cross arms of an image recorded in the same focusing geometry as 5.8(b) (point to point focusing of 1.59keV X-rays by optic GEO4) with an exposure of 2.3nC.

Exposure (nC)	Gain G	FWHM$_x$ (mm)	FWHM$_y$ (mm)
2.3	25	1.3	3.1
20	18.3	2.4	2.8
Si K (at Leicester)		1.4	2.0

Table 5.3: Gain G and FWHM from microdensitometer scans along the cross arms of focused images with FWHM measurements for focused Si K (1.74keV) X-rays obtained in the laboratory at Leicester.

true focus should fall into the 5mm circle. They also show that sampling a 2mm circle is of little value as only part of the true focus will be enclosed and the averaged intensity will be highly sensitive to slight misalignments. G is affected by both the glass reflectivity and the mechanical quality of the plate. F however, when it is measured with a 5mm diameter aperture, only depends strongly on the reflectivity of the glass. Hence they are a complementary pair of measurements which, between them, give a clear insight into the quality of the plate.

The measured intensity gain of around 20 was rather encouraging, particularly from the point of view of the X-ray beamline proposed in the introduction section of this chapter. It is roughly in agreement with the rather crudely measured value of 45 obtained in the laboratory at Leicester (Fraser *et al.* 1993b) and is of the same order as the figures of 23-31 obtained by Chapman, Nugent & Wilkins (1993b) with the ANU laser plasma source. The reader is reminded that this plate represents a first attempt at manufacture of a square pore MCP and the next generation of such plates should offer gains much closer to the figures predicted theoretically, making the beamline a very exciting prospect.

5.4.4 Surface roughness analysis by X-ray scattering

X-ray scattering is an established technique for investigating the roughness of optical surfaces (Christensen *et al.* 1993). In this type of work a small area on the optical surface is illuminated, at grazing incidence, with X-rays. The reflected rays are detected by some means and one finds that in addition to the specularly reflected rays there is another class of *scattered* rays. These rays emerge from the surface, still in the same plane as the incident rays and the normal to the surface at the interaction point, but in such a direction that the angle of reflection is not equal
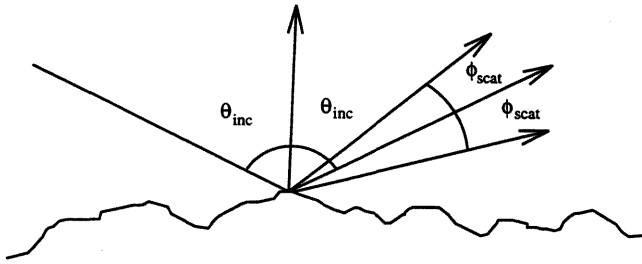
Figure 5.11: When X-rays are scattered away from the specular reflection direction by surface roughness they generally remain in the same plane as the incident beam and the normal to the surface at the point of interaction.

to the angle of incidence (figure 5.11). These X-rays have been scattered by tiny topographic features of the optic known as surface roughness. At high energies such scattering is the limiting factor in the performance of MCP optics. By illuminating the MCP in a controlled way with X-rays of a known energy we can gain an insight into the nature of its surface roughness.

Most treatments of scattering from surface roughness (*eg* Church, Jenkinson & Zavada 1979; Beckmann & Spizzichino 1963) agree that the total integrated scatter (TIS) or fraction of X-rays with wavelength λ incident at a grazing angle θ on a surface with RMS surface roughness σ which are scattered out of the specular direction is given by:

$$\frac{I_s}{I_0} = 1 - e^{-(4\pi\sigma sin\theta/\lambda)^2} \tag{5.5}$$

Using a simple model, treating the surface roughness as a sinusoidal variation in surface height with wavelength τ, the scattered angle is given by the grating equation:

$$\phi_{scat} = \frac{\lambda}{\tau sin\theta} \tag{5.6}$$

A rough surface can be treated as a sum of sinusoidal Fourier components. For a simple treatment of such a surface we set τ to be the "correlation length" of the roughness, an averaged spatial wavelength over all the components present in the surface, then ϕ_{scat} becomes an average scattering angle.

A mask was made from a 33mm diameter metal disc with a 0.5mm diameter hole drilled in

123
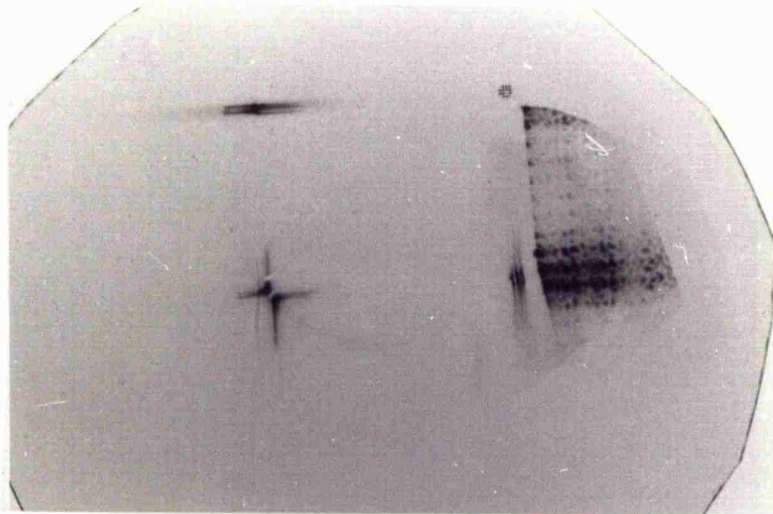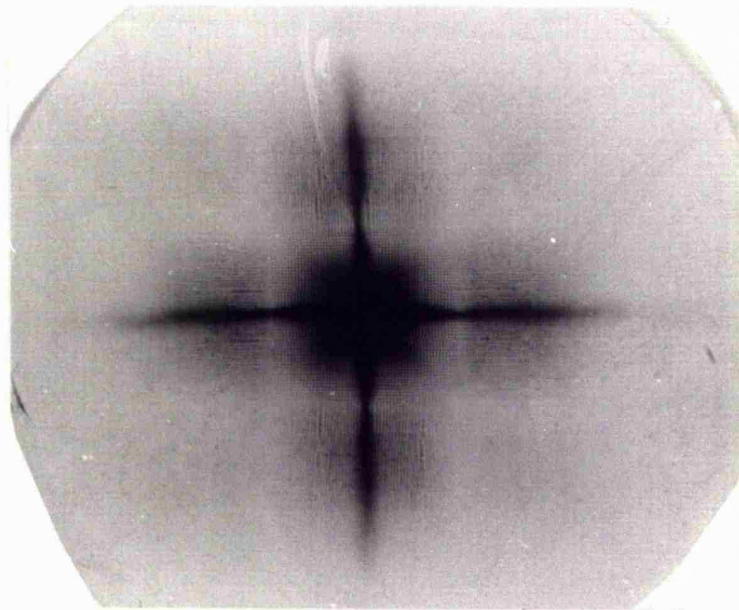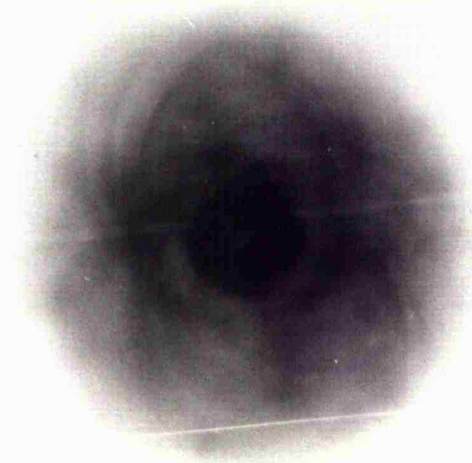
Figure 5.12: (a) Image of scattering wings caused by illumination of GEO4 through a 0.5mm pinhole with 1.59keV X-rays, (b) Image of 0.37keV X-rays focused by GEO4, (c) Image of 1.59keV X-rays focused by circular pore slumped MCP slump 1b.
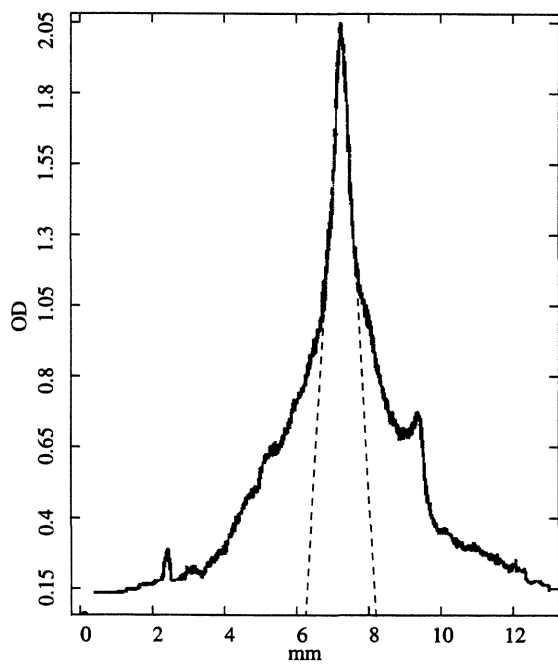
Figure 5.13: A Microdensitometer trace along "scattering wings" from which the channel surface roughness and correlation length were estimated. The dotted lines indicate the assumed width of the specular beam.

125

it 12mm from the centre. The mask was fitted into the MCP holder in such a way that it was in contact with the MCP. A piece of DEF was exposed with the MCP and mask in place, the exposure recorded on the reference diode was 10000nC. The resultant image is shown in figure 5.12(a). Scattering wings are clearly visible on both the line and true foci. Note that the extended structure to the right of the image is due to the window on the front of the camera being broken so that part of the film was exposed to the light. The actual X-ray image is not believed to have been affected. Microdensitometer scans were made along the scattering wings (figure 5.13). Estimates of the surface roughness and its correlation length were made from them. For a first order approach to the analysis of this type of image Church, Jenkinson & Zavada (1979) define two integrals:

$$I_s = \int_{\phi_1}^{\phi_2} I(\phi_{scat}) d\phi_{scat} \tag{5.7}$$

and

$$I_{ms} = \int_{\phi_1}^{\phi_2} I(\phi_{scat}) \phi_{scat}^2 d\phi_{scat} \tag{5.8}$$

Roughness can occur on given surface on a number of different length and height scales simultaneously. Any method of measurement of roughness will be sensitive only to a certain range of correlation lengths limited, in this case, by the scattering angles at which it can detect radiation, which are in turn limited by the angular extent of the mouth of a channel and the breadth of the specular (non-scattered) beam. We must accept this as a limitation of the experiment and choose the limits on the integrals ϕ_1 and ϕ_2 such that they encompass the range of scattered angles at which a ray can exit the channel.

Church et al. further inform us that the surface roughness σ averaged over the spatial wavelength range that we are sampling is given by:

$$\sigma^2 = \left(\frac{\lambda}{4\pi\theta}\right)^2 \frac{I_s}{I_0} \tag{5.9}$$

where θ is the grazing incidence angle and I_0 is the total reflected (plus the scattered) flux. The range of spatial wavelengths to which this experiment was sensitive is $3 - 74\mu$m limited at one end by the $L : D$ ratio of the channels and at the other end by the breadth of the specular beam. A measure of the correlation length τ is given by:

$$\tau = \frac{2\pi\sigma}{\sqrt{m}}; \qquad m = \frac{1}{4}\frac{I_{ms}}{I_0} \tag{5.10}$$

126

Application of these equations to microdensitometer scans across a line focus, using a trapezium approximation to the integration yield an RMS roughness $\sigma = 30\text{Å}$ with a correlation length $\tau = 17\mu\text{m}$.

The accuracy of these measurements must be compromised by the fairly large (0.5mm) hole in the mask which resulted in twelve channels rather than one being illuminated. Furthermore misalignment between these channels resulted in a broad (FWHM=5′) specularly reflected beam which must similarly broaden the scattered component. The rather crude method employed to isolate a single X-ray energy also introduces an uncertainty. However, a strength of the technique is that the X-rays are shining into the channels of an actual MCP, probing its surface in a non-destructive way (cf the AFM measurements described in chapter 6). Another important point is that we are sampling the range of spatial wavelengths which will degrade the image, in terms of resolution, as the MCP is being tested in the same geometry as it would be used and only rays that are scattered at such an angle that they come through into the detector are observed.

In conclusion, this technique shows great promise as a means of investigating the surface roughness of microchannels, which will undoubtedly be an important issue in the development of these optics. The experiment described here is a rather hasty first attempt, yet its results are in broad agreement with those of Kaaret et al. (1992) who obtained $\sigma = 57\text{Å}$ and $\tau = 1.41\mu\text{m}$ by means of an optical profilometer. It also highlights the areas which need improvement before a working test facility is realised, namely number of channels illuminated and spectral purity of the radiation.

5.4.5 Image of $C_{Ly-\alpha}$ (0.37keV) X-rays focused by GEO4

One image (figure 5.12 b) was recorded, on Chinese film, of 0.37keV X-rays focused by the MCP known as GEO4. The distances l_s and l_i were 197mm each, as they were when measurements were being made using the X-ray diodes. The image clearly shows the diffuse, cruxiform and true focus components of the image. The chequer-board pattern in the diffuse component is particularly clear. Indeed, the contributions of individual channels to this diffuse component are easily resolved and multifibre boundaries and rotational misalignments between multifibres can be seen. Comparison of this image with the basic simulation of this geometry and X-ray energy

in figure 2.6 shows a good agreement. The image appears sharper than similar ones presented elsewhere in this thesis. The reason for this is, as the attentive reader will already have noted, the shorter l_s and l_i, which lead to the angular misdirections of the X-rays passing through the plate being converted into smaller linear misplacements in the image plane. Unfortunately this image is overexposed (100nC on the reference diode) to the extent that no meaningful microdensitometer scans could be made of the focus - pressure of time at RAL meant that a rerun with less exposure was not possible.

5.4.6 Image of Al_{He_α} (1.59keV) X-rays focused by Slump 1-b

An image of 1.59keV X-rays focused by the Philips slumped circular pore MCP Slump 1-b was recorded on DEF film. The exposure was 2000nC on the reference diode. The MCP was used in so-called beam expander mode *ie* with the source on the concave side. Equation 1.1 and the length of pipe available dictate the necessary l_s and l_i which were chosen to be 250mm and 1026mm respectively. The resulting image is shown in figure 5.12(c). The image is a little out of focus, due either to incorrect positioning in the tube or, possibly due to the uncertainty in the information from Philips regarding the radius of curvature ($\pm 5\%$). Because of this incorrect focus the familiar doughnut shaped image is visible. This doughnut-type image may well prove to be more useful for characterisation of circular-pore MCPs than a "correctly focused" one as departures from the circular symmetry are easily detected. Indeed Zhao *et al.* (1993) report using just such a disfocused image for calibration of Wolter type 1 mirrors for use on the AXAF telescope.

The circular arcs described in section 2.6.3, previously invisible in images of X-rays focused by MCPs, are clearly seen in this image. The high resolution of X-ray film combined with excellent statistics provided by the intense point-like source again shows its power as a diagnostic technique for these optics.

Chapter 6

Metrology and modelling of focusing MCPs

6.1 Introduction

In Chapter 2 the geometry of MCP optics was introduced, idealised MCPs were discussed and a Monte Carlo ray-trace model of their optical properties was described. The experimental results reported in Chapters 3-5 show reasonable agreement with the predictions of the model but due to imperfections in the channels and the channel arrays, there are some discrepancies. In particular, the focal spots from the square pore plates are much broader than the ideal plate model suggests they ought to be. Imperfections will always limit the performance of these optics, so it is important to investigate their nature and relative importance.

Considerable effort has gone into the metrology of square pore MCPs to determine the exact causes of the broadening of the point spread function. This metrology has included optical microscopy; scanning electron microscopy (SEM); atomic force microscopy (AFM) as well as the X-ray scattering measurements described in section 5.4.4. An equally considerable effort has been devoted to incorporation of the imperfections so discovered into the ray-trace model. The outcome of this work is a Monte Carlo model whose output closely corresponds to the focused images presented in Chapters 3 and 5. The model is sufficiently comprehensive that it may

be used in future to set manufacturing tolerances, predict the effect of trading off one feature against another and so on.

The main imperfections that have been investigated are:

- distortions of the channels

- roughness of the channel surfaces

- misalignments of the channels within a given multifibre

- misalignments of the multifibres relative to each other

This chapter will deal with the metrology and modelling of each of these distortions in turn, before bringing them all together into a comprehensive model of a real-life square pore microchannel plate. Throughout the chapter images are presented which result from simulations of focusing by Galileo type plates (section 3.3.1) which exhibit just one type of characteristic distortion. To render the effects of the distortion easily visible, its severity, in each case, is twice that found to be present in the Galileo plates. FWHM resolution values are reported for simulations in the same geometry but with the distortions set at the levels determined experimentally. Most simulation images shown in this thesis have been recorded in 500×500 arrays representing an area of 100×100mm, so that one pixel corresponds to a 0.2mm square. These pixels are large enough to introduce significant blur to the foci since the FWHM extent of the central focus is only 170μm for an ideal Galileo type plate. For the FWHM measurements reported below special high resolution images have been recorded, again in 500×500 arrays but now corresponding to an area of only 5×5mm. The pixel size is therefore 10μm reducing the intrinsic blur to an acceptable level.

6.2 Distortion of the channels

The main types of channel distortion seen in square pore MCPs are: (i) "pincushion" where the channel walls are not planar but bow in towards the centre of the channels and (ii) striations running along the length of the channels. The SEM photograph, figure 6.1(a) shows pincushion

distortion at the mouths of several of the channels belonging to the etched-only Philips plate LD061-14 (section 3.2). The SEM images of figures 6.2(a) and (b) show striations on a channel surface, again of LD061-14, as revealed after sectioning with a diamond saw. The spacing of these parallel grooves is approximately 0.3μm.

Kaaret et $al.$ (1992) report that they detected both these types of distortion in a hydrogen fired square pore MCP from Galileo, using an optical profilometer. They measured the saggital depth as 189nm for a 41.2μm wide central section of the channel, so that the depth as a fraction of the width was $g/D = 4.5 \times 10^{-3}$. Unfortunately we have not been able to make measurements to confirm this figure at Leicester, so for the modelling described below the result of Kaaret et $al.$ has been used. The SEM work showed that some channels are grossly distorted so that their openings take on all kinds of bizzare shapes, these are however, a very small minority. The only distortions visible in the great majority of channels are those described above. The exact origins of these imperfections are unclear. Pincushion is thought to be a product of the drawing process. The cause of the striations may be the fact that, certainly in the case of the Philips plates, the core bar was not originally square in cross-section but was ground down from a cylindrical original. The core bars used in future plates must be originally square and be optically polished in order to minimise mechanical damage at the core-cladding interface.

Figure 6.1(b) shows that the vertices of the channels are slightly rounded or "radiused". This rounding is deliberately built in by the manufacturer because glass bars with sharp corners are prone to chipping during handling. Any rays which stray into the corners of the channel will be subject to reflection in a non-ideal direction due to the curved edge. In the Galileo plates of section 3.3.1 the radii of the curved sections have been found to be 2μm. The channel side length is 85μm, therefore 4.8% of the channel surfaces lie on these curves. The Philips plates show a proportionately similar radiusing. These curves are a nuisance from the point of view of X-ray focusing and manufacturers must be encouraged to minimise them in future generations of plates.

A further deviation from cuboidal channels is seen in some square pore plates - "funnelling" of the channels. Again this is not strictly a distortion but a deliberately induced characteristic, designed to increase the open area fraction on the front surface of plates intended for use as multipliers. It is achieved by "aggressively" etching the plate so that some cladding glass is

131

a

b

15KV   0.57KX   17.5M   5194   LD061/14

15KV   565X   17.7M   8430
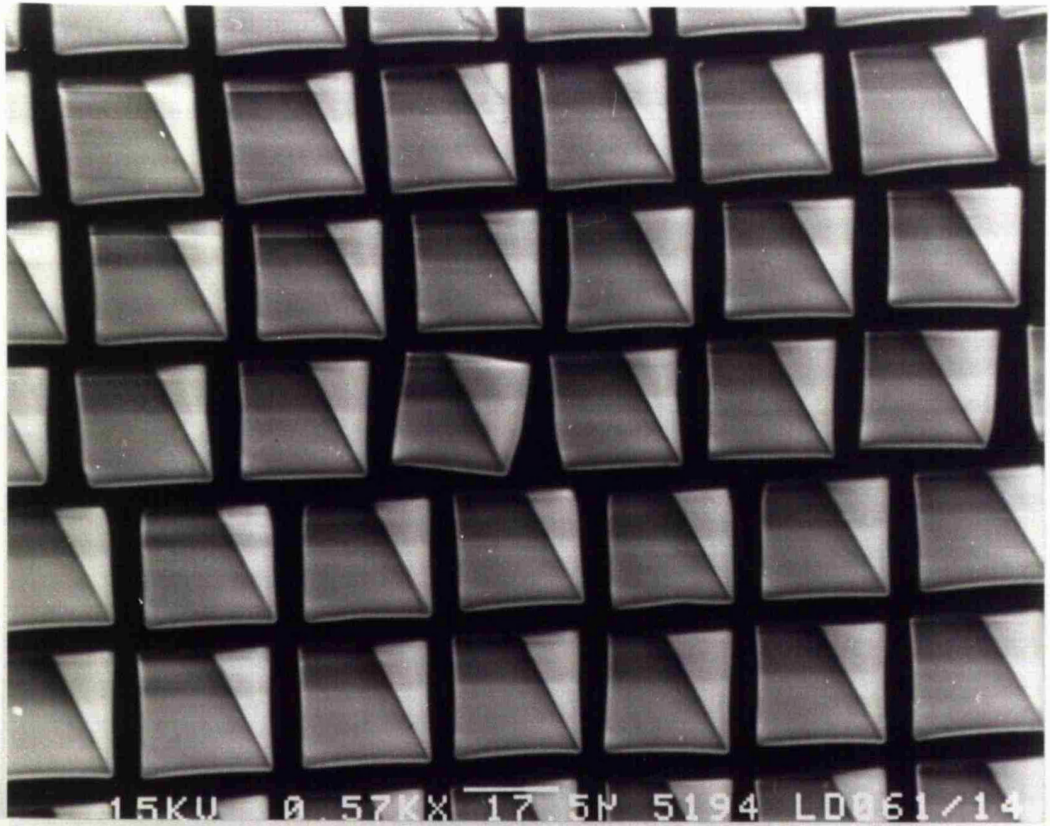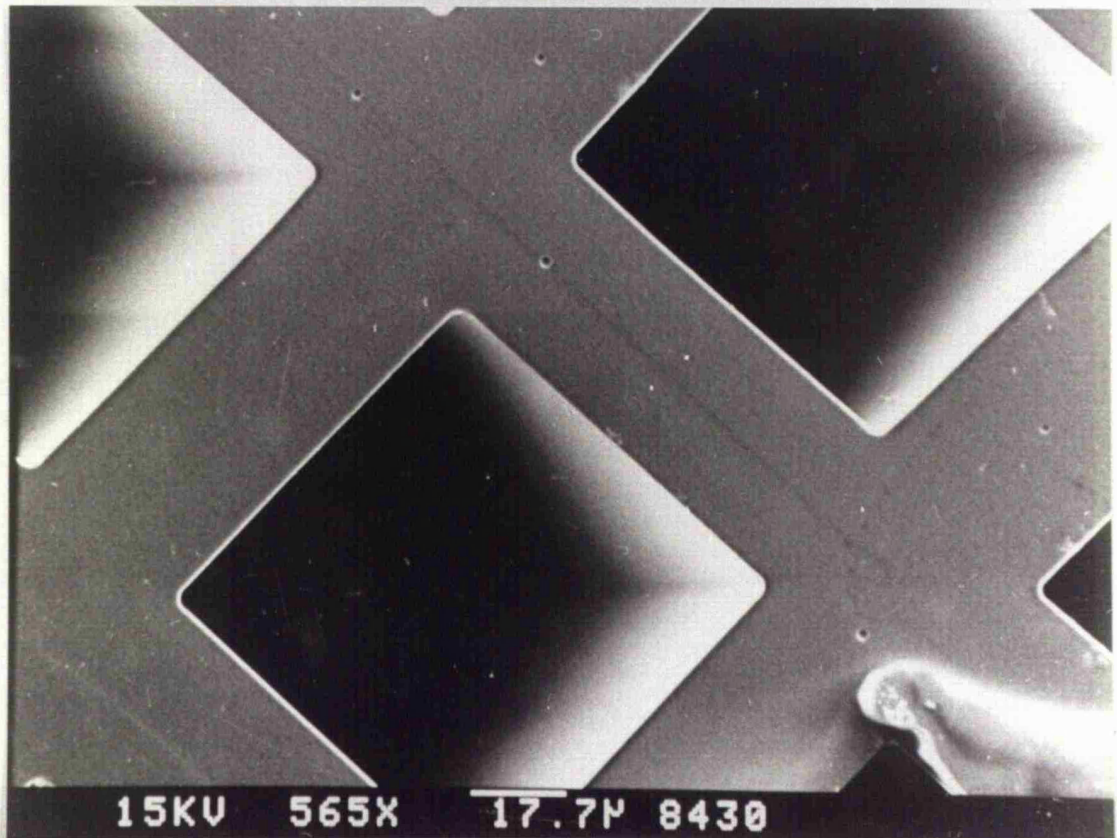
Figure 6.1: SEM photographs of (a) the Philips MCP LD061-14 showing pincushion distortion at the channel entrances and (b) the Galileo MCP GEO3 showing radiused channel corners.

a

15KU 2.20KX 4.55μ 6704 TUBE

b

15KU 11.0KX 909n 6703 TUBE
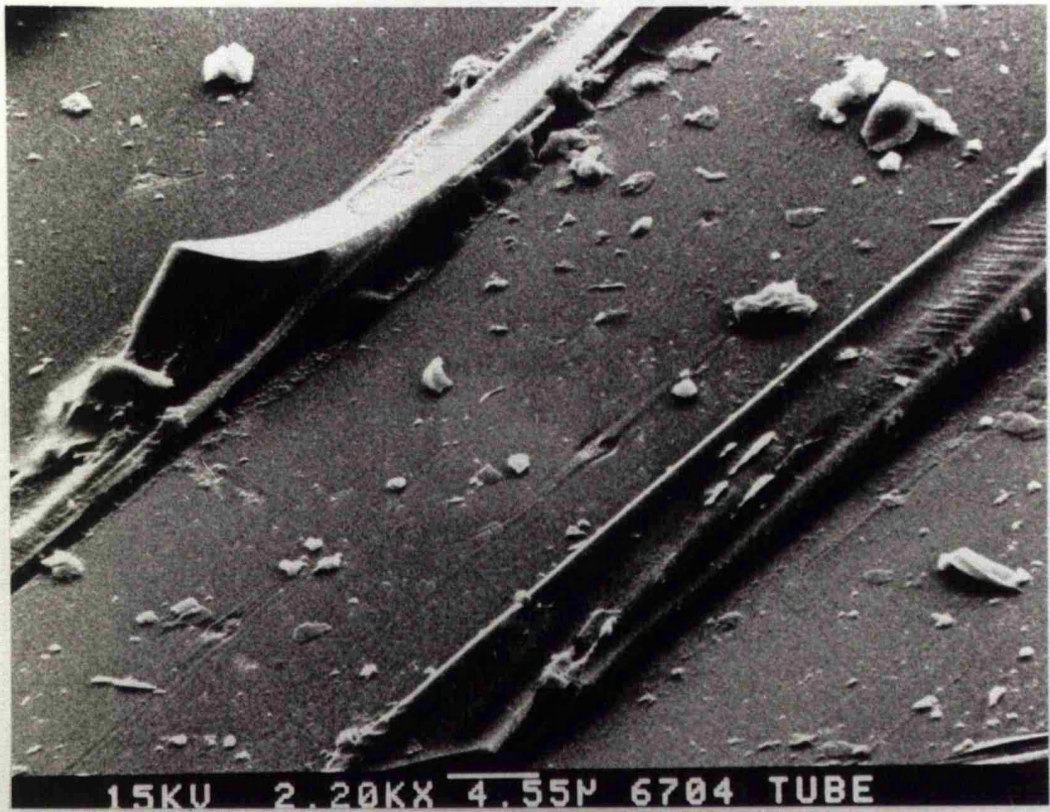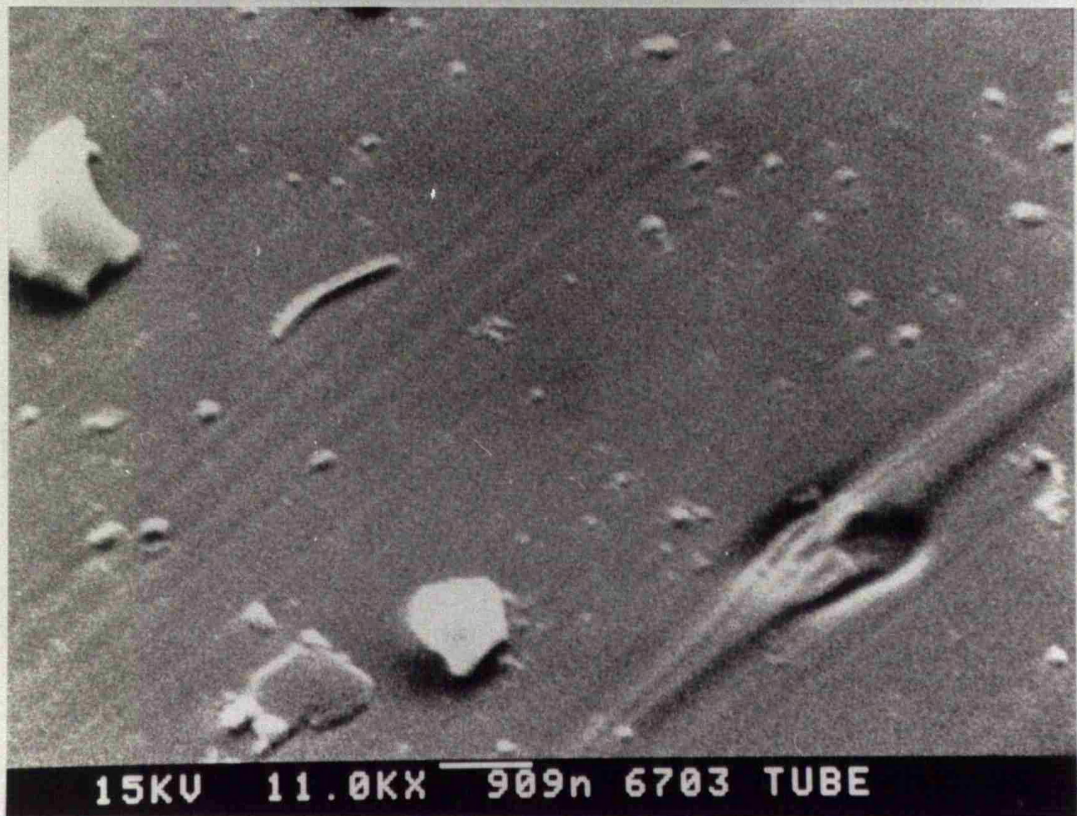
Figure 6.2: SEM photographs of the Philips MCP LD061-14 after cutting with a diamond saw. (b) is an increased magnification version of (a) Striations on the channel surface are visible as is considerable debris due to the sawing.

removed as well as the core. Funnelling can be detected by looking at both faces of a plate under the SEM. If A_{open} is greater on one side than the other then the channels must certainly be funnelled. Plate GEO2 from Galileo was found to exhibit channel funnelling which seriously compromised the results obtained by illuminating it with X-rays (section 3.3.4).

6.2.1 Modelling distorted channels

A model of pincushion distortion has been formulated but no attempt has, as yet, been made to model the effect of the striations other than via the general scattering from surface roughness described in section 6.4.3. Kaaret *et al.* (1992) present a complex analytical model of scattering from the striations. This model represents the parallel grooves as a perfect diffraction grating which causes circular arcs in the image plane. These curves are clearly visible surrounding the focused spot in figure 3.13. No modelling of the rounded-off channel edges has been done at this stage, as it affects only 5% of the rays it was deemed to be of low priority. These rounded corners merit some future modelling effort because there has been speculation that they and not the striae cause the circular arcs of figure 3.13.

Similarly no model of funnelled channels has been set up, simply because plates with funnelled channels are unsuitable for X-ray focusing.

The code which includes distortions and misalignments of the planar square pore MCP has the same structure as the code described in section 2.4 which models idealised plates. For the purpose of determining whether a photon enters a channel or not, the channel mouths are still treated as squares with their centres on a regular square array. Strictly speaking, this is not accurate: we should check whether the rays entered a distorted and rotated channel mouth. Including this detail would make little difference to the operation of the model which only requires the proportion of the rays entering each channel. It is only after we have decided that a ray has entered a channel that we start treating the channel as being distorted and misaligned

For the purpose of modelling distortions it is simpler to deal with a channel with its axis lying on the z-axis and its centre at the origin, rather than at some other point on the plate. Whichever channel the ray has entered will have, in the terminology of section 2.4.1, a pair of integers (C_x, C_y), which represent its position in the rectangular grid relative to the central channel.
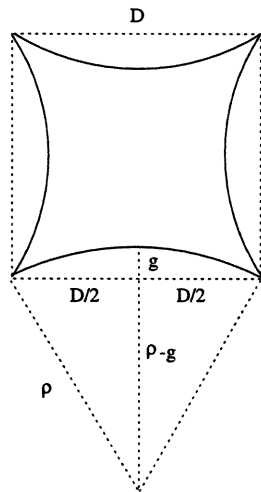
Figure 6.3: Construction used to determine cylindrical radius ρ for a pincushioned channel; we may use Pythagoras' theorem on one of the triangles to obtain ρ.

The ray, as it enters a channel, can be translated to an equivalent point on the central channel which then has distortion and misalignment applied to it. The ray's path along this channel is calculated and the point where it exits is determined. From that position a reverse translation is applied to take it back to the point where it would have left the channel that it originally entered. If the entry point is $(x, y, -L/2)$, we translate to a point $(x - pC_x, y - pC_y, -L/2)$ on the central channel, the direction vector of the ray remaining unchanged. On leaving the plate we translate the exit position back by adding pC_x and pC_y to the respective x and y exit coordinates.

In the model that has been established for pincushion distortion, the channel walls are treated as sectors of cylinders. Figure 6.3 shows a channel with exaggerated pincushion distortion. Equations representing cylinders parallel to the z axis are of the form:

$$(x - x_0)^2 + (y - y_0)^2 = \rho^2 \qquad (6.1)$$

where m and n are the x and y coordinates of the axis of the cylinder and ρ is its radius given,

135

in terms of the channel side length D and the saggital depth g by:

$$\rho = \frac{g}{2} + \frac{D^2}{8g} \tag{6.2}$$

according to the construction indicated in figure 6.3. It can also be seen from this figure that the cylinders have the equations:

$$(x - \rho + D/2 - g)^2 + y^2 = \rho^2 \tag{6.3}$$

$$x^2 + (y - \rho + D/2 - g)^2 = \rho^2 \tag{6.4}$$

$$(x + \rho - D/2 + g)^2 + y^2 = \rho^2 \tag{6.5}$$

$$x^2 + (y + \rho - D/2 + g)^2 = \rho^2 \tag{6.6}$$

To calculate the intersection position of the ray and the cylinder the ray equation $\mathbf{r} = \mathbf{a} + t\mathbf{b}$ must be solved for t simultaneously with the four cylinder equations above. The solution which gives the smallest positive value for t gives us the wall the ray will strike first. The intersection position may be obtained by substituting the appropriate t value back into the ray equation, as described for an ideal circular cross-section channel in section 2.6.2. The normal vector is easily obtained; it is the vector to the intersection point from its projection on the channel axis.

6.2.2   Results

Figure 6.4 shows images resulting from simulations of point-to-point MCP focusing using a square pore Galileo type plate with 1.59keV X-rays in the geometry established for the RAL experiment of Chapter 5 ($l_s = l_i = 644$mm). For comparison, figure 5.8(b) is an actual X-ray image produced when GEO4 was illuminated by the laser plasma source at RAL. Figure 6.4(a) results from a simulation of an ideal MCP while (b) is the image formed by a plate with pincushion distortion twice as severe as that reported by Kaaret *et al.* (1992) *ie* $g/D = 9 \times 10^{-3}$. In both the figures the logarithm of the intensity has been plotted in order to allow features at opposite ends of the images' dynamic range to be shown on the same diagram.

The image from the pincushion distortion simulation shows a broadening of the cross arms towards their ends and also a broadening of the central focus with lobes emerging from it between the cross arms. The broadening occurs because rays striking the cylindrical channel
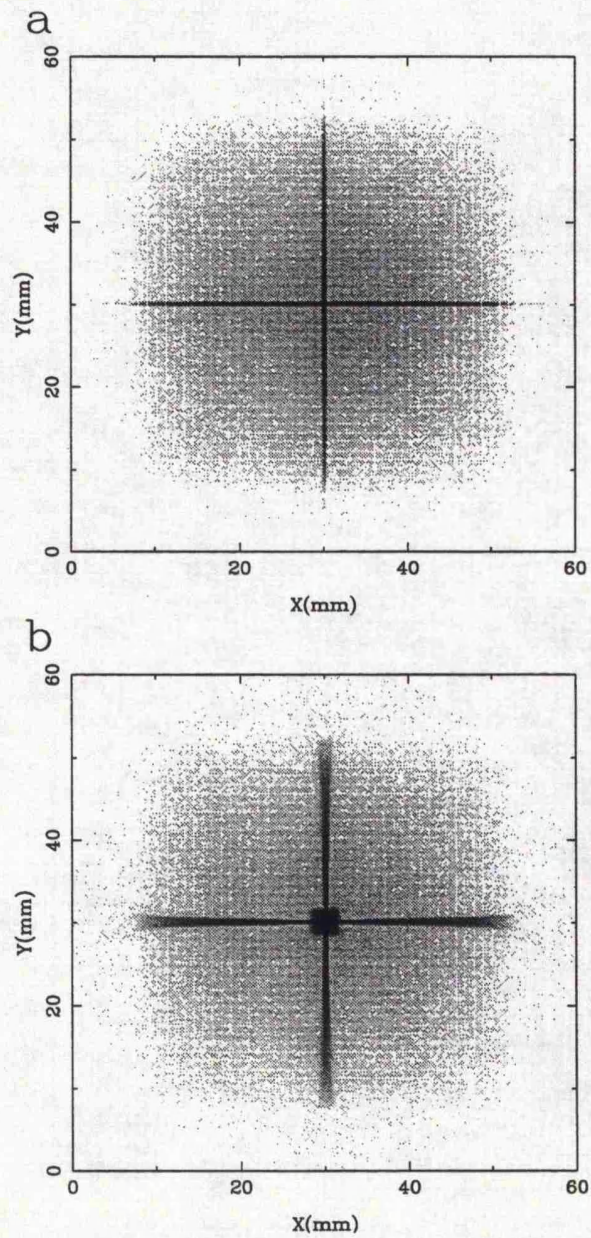
Figure 6.4: Logarithmic plots of images from simulations of focusing in the geometry of the RAL 1.59keV experiments (section 5.4.2), (a) is a simulation of an idealised Galileo MCP illuminated by 1.59keV X-rays, (b) incorporates pincushion distortion.

137
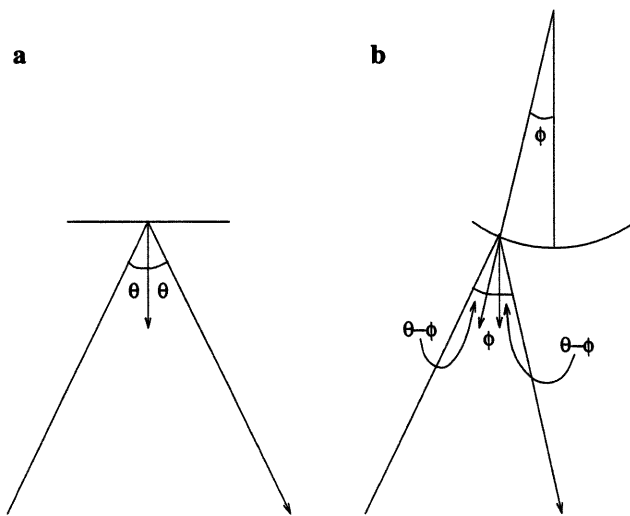
Figure 6.5: The projection of a ray path onto the xy plane showing the effect of pincushion distortion on the ray path. The normal at the point of incidence is rotated by an angle ϕ_p from its direction in the planar wall case. This alters the reflection direction of the ray by $2\phi_p$.

wall are subject to a reflection out of the ideal (planar wall) direction (figure 6.5). The amount of angular deviation from the planar channel direction for a given ray depends on where on the curved surface the ray falls. This position determines the degree of rotation of the normal away from the planar channel normal direction. The nearer the edge of the channel the ray falls the greater the normal rotation will be (once again see figure 6.5) The broadening is greater at the ends of the cross arms because the projection of the ray path between the channel and the image plane onto the xz or yz plane is longer for rays which fall at the ends of the cross arms. Hence the same angular offset is converted into a larger linear one for these rays than for rays which fall closer to the centre of the distribution. The broadening of the central focus is due to the same effect occurring doubly, once in each reflection plane, during the ray's progress along the channel.

A measurement of the FWHMs of the central peak in the simulated images from a perfect plate and from one with pincushion distortion of the actual severity measured by Kaaret et $al.$ yields the following: FWHM=0.27mm for the perfect plate (note that the peak is broadened beyond the theoretical figure of $2D = 0.17$mm by the 8° bias angle); FWHM=0.71mm for the pincushioned plate. We see that a significant contribution to the breadth of the focal spot is due to pincushion distortion of the walls.

6.3   Channel Misalignments

When square pore MCPs are examined under a high powered optical microscope or an SEM, deviations from the regular square array of square channels are invariably visible. Errors in the square array can essentially be split into two categories. Firstly, translations of multifibres with respect to one another and secondly, rotation of square channel openings relative to others in the same multifibre or rotation of multifibres with respect to one another. The translations do not degrade the image, as long as a channel's walls are parallel to the xz and yz planes it will focus rays to the ideal cruxiform or true foci so these are not modelled. Channel rotations are generally more pronounced near the multifibre boundaries. This is a consequence of the fusion process used in manufacture, where pressure is applied to a heated bundle of fibres to induce cohesion. Where the fibres are being forced together there is a tendency for both the

channels and the array to become squashed and therefore distorted. Figure 6.6 shows some SEM photographs of channel plates which illustrate the prevalence of distorted and rotated channels near to the clearly visible multifibre boundaries.

There is a second important class of channel misalignments, namely misalignments of the channel long axes. In a perfect planar MCP all the channel axes lie parallel to the optic axis of the system. In practice they are inclined at small angles to the xz and yz planes. These misalignments have not been directly measured in this work but have been inferred by modelling all known distortions and attributing the residual deviation from the ideal image to them. This technique is not as hit-or-miss as it may initially sound because this type of distortion manifests itself in the image in a characteristic way (section 6.3.3 below).

One possible means of measuring the long axis misalignment might be provided by the RAL laser plasma source, described in Chapter 5. The images recorded on X-ray film at RAL provide such high resolution that it would be possible to illuminate small sections of a plate with the laser plasma X-ray source and from the positions where the reflected output beams from single channels (easily resolved for the 85μm channels of the plate GEO4) expose the film build up a distribution of misalignment angles.

Figure 5.12(a), which was recorded with a mask pierced with a single pinhole placed in front of the focusing MCP shows exposed spots caused by just such single channel output beams. The relative alignment of the channels illuminated can be measured from their positions. In this case only twelve channels were illuminated - not enough to tell us much about the distribution of misalignment angles.

A second method which might be of use for determining the long axis misalignment distribution might be that of Hassler, Rottman & Lawrence (1990) which involves photographing each side of an accurately mounted MCP, searching for blocked pores (which are always present in small numbers) and comparing their positions on each side of the plate. Hassler *et al.* have performed this painstaking work on curved channel MCPs, so called "C plates" (Timothy 1981). These would be expected to have larger front to back misplacements than a straight channel plate and indeed the results of the above authors confirm this. The technique may prove sensitive enough for use with MCP optics, a full study will be required to assess its feasibility.
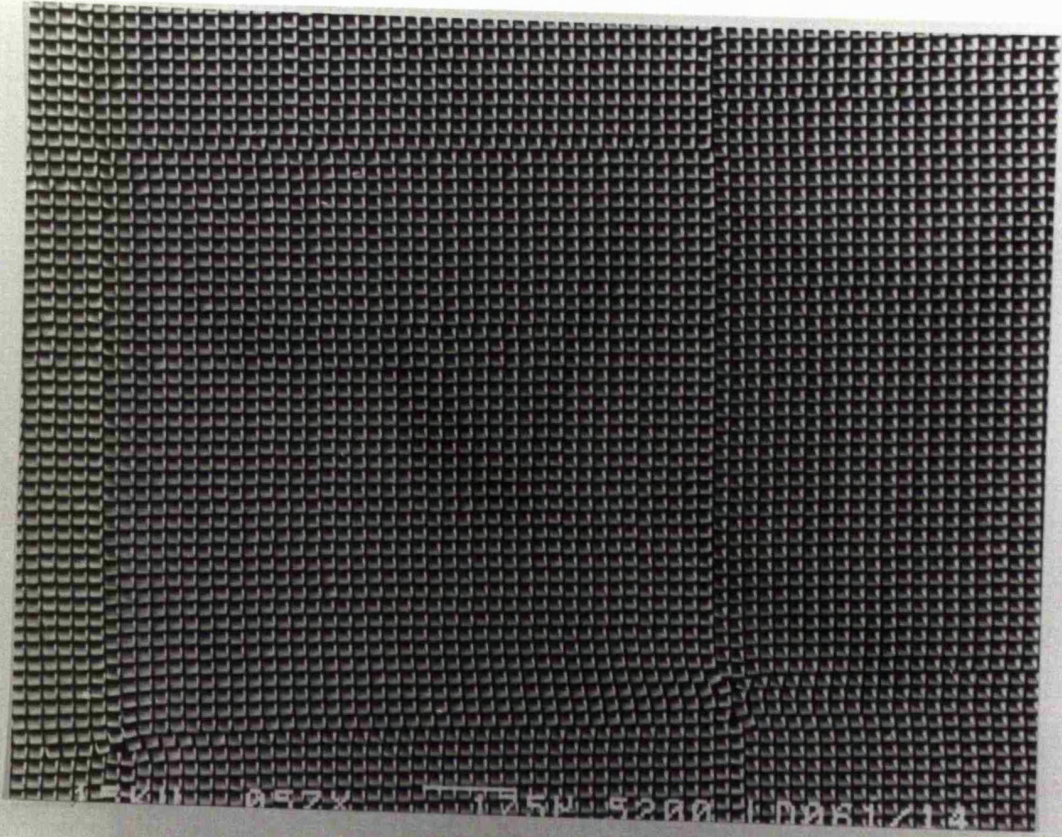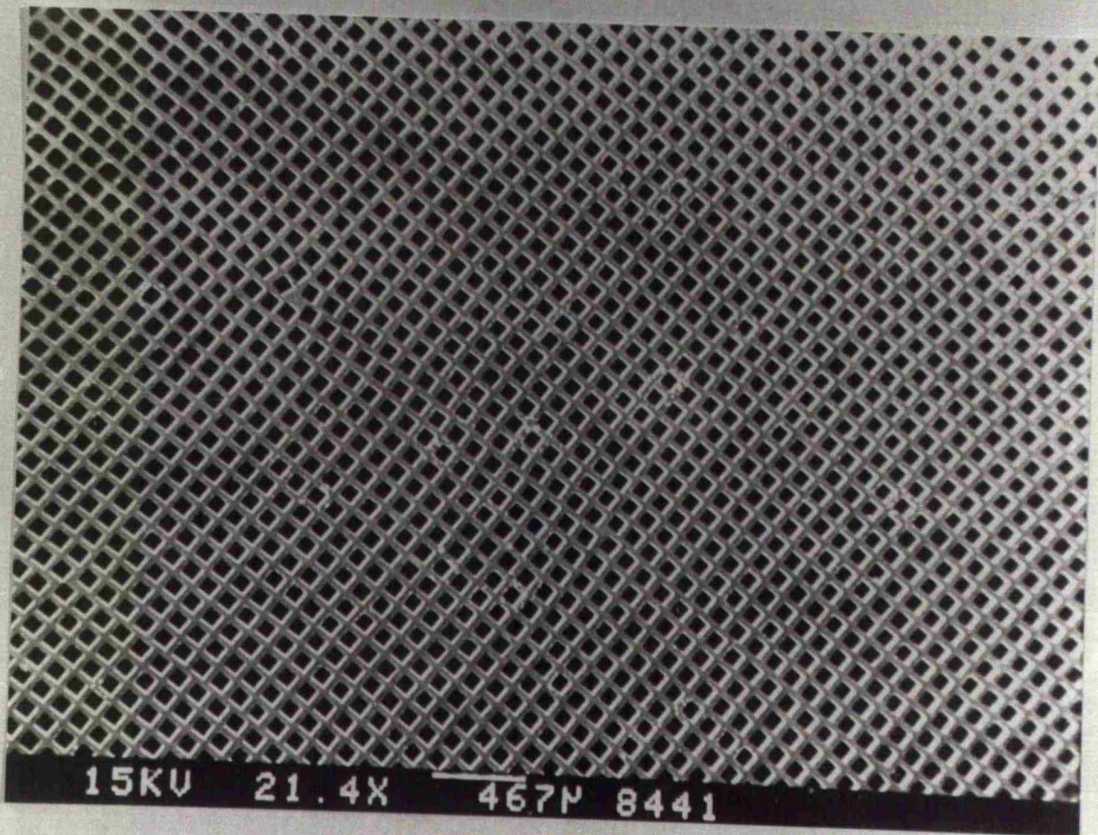
Figure 6.6: SEM photographs of (a) the Philips MCP LD061-14 (b) the Galileo MCP GEO3 showing multifibre boundaries. These boundaries are the areas where distortions to both the channel and the channel array are prevalent.

n = 1   2   3   4
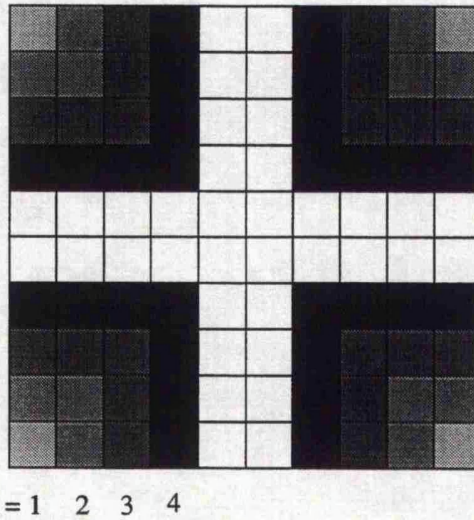
Figure 6.7: The weighting scheme used for channel rotation measurements. The rotation of the nth channel on the diagonal of the multifibre is taken to be representative of the 4(2n-1) channels in the four similar chevrons, one of which it lies at the apex of.

6.3.1 Metrology of channel rotations

Measurements of channel rotations were made on both Philips LD061 plates and the Galileo plate (GEO2). The distribution of rotations, relative to an arbitrary set of Cartesian axes, was found by inspection with a powerful optical microscope equipped with a rotatable eyepiece graticule.

A sampling scheme was devised which would take into account both multifibre rotations and individual channel rotations. The multifibres are, in cross-section, squares of $N \times N$ channels, for the Galileo plates $N = 16$, while the Philips MCPs have $N = 40$. Measurements commenced in the corner channel of one multifibre, then the microscope was moved diagonally across to the second channel on the diagonal of the next multifibre, then across to the third channel on the next and so on, until the central $(N/2)$ channel of the fibre was reached. Repeat sets of measurements were made from different starting points. The nth measurement in each set was taken to represent all the channels in the nth row and column from the edge of the tile to the (n, n) position, as shown in figure 6.7. To account for the varying numbers of channels in these chevrons weighting factors $4(2n - 1)$ were introduced. The distributions resulting from these

142

weighted measurements are Gaussian. The plates exhibited similar standard deviations: 1.09° for the Galileo plate and 1.20° for the Philips one.

A straightforward measurement of the angles between the multifibres and arbitrary Cartesian axes gave angular distributions with RMS deviations of 1.29° (Galileo) and 0.4° (Philips).

A further set of weighted measurements was performed on the Galileo plate only, using the scheme described above but moving along the diagonal of a single multifibre, to obtain the distribution of rotations within the tile. This work yielded a standard deviation of 0.86° for the Galileo plate.

Theoretically the total misalignment standard deviation should equal the quadrature sum of the within-multifibre and between-multifibre values, subject to some error due to the finite number of channels measured. The similarity between the overall RMS rotation values obtained for the two plates, when compared with the greatly superior focusing properties of the Galileo plate (see Chapter 3) suggest that these channel rotations are not of primary importance as causes of image distortion. In section 6.3.3 below it will be shown that they have no effect on the width of the central focus.

6.3.2 Modelling misalignments

Misalignments may be represented by three separate rotations of the normals (**i**, -**i**, **j** and -**j**) to the four planes which represent the channel as illustrated by figure 6.8. Rotations in the xz and yz planes correspond to misalignments of the channel axis, while a rotation in the xy plane represents a twisting of the channel about its axis. These rotations are effected by multiplying the channel normal vectors by matrices.

$$\mathbf{G}_i \mathbf{r} = \mathbf{r}' \quad i = 1, 2, 3 \tag{6.7}$$

$\mathbf{G}_1$, $\mathbf{G}_2$ and $\mathbf{G}_3$ represent rotation in the xz, yz and xy planes respectively and are given by:

$$\mathbf{G}_1 = \begin{pmatrix} cos\phi_1 & 0 & -sin\phi_1 \\ 0 & 1 & 0 \\ sin\phi_1 & 0 & cos\phi_1 \end{pmatrix} \tag{6.8}$$
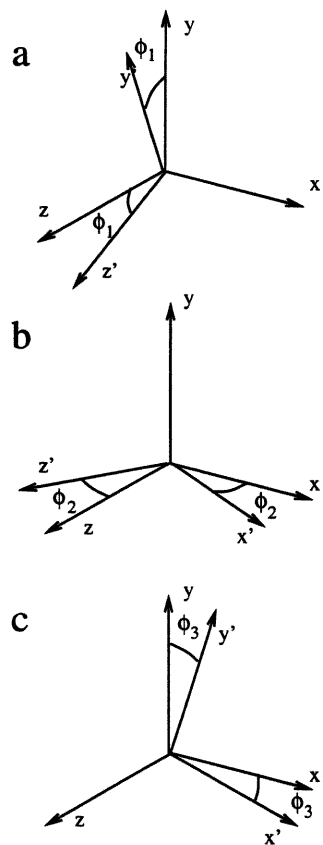
Figure 6.8: The three rotations use to model channel misalignments (see text). The z-axis corresponds to the channel long axis and in a perfect channel the walls would lie in the xz and yz planes, (a) and (b) represent misalignments of the channel long axis while (c) represents a rotation of the channel about its axis.

$$G_2 = \begin{pmatrix} 1 & 0 & 0 \\ 0 & cos\phi_2 & -sin\phi_2 \\ 0 & sin\phi_2 & cos\phi_2 \end{pmatrix} \qquad (6.9)$$

and

$$G_3 = \begin{pmatrix} cos\phi_3 & sin\phi_3 & 0 \\ -sin\phi_3 & cos\phi_3 & 0 \\ 0 & 0 & 1 \end{pmatrix} \qquad (6.10)$$

where ϕ_1, ϕ_2 and ϕ_3 are the respective rotation angles. These three matrices may be combined, by multiplication, into one matrix which contains all three misalignments, this is:

$$G = G_1 G_2 G_3 \qquad (6.11)$$

so

$$G = \begin{pmatrix} cos\phi_3 cos\phi_1 & -cos\phi_3 sin\phi_1 sin\phi_2 + sin\phi_3 cos\phi_2 & -cos\phi_3 sin\phi_1 cos\phi_2 - sin\phi_3 sin\phi_2 \\ -sin\phi_3 cos\phi_1 & sin\phi_3 sin\phi_1 sin\phi_2 + cos\phi_3 cos\phi_2 & sin\phi_3 sin\phi_1 cos\phi_2 - cos\phi_3 sin\phi_2 \\ sin\phi_1 & cos\phi_1 sin\phi_2 & cos\phi_1 cos\phi_2 \end{pmatrix}$$
$$(6.12)$$

If we are treating the surfaces as planes, multiplication of the normal vectors by this matrix imparts both rotation about the long axis and misalignment of that axis to the channel. For channels with pincushion distortion, due to the cylinders which are the walls being defined with reference to a line representing their axis, a straightforward multiplication is not possible. An alternative but equivalent approach is used. The *ray* is rotated using multiplication of both **a** and **b**, the entry point of the ray into the channel and the ray direction respectively, by matrix **G**, while the channel is left unchanged. After all reflections in the channel are completed the ray is transferred back to unrotated co-ordinates by fore multiplication of **a** and **b** by the inverse matrix G^{-1}. An analytical inversion of **G** would be tedious in the extreme, so a standard numerical inversion routine (from NAG [1]) is used within the code.

The three misalignment angles ϕ_1, ϕ_2, ϕ_3 are all made up of two components: the misalignments of the channels within the multifibre and the misalignments between the multifibres (sections 6.1 and 6.3.1 above). The multifibre misalignments are generated randomly using a Gaussian distribution by a NAG routine before execution of the ray trace code. They are stored in an

---

[1]Numerical Algorithms Group Limited, NAG Central Office, Wilkinson House, Jordan Hill Road, OXFORD, OX2 8DR, United Kingdom.

$m \times m \times 3$ array in which each element is an 8 byte number, m is the number of multifibres across the plate and is given by:

$$m = \frac{2R_{mcp}}{pN} \tag{6.13}$$

where N is, as above, the number of channels along the side of a multifibre. For the Galileo plate $m = 17$ and for the Philips one $m = 39$

To store angles for every individual channel in this way would be very demanding in terms of memory: the Galileo plates have approximately 5.7×10^4 channels, while the Philips ones have about 2.7×10^6, requiring 1.4MB and 65MB respectively to store their misalignment information. Using the computers available at the present time, the latter figure is prohibitively large. Individual channel misalignments are generated, again randomly with a Gaussian distribution, during the ray-tracing code at the point when the ray enters the channel. This results in multiple rays passing through the same channel each experiencing different misalignments.

6.3.3 Results

Channel rotations

Figure 6.9 shows the effects of (a) individual channel rotation and (b) rotation of whole tiles. The plate modelled had the dimensions of a Galileo square pore MCP ideal apart from the rotation under investigation and illuminated with 1.59keV X-rays in the RAL geometry of Chapter 5. Again logarithmic plots have been used. In both cases we see the cruxiform arms fanning out at their ends giving a "Maltese Cross" type image. In figure 6.9(a) the fanning out is smooth due to the random rotation angles of the channel (section 6.3.2) whereas in (b) the cross arms are broken into discrete sections as all the channels in each multifibre have the same rotation angle.

These images, particularly (a) look very similar to figure 6.4 which was generated by a simulation of the focusing action of a plate with pincushion distortion. In section 6.2.2 above, the effect of pincushion distortion was explained in terms of a rotation of the channel normal in the xy plane. This is exactly what happens when the channel is rotated about its normal. The great number of channels, all with different rotation angles builds up the smooth distribution seen in figure 6.9(a). The relative effects of pincushion with a given saggital depth g and channel

146
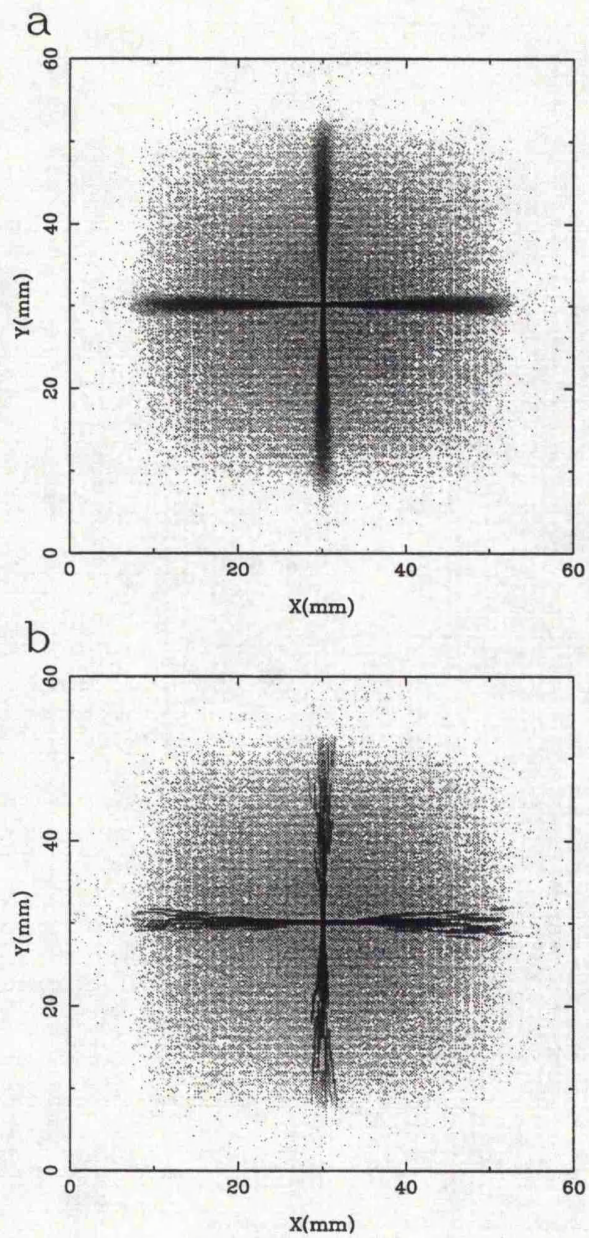
Figure 6.9: Logarithmic plots of images resulting from simulations of a Galileo square pore type plate illuminated by 1.59keV X-rays in the RAL geometry, (a) channel and (b) tile rotations have been modelled, both twice as severe as measured from plate GEO2.
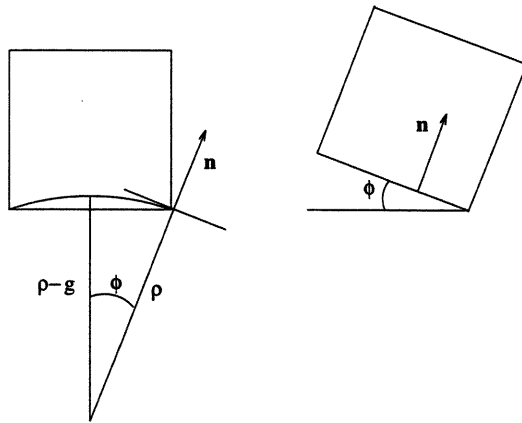
Figure 6.10: Rotation of the channel has a similar effect, on singly reflected rays, as pincushion distortion.

rotation through a given angle may be compared by means of the construction shown in figure 6.10. We see that

$$cos\phi = \frac{\rho - g}{\rho} = 1 - \frac{g}{\rho} \qquad (6.14)$$

so that if we choose some suitable standard deviation for our Gaussian rotation distribution (say $\phi/2$) the effects on singly reflected rays of the pincushion and of the channel rotations will be almost the same. In this way we can directly compare the relative effect on the cruxiform structure of the two distortions for a given plate.

A more important result of pincushion channel distortion is, of course, the broadening of the central focal spot. Channel rotations have *no effect* on the FWHM of the central peak. The reason for this is that in passing along a rotated channel the ray is still reflected from two orthogonal walls; this is the requirement for focusing. Rotation of the channel is merely a rotation of the x and y axes for that particular ray. If the whole MCP were rotated it is clear that the central focus would remain in the same place. It is equally true that if a single channel is rotated its focus will not move. This is the reason why the lobes on the central peak, present in pincushion distorted plate images, are not present when the distortion modelled is channel rotation. In the pincushioned channel the rotations to the two reflection normals are independent. They depend on where the ray strikes the two cylinders.

148

Channel rotation is, therefore, a relatively unimportant channel plate distortion. It should be said, however, that observations made with an MCP X-ray telescope would utilise the photons which fell into the line foci as well as the ones in the central peak. Thus, although channel rotation does not affect the peak, its effects should not be ignored.

Channel axis misalignments

Figure 6.11 shows the effect of misalignments of the channel long axes on the focused image. As usual focusing 1.59keV X-rays with a Galileo type plate in the RAL experimental geometry has been simulated, and as usual the misalignments are double those believed to be present in the Galileo plates. This type of misalignment causes each channel to focus X-rays to a position which differs slightly from the ideal. Figure 6.12 shows that the focused spot for a given channel is simply moved in the x and y directions by twice the channel misalignment angles ϕ_1 and ϕ_2. Both the line foci and the true focus are mispositioned so that this is a serious type of channel plate imperfection.

Figure 6.11(a) shows the effect of misalignments between the tiles, namely that the part of the line focus due to each tile is translated relative to the ideal position, leading to a broken cruxiform structure. The central focus suffers doubly because the rays being focused are subject to reflection from two misaligned walls.

The individual channel misalignments broaden both line and true foci, by exactly the same mechanism as the tile misalignments (figure 6.11 b). Because of the randomly generated angles for each ray entering a channel this broadening is very smooth. This should be a fairly good model due to the large number of channels.

The tile misalignment angles were inferred from figure 5.8(b). That image clearly shows individual multifibres focusing to different positions in the line foci, causing fragmentation of the cruxiform structure. The lateral spread in the fragments was measured from the image, the corresponding misalignment angles were fed back into the ray trace code and the process was iterated until an image with line foci looking very similar to the RAL image was obtained. The misalignment angles were found to be $\phi_1 = \phi_2 = 0.35\text{mrad}$ or 1.2arcmin.
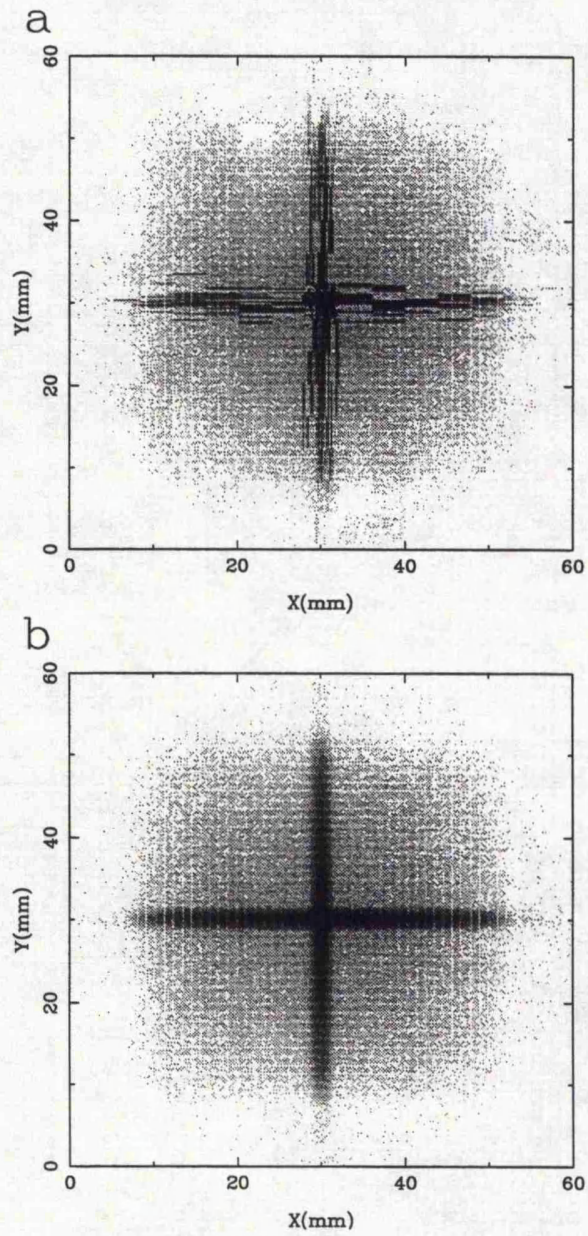
Figure 6.11: Logarithmic plots of images resulting from modelling plates with misalignments (a) between tiles only and (b) between individual channels within the tiles. Again, for clarity, the misalignment angles are twice those believed to be present in the Galileo plate.

150
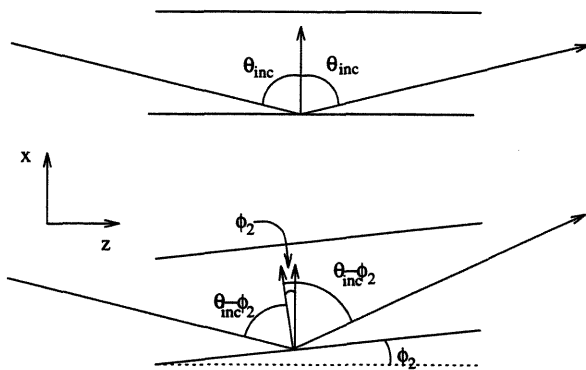
Figure 6.12: A misalignment of angle ϕ_2 to the yz plane causes the reflected rays to be misdirected by $2\phi_2$ with respect to the ideal ray direction.

The channel to channel misalignment angles within the multifibres and the inter-multifibre misalignment angles have been assumed to be in the same ratio as the corresponding channel rotations, this yields a figure of 0.23mrad (0.79arcmin) for the inter-channel misalignment.

The misalignment angles obtained here are in close agreement with the results of Chapman, Nugent & Wilkins (1993b). These authors obtained an overall misalignment angle of 0.3mrad by fitting their analytical model to experimental results from a circular pore plate. The FWHM of the peaks resulting from simulations with these tile and channel misalignments are 0.74mm and 0.69mm.

6.4 Surface Roughness

Channel surface roughness has been measured by X-ray scattering and by AFM. The scattering measurements have already been described in section 5.4.4. The AFM measurements were performed at the National Physical Laboratory (NPL) [2] using a Digital Instruments Nanoscope 2. A treatment of scattering from surface roughness has been included in the Monte Carlo model.

6.4.1 The MCP samples

The samples were prepared at the Leicester University Electron Microscopy Unit. Slices were cut from the MCPs with a diamond saw in such a way that channel surfaces were exposed, *ie* some channels were cut lengthways in two. After cutting, the samples were cleaned for thirty minutes in an ultrasonic bath filled with propan-2-ol in order to remove the broken glass debris caused by the sawing. SEM investigation of the channel surfaces after cleaning revealed that this technique had only been partially successful and some debris remained. Samples were taken from four types of MCP: Philips etched-only (LD061-14); Philips etched and sodium citrate polished (LD061-16); Galileo etched only (GEO3) and Galileo etched and hydrogen-reduced (GEO1). Some of these plates had been used previously in X-ray focusing experiments. Figure

---

[2] Division of Mechanical and Optical Metrology, National Physical Laboratory, Teddington, Middlesex, TW11 0LW.

MCP	manufacturer	process	RMS roughness (Å)
LD061-14	Philips	etch-only	50
LD061-16	Philips	etch + polish	22
GEO3	Galileo	etch-only	37

Table 6.1: Surface roughness measured by AFM.

6.2 is an electron micrograph of one of the channels which was cut open.

6.4.2 Atomic force microscopy

The AFM employs the same principle as the Talysurf of section 4.2. Namely, a sharp point scraping over the surface, and a cantilever arm system amplifying the surface features. The AFM measures interactions between the tip and surface down to the level of van der Waal's forces. The forces that it detects are in the range $10^{-13} - 10^{-6}$N (cf 10^{-2}N with the Talysurf). The excellent height resolution and accurate xy positioning (achieved by means of piezo-electric transducers) available with this device render it suitable for investigating the surface roughness of microchannels. In fact, special "cusp shaped" AFM tips (Ultralevers from Park Scientific) had to be used to facilitate entry into the opened channels, which in the case of the Philips plates, are only 25μm wide with the remains of the walls standing as much as 25μm above the bottom. These high aspect ratio tips suffered considerable wear from contact with the hard glass surface and this may have compromised the results to some extent, though the NPL personnel were confident that their figures were reasonably accurate.

The AFM sampled 5000Å square areas and found their RMS surface roughness. Surface roughness values were obtained for both types of Philips MCP but only for one of the Galileo samples - the etched-only one. These data are listed in table 6.1. The numbers are roughly in accordance with those obtained from the X-ray scattering work with the reduced glass Galileo plate ($\sigma = 30$Å). Kaaret et $al.$ (1992) obtained $\sigma = 57$Å and $\tau = 1.41\mu$m using their optical profilometer on a reduced glass Galileo plate. Chapman, Nugent & Wilkins (1993b) obtained the best fits between experimental data and their analytical model (Chapman, Nugent & Wilkins 1993a) by setting $\sigma = 37$Å and $\tau = 1.2\mu$m in the model.

The roughness values obtained from the Philips etched-only and etched and polished plates encouragingly show that the weak acid etch has caused a reduction in the RMS roughness by a factor of two. This result indicates that acid polishing may be a very important technique in the future development of MCP optics.

In these measurements the areas sampled were 0.5μm squares. These dimensions set an upper limit on the range of roughness length scales over which the technique averages. This range is quite different to that probed by the X-ray scattering experiment of section 5.4.4 which can only sample roughness with spatial wavelengths scales longer than 3μm.

6.4.3 Modelling the surface roughness

The code used to model scattering from surface roughness uses the treatment described in section 5.4.4. The probability of a ray being scattered is given by:

$$P(scat) = 1 - e^{-(4\pi\sigma sin\theta/\lambda)^2} \tag{6.15}$$

A random number between 0 and 1 is generated and compared with this probability, if the number is less than $P(scat)$ then the ray is treated as having been scattered. In the initial analysis all scattered rays were discarded and treated as having been absorbed in subsequent reflections due to incidence at large grazing angles. This level of analysis only calculates a worst estimate of the reduction in focusing efficiency.

A better model goes as follows. If a ray striking a channel wall at a grazing angle θ is scattered, the reflection direction is calculated as described in section 2.3.4 except that a perturbation to the reflection angle is made to account for the scattering. An average scatter angle for a ray incident on a rough surface is given by:

$$\phi_{scat} = \frac{\lambda}{\tau sin\theta} \tag{6.16}$$

Scatter angles are generated randomly using a Gaussian distribution with a mean of zero and a standard deviation of ϕ_{scat}. The random numbers are, once again, generated using a NAG routine. Inclusion of the scatter angle modifies equation 2.13 to give:

$$\mathbf{d} = 2\hat{n}cos(\theta_{inc} + \phi_{scat}/2) + \mathbf{b} \tag{6.17}$$
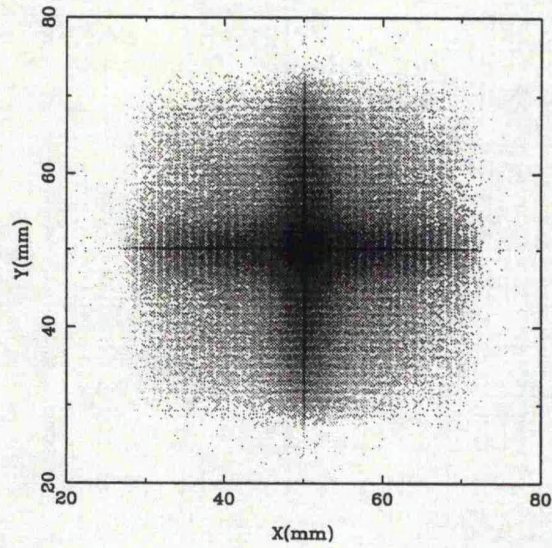
Figure 6.13: Logarithmic plot of an image resulting from modelling a plate with rough channel surfaces illuminated by 1.59keV X-rays in the RAL geometry. Again for clarity the roughness is twice that believed to be present in the Galileo plate.

ϕ_{scat} is divided by 2 because it alters both $\theta_i nc$ in figure 2.4 (the incidence and reflection angles) and hence is counted twice. The reflected ray generated like this continues down the channel, the code checks for further reflections and so on.

6.4.4 Results

Figure 6.13 shows, on a logarithmic intensity scale, the results from a simulation of a Galileo type plate in the RAL geometry illuminated by 1.59keV X-rays. The plate modelled is ideal, apart from exhibiting surface roughness with $\sigma = 60$Å and $\tau = 17\mu$m. The scattering introduces a general blur to the image as an uncertainty is introduced to each reflection angle, something like the effect of misalignment of the channel long axes, although the distribution of angles is rather different. An image similar to figure 6.13 except with $\sigma = 30$Å, the actual roughness determined from the X-ray scattering measurements of section 5.4.4 for the reduced glass Galileo plate GEO4, has an FWHM of 0.30mm.

155

| distortion | | FWHM F | $\sqrt{(F^2 - F^2_{perfect})}$ |
type	magnitude	(mm)	(mm)
perfect		0.27	N/A
pincushion	$g/D = 0.0045$	0.71	0.66
channel rotation	$\phi_{rms} = 0.86°$	0.27	0
tile rotation	$\phi_{rms} = 1.29°$	0.27	0
channel misalignment	$\phi_{rms} = 0.8 \text{arcmin}$	0.69	0.63
tile misalignment	$\phi_{rms} = 1.2 \text{arcmin}$	0.74	0.69
surface roughness	$\sigma = 30\text{Å}; \quad \tau = 17\mu\text{m}$	0.30	0.13
total		1.61	1.59

Table 6.2: The various distortions and their contributions to the width of the focal spot.

6.5 Integration of all distortions into a comprehensive model

Now that all the known distortions of the channel plate have been measured or inferred as accurately as possible from the available data they can be combined into a single model using the techniques described in this chapter. Table 6.2 is a compendium of the contributions to the focal spot breadth from all the distortions discussed above, both individually and in combination. Figure 6.14(a) shows an image resulting from a simulation of a Galileo type plate focusing 1.74keV X-rays in the geometry used in the VTF at Leicester (section 3.1) while figure 6.14(b) shows the corresponding X-ray image (in fact a reproduction of figure 3.12 b). Clearly the simulated and real images are very similar. The FWHM of the peak, 1.61mm, is in close agreement with the figure obtained with Si-K 1.74keV X-rays in the Leicester laboratory (1.4 × 2.0mm). The peak gain, is 40, in reasonable agreement with the value determined experimentally at RAL (~ 20). These lend credibility to the ray-trace model.

From this model we can see that pincushion, tile and channel axis misalignment contribute more or less equally to the breadth of the central focus produced by this plate. The other distortions have a relatively minor effect. At high energies scattering from the surface roughness will, of course, become more significant. These are the problems that must be primarily be addressed in the next generation of these optics.
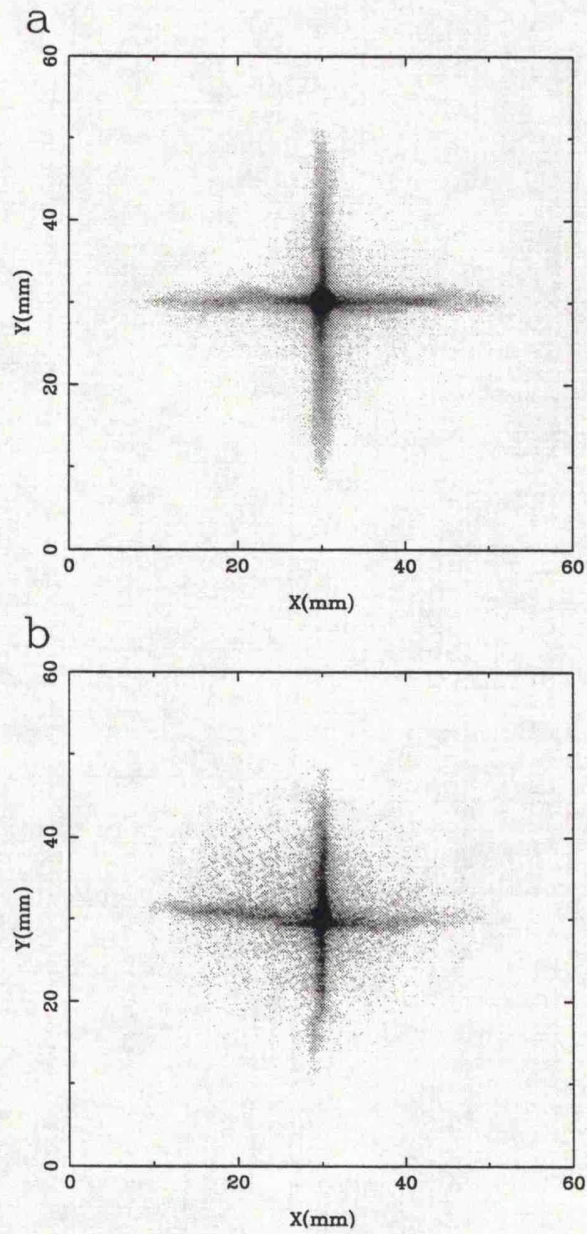
Figure 6.14: Simulated (a) and real (b) images of an MCP focusing 1.74keV X-rays in the VTF geometry of Chapter 3.

157

As an example of the sort of predictions that the model can make a simulation has been run with all the distortion parameters set to half the severity found in the Galileo reduced glass plates. This might represent a reasonable next step forward in the development of MCP optics. Again 1.74keV X-rays in the VTF geometry have been simulated. The FWHM of the focused peak is now only 0.90mm (4.5arcmin) and the peak gain has increased from 40 to 181.5. Thus we can see that a fairly modest improvement in manufacturing technique will produce impressive gains in performance. The modelling described in this chapter will undoubtedly have a significant rôle in guiding the manufacture of next generation MCP optics.

Chapter 7

Conclusions and further work

7.1 Conclusions

The knowledge gained from this work falls into two areas. The first is a thorough understanding of the current state of MCP focusing technology. The second is an appreciation of how deficiencies in the technology currently limit the performance of MCP X-ray optics and what development work must be done to improve that performance.

If we recall the list of manufacturing requirements for telescope optics set out at the end of chapter 1, we may now compare it with the experimental results obtained in chapters 3-6 and see to what extent the existing technology meets the requirements and in what areas improvements are needed. The list of requirements was as follows:

1. Drawing and assembly of regular cuboidal channels

2. Etching of long channels

3. Production of smooth channel surfaces

4. Achievement of good parallelism between channels on flat plates

5. Slumping of thick plates to an accurate spherical figure, maintaining good channel alignment.

Our results may be summarised, point by point, as follows:

1. Channel distortion is a problem with plates from both Philips and Galileo. This was not taken into account in the ray-tracing from which the HXT specification was derived (Willingale & Fraser 1995; Fraser *et al.* 1993c).

2. A 4mm thick plate with *L:D*=320:1 has been successfully etched An aspect ratio of approximately *L:D*=700:1 would be required for a hard X-ray telescope.

3. The RMS channel surface roughness values obtained in chapters 5 and 6 range from 22-50Å. These are somewhat larger than the 10Å figure of merit specified for HXT (also typical of conventional grazing incidence optics).

4. Channel long axis misalignment is the main factor degrading the focus of current plates (see chapters 3,5 and 6). The best foci achieved so far have FWHM of about 6arcmin. They were achieved with soft (0.28keV and 1.74keV) X-rays, so their breadth is due mainly to long axis misalignments; scattering is not a dominant effect at these photon energies. An RMS misalignment angle of 0.5mrad has been inferred from these images. In the HXT modelling an RMS misalignment of 0.2mrad yielded a focus with a FWHM of ~1-2arcmin although pincushion channel distortion was not taken into account.

5. The Philips slumping technique has proved very successful (chapter 4). Thin (1mm) plates have been slumped to the correct radius for an ASM class instrument with, apparently, very little distortion of the channels. Thicker (4mm) plates have been slumped to the same radius. For a hard X-ray telescope it will be necessary to bend 9mm thick plates to ~10m radius. Conversely, if channel sizes can be reduced by a factor of two (altering *D* from 12.5μm to ~ 6μm) currently slumped plate thicknesses will be adequate.

7.2   Future Work

Successful future work in this field will require a close collaboration between MCP manufacturers and Leicester personnel, enabling production of plates which exhibit the mechanical regularity and smooth surface finish described above. Fortunately, the excellent relationship between

Leicester and these companies is likely to be reinforced by the instigation of an ESA Technology Research Programme (TRP)[1]. This programme, which stemmed from the HXT proposal (Fraser *et al.* 1993c), provides substantial funds for fabrication of MCP optics of the type required for an HXT type instrument. Leicester's rolling grant from PPARC has been extended to cover the testing of these new devices. The project will cover development of conventional square packed plates and also the novel radial packing mentioned in section 1.5.

An HXT type telescope could be used to image the important 5-50keV spectral region in which the transition between thermal and non-thermal processes occurs. It would be particularly suitable for observing X-ray emission from compact objects (white dwarfs, neutron stars, black holes). The accretion disc around such an object provides a source of soft thermal X-rays which may seed Compton processes leading to the emission of high energy photons in regions where hot electrons are present. Cyclotron or synchrotron emission may occur from regions where relativistic electrons are moving in strong magnetic fields. In weaker fields the lower energy photons produced may be upscattered by the electrons leading to synchrotron self-Compton emission. Where hard X-rays illuminate material - the accretion disc or compact object itself a proportion of the X-rays will be Compton reflected.

The spectra due to these processes may be modified by line emission, photoelectric absorption and Compton downscattering. To distinguish the subtle differences between these mechanisms in both AGN and galactic X-ray binaries good sensitivity and spectral resolution are required.

The proposed HXT fulfills these requirements, providing by the use of MCP optics, arcminute spatial resolution with 0.2mCrab sensitivity (figure 7.1. The optics allow the use of small semi-conductor detectors with good spectral resolution which also provide a polarimetric capability (Fraser *et al.* 1993c).

In order to achieve this performance certain requirements, which have been determined by ray-tracing, are placed on the optics. These are:
(a) An RMS surface roughness of 10Å.
(b) An RMS gradient error of 0.2mrad. This gradient error represents a combination of channel misalignments, distortions of the channel surfaces and figure errors due to the slumping process.

---

[1] Progress in MCP optics (94/4.15.5 in the ESA "Blue Book")

161
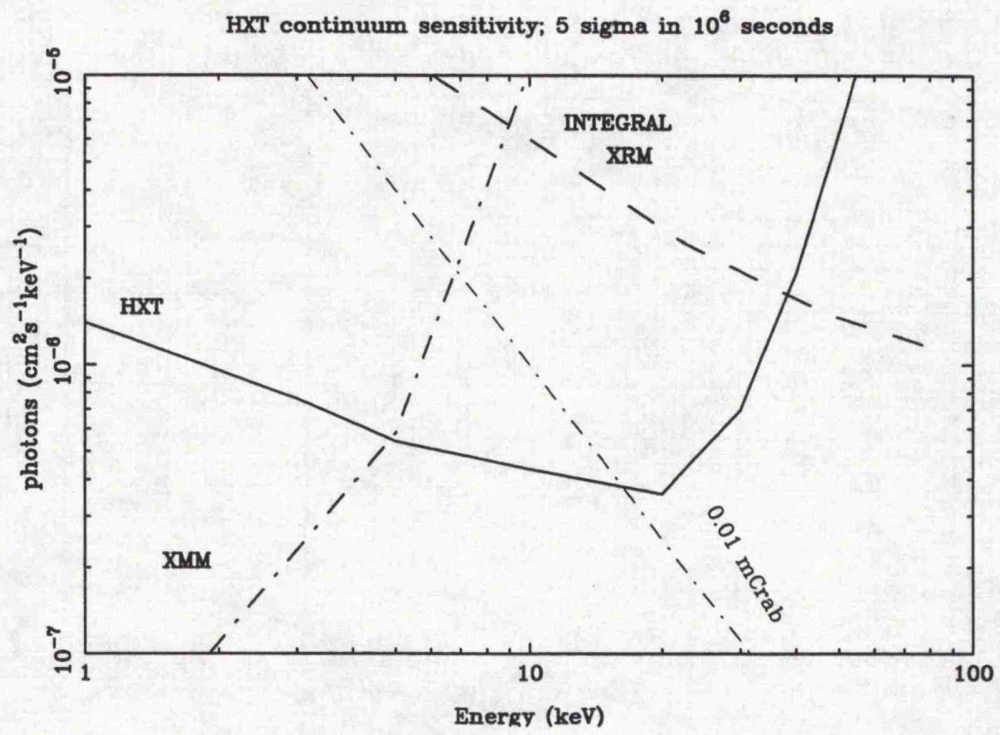
Figure 7.1: HXT continuum sensitivity

The current "state of the art" of MCP optics is reviewed in section 7.1 above. Currently the optics fall short of the specifications required for an HXT type imager. Manufacturers will have to address these shortfalls by developing the slumping, drawing, etching, multifibre assembly and fusion techniques. In particular the assembly of multifibres containing large ($\sim 40 \times 40$) numbers of channels may prove advantageous as by far the worst channel distortion and misalignment occurs within a few rows from the multifibre boundaries. Large multifibres will minimise the proportion of the channels which are near these boundaries. The successful Philips weak acid polishing etch must be further developed and efforts must be made to deposit metal coatings on the inside surfaces of the channels as such coatings would very significantly increase the critical grazing angle at high X-ray energies.

At Leicester, test facilities and procedures must be established to provide accurate informative feedback to channel plate manufacturers. It is vital that Leicester personnel work closely with these manufacturers as only a thorough knowledge of both the optical characteristics of the devices and the problems associated with their fabrication will lead to rapid development progress. In summary, the work which must be done at Leicester is as follows:

In order to test hard X-ray telescope type plates, which will have slump radii of order 10m, a long (17m) beamline, equipped with a 100kV X-ray source will be commissioned. In this facility X-rays will be reflected at grazing angles of similar size to those suffered by rays passing through HXT. A programme of tests with hard X-rays will begin, giving an overall picture of the operation of MCP optics at high photon energies.

Methods must be developed to test for problems one at a time, for instance channel rotation may be detected by SEM inspection. long axis misalignment may be mapped by illuminating single lines of channels via a mask (suitably fine line apertures may be produced by lithographic techniques) with a point like X-ray source (possibly the RAL laser plasma source described in chapter 5). The high resolution of X-ray film would be exploited to record the positions of the reflected spots due to individual channels. Channel alignments would determined from the relative positions of these spots. In order to ascertain at which points in the manufacturing process misalignments are introduced, it may be necessary to apply such tests to samples of multifibre, both before and after the second draw, as well as entire optics.

Channel surface roughness may be assessed by X-ray scattering, AFM or phase contrast microscopy. These techniques must be developed or further developed to obtain accurate measurements of the roughness. A standard test matrix must be established. All types of microscopy applied to channel surfaces are, of course, destructive forms of testing whereas X-ray scattering measurements are not, although their interpretation is not straightforward. Furthermore, optics must be illuminated with hard X-rays at realistic grazing angles in the beamline described above.

Slump profiles must be measured so that we may find how closely plates adhere to the correct spherical figure. The Talysurf is a device which has been used for this purpose albeit in a fairly simplistic way. It could be used to build up detailed surface maps although there is a risk of its stylus scratching the MCP surface. Non-contact optical profilometers are available, though how well they would sample the peculiar MCP surface is not known.

In parallel with this considerable body of experimental work, the ray-trace model will be further developed; the full distortion model will be incorporated into the slumped-plate code and enhanced to include multiple optic elements, further distortions such as the radiused channels of figure 6.1 and so on. This model should prove invaluable in further understanding MCP optics.

Looking further ahead, some thought must be given to deconvolution of the optics' PSF from images obtained with them. It is likely that there will be differences between the PSFs of any two optics, due to inhomogeneities along the boule. As a telescope might have 200 parallel optics this deconvolution represents a very considerable task.

Finally, applications for MCP optics in other fields will be investigated. In chapter 5 a high intensity X-ray beamline for microscopy or X-ray fluorescence microanalysis is proposed. This idea is now starting to attract interest from the microanalysis community (Siegbahn & Maripou 1994). A programme of research into the use of MCP optics for X-ray lithography of microelectronic devices has also been started up at Leicester. This is a collaborative venture with Nova Scientific [2] funded by the US government's Advanced Research Projects Agency (ARPA).

Now that reasonable funding has finally been secured, microchannel plate optic development at Leicester should enter a new, dynamic phase.

---

[2]Nova Scientific Inc. 54 Main Street, 7 Cedar Court, Sturbridge, MA01566, USA

References

Angel, J. R. P., 1979. *Astrophys.J.*, **233**, 364.

Bar-Lev, A., 1984. *Semiconductors and electronic devices*, Prentice Hall.

Barstow, M. A. & Sansom, A. E., 1990. In: *EUV,X-ray, and gamma ray instrumentation for astronomy*, **1344**, 244, eds O.H.W.Siegmund & H.S.Hudson, Proc.SPIE.

Beckmann, P. & Spizzichino, A., 1963. *The scattering of electromagnetic waves from rough surfaces*, Pergamon Press.

Brunton, A. N., Fraser, G. W., Lees, J. E. & Pearson, J. F., 1993. XRA group internal report, Leicester University.

Caroli, E., Stephen, J. B., di Cocco, G., Natalucci, L. & Spizzichino, A., 1987. *Space Sci.Rev.*, **45**, 349.

Chapman, H. N., Nugent, K. A., Wilkins, S. W. & Davies, T. J., 1990. *J.X-ray Sci. Tech.*, **2**, 117.

Chapman, H. N., Nugent, K. A., Wilkins, S. W. & Rode, A. V., 1992. In: *Soft X-ray Microscopy*, **1741**, Proc.SPIE.

Chapman, H. N., Nugent, K. A. & Wilkins, S. W., 1991. *Rev.Sci.Instrum.*, **62**, 1542.

Chapman, H. N., Nugent, K. A. & Wilkins, S. W., 1993a. *Appl.Opt.*, **32**, 6316.

Chapman, H. N., Nugent, K. A. & Wilkins, S. W., 1993b. *Appl.Opt.*, **32**, 6333.

Chen, A., Kaaret, P. & Kenny, T. W., 1993. In: *Multilayer and grazing incidence X-ray/EUV optics 2*, **2011**, 227, eds Hoover, R. B. & A. B. C. Walker, J., Proc.SPIE.

Christensen, F. E., Abdali, S., Hornstrup, A., Schnopper, H. W., Slane, P. & Romaine, S. E., 1993. In: *Multilayer and grazing incidence X-ray/EUV optics 2*, **2011**, p. 18, eds Hoover, R. B. & A. B. C. Walker, J., Proc.SPIE.

Christensen, F. E., Abdali, S., Frederiksen, P. K., Ramussen, I., Westergaard, N. J., Schnopper, H. W., Louis, E., Voorma, H. J., Koster, N., Wiebicke, H., Halm, I., Geppert, U., Silver, E., Legros, M., Borozdin, K., Joensen, K. D., Gorenstein, P., Wood, J. & Gutman, G.,

1994. *Journal de Phisique*, 4, 1599.

Church, E. L., Jenkinson, H. A. & Zavada, J. M., 1979. *Optical Engineering*, **18**, 125.

Clampin, M., Crocker, J., Paresce, F. & Rafal, M., 1988. *Rev.Sci.Instrum.*, **58**, 1269.

Cromer, D. T. & Liberman, D., 1970. LASL report LA-4403, Los Alamos Laboratory.

Fraser, G. W. & Mathieson, E., 1981. *Nucl.Instr.Meth.*, **179**, 591.

Fraser, G. W., Barstow, M. A. & Pearson, J. F., 1988. *Nucl.Instr.Meth.*, **A273**, 667.

Fraser, G. W., Lees, J. E., Pearson, J. F., Sims, M. R., Spragg, J. E. & Willingale, R., 1989. In: *X-ray/EUV optics for Astronomy and Microscopy*, **1160**, 568, ed. Hoover, R. B., Proc.SPIE.

Fraser, G. W., Sims, M. R., Kaaret, P., Manzo, G. & Goodall, C., 1990. ASM mission proposal to ESA, Leicester University UK.

Fraser, G. W., Lees, J. E., Pearson, J. F. & Barstow, M. A., 1991a. *Nucl.Instr.Meth.*, **A310**, 292.

Fraser, G. W., Lees, J. E., Pearson, J. F., Sims, M. R. & Roxburgh, K., 1991b. In: *Multilayer and Grazing Incidence X-Ray/EUV Optics*, **1546**, p. 41, ed. Hoover, R. B., Proc.SPIE.

Fraser, G. W., Brunton, A. N., Lees, J. E. & Emberson, D. L., 1993a. *Nucl.Instr.Meth.*, **A334**, 579.

Fraser, G. W., Brunton, A. N., Lees, J. E., Pearson, J. F. & Feller, W. B., 1993b. *Nucl.Instr.Meth.*, **A324**, 404.

Fraser, G. W., Willingale, R., Turner, M. J. L., Cole, R. E., Cruise, A. M. & Gnedin, Y. N., 1993c. HXT mission proposal to ESA, Leicester University UK.

Fraser, G. W., Lees, J. E. & Pearson, J. F., 1989. *Nucl.Instr.Meth.*, **A284**, 483.

Fraser, G. W., 1982. *Nucl.Instr.Meth.*, **195**, 523.

Fraser, G. W., 1989. *X-ray Detectors in Astronomy*, Cambridge University Press.

Gibson, W. M. & MacDonald, C. A., 1994. In: *X-ray and UV detectors*, **2278**, 156, eds Hoover,

R. B. & Tate, M. W., Proc.SPIE.

Gorenstein, P., 1991. In: *Multilayer and grazing incidence X-ray/EUV optics*, **1546**, 91, ed. Hoover, R. B., Proc.SPIE.

Hassler, D. M., Rottman, G. J. & Lawrence, G. M., 1990. In: *EUV, X-ray and gamma-ray instrumentation for astronomy*, **1344**, p. 194, ed. Siegmund, O. H. W., Proc.SPIE.

Henke, B. L., Uejio, J. Y., Stone, G. F., Dittmore, C. H. & Fujiwara, F. G., 1986. *J.Opt.Soc.Am.B*, **3(11)**, 1540.

Henke, B. L., 1981. In: *Topical conference on low-energy X-ray diagnostics*, **75**, p. 146, eds Attwood, D. & Henke, B., AIP ISS-75.

Holland, A. D., Fraser, G. W., Willingale, R. & Turner, M. J. L., 1994. In: *Proceedings of the International Workshop on Imaging in High Energy Astronomy, Anacapri Italy*. In press.

Hudec, R., Inneman, A., Pina, L. & Gorenstein, P., 1994. In: *Proceedings of the International Workshop on Imaging in High Energy Astronomy, Anacapri, Italy*. In press.

Joy, M. & Weisskopf, M. C., 1991. In: *Multilayer and grazing incidence X-ray / XUV optics*, **1546**, 303, ed. Hoover, R. B., Proc.SPIE.

Kaaret, P. E. & Geissbühler, P., 1991. In: *Mutilayer and grazing incidence X-ray/EUV optics*, **1546**, p. 82, ed. Hoover, R. B., Proc.SPIE.

Kaaret, P., Novick, R., Martin, C., Hamilton, T., Sunyaev, R., Lapshov, I., Silver, E., Weisskopf, M., Elsner, R., Chanan, G., Manzo, G., Costa, E., Fraser, G. & Perola, G., 1989. In: *X-Ray/EUV Optics for Astronomy and Microscopy*, **1160**, 587, ed. Hoover, R. B., Proc.SPIE.

Kaaret, P., Geissbühler, P., Chen, A. & Glavinas, E., 1992. *Appl.Opt.*, **31**, 7339.

Kirkpatrick, P. & Baez, A. M., 1948. *J.Opt.Soc.Am.*, **38**, 766.

Kumakhov, M. A. & Komarov, F. F., 1990. *Phys.Rep.*, **191**, 289.

Land, M. F., 1978. *Scientific American*, **239**, 126.

Lecomte, P. & Perez-Mendez, V., 1978. *IEEE Trans.Nucl.Sci.*, NS-25, 964.

Lees, J. E., Fraser, G. W., Brunton, A. N. & Willingale, R., 1994. In: *Proceedings of the*

International Workshop on Imaging in High Energy Astronomy, Anacapri, Italy. In press.

Lu, P., Li, R., Wang, X., Li, Y., Fan, P., Zhang, Z., Chen, S. & Xu, Z., 1992. In: *X-ray lasers ISS-125*, **125**, p. 379, ed. Fill, E. E., IOP.

Murray, S. S. & Chappell, J. H., 1988. In: *X-Ray Instrumentation in Astronomy II*, **982**, p. 48, ed. Golud, L., Proc.SPIE.

Pearson, J. F., 1984. *PhD thesis*, University of Leicester.

Ramsey, B. D., Austin, R. A. & Decher, R., 1994. *Space Sci.Rev.*, **69**, 139.

Rockett, P. D., Bird, C. R., Hailey, C. J., Sullivan, D., Brown, D. B. & Burkhalter, P. G., 1985. *Appl.Opt.*, **24**, 2536.

Schmidt, W. K. H., 1975. *Nucl.Instr.Meth.*, **127**, 285.

Schmidt, W. K. H., 1981. *Space Sci.Rev.*, **30**, 615.

Siegbahn, K. & Maripou, R., 1994. *Private Communication to W. B. Feller, Nova Scientific Inc.*

Stead, A. D., Cotton, R. A., Page, A. M., Goode, J. A., Steele, C. G., Duckett, J. G. & Ford, T. W., 1993. In: *Applications of laser-plasma radiation*, **2015**, p. 2, ed. Richardson, M. C., Proc.SPIE.

Timothy, J. G., 1981. *Rev.Sci.Instrum.*, **52**, 1131.

Turcu, I. C. E., Ross, I. N., Shields, H., Trenda, P., Batani, D., Fluck, P. & Goodson, H., 1994a. *Microelectronic Engineering*, **23**, 207.

Turcu, I. C. E., Ross, I. N., Trenda, P., Wharton, C. W., Meldrum, R. A., Daido, H., Schulz, M. S., Fluck, P., Michette, A. G., Juna, A. P., Maldonado, J. R., Shields, H., Tallents, G. J., Dwivedi, L., Krishnan, J., Stevens, D. L., Jenner, T. J., Batani, D. & Goodson, H., 1994b. In: *Applications of Laser Plasma Radiation*, **2015**, p. 243, ed. Richardson, M. C., Proc.SPIE.

Turcu, I. C. E., Ross, I. N. & Tallents, G. J., 1993. *Appl.Phys.Lett.*, **63**, 3046.

Turner, M. J. L. & Smith, A., 1981. *Space Sci.Rev.*, **30**, 513.

Wilkins, S. W., Stevenson, A. W., Nugent, K. A., Chapman, H. & Steenstrup, S., 1989. *Rev.Sci.Instrum.*, **60**, 1026.

Willingale, R. & Fraser, G. W., 1995. *Broad band X-ray imaging with microchannel structures, In preparation.*

Winkler, C. E., Cumings, N. E., Randolph, J. L. & Talley, D. H., 1993. In: *Astroparticle physics and novel gamma-ray telescopes*, **1948**, 63, ed. Cline, D. B., Proc.SPIE.

Wiza, J. L., 1979. *Nucl.Instr.Meth.*, **162**, 587.

Wolter, H., 1952a. *Ann.Physik*, **10**, 286.

Wolter, H., 1952b. *Ann.Physik*, **10**, 94.

Xiao, Q., Ponamarev, I. Y., Kolomitsev, A. I. & Kimball, J. C., 1992. In: *X-Ray detector physics and applications*, **1736**, p. 227, ed. ?, Proc.SPIE.

Zhao, P., Freeman, M. D., Jerius, D. & Shao, Y., 1993. In: *Multilayer and grazing incidence X-ray/XUV optics 2*, **2011**, p. 59, eds Hoover, R. B. & Walker, A. B. C., Proc.SPIE.